Engineering and Applied Science Theses & Dissertations

McKelvey School of Engineering

Summer 8-15-2017

Photodynamic Therapy: Agents and Mechanisms

Rebecca Claire Gilson
Washington University in St. Louis

Recommended Citation

WASHINGTON UNIVERSITY IN ST. LOUIS

School of Engineering and Applied Science

Department of Biomedical Engineering

Dissertation Examination Committee:
Samuel Achilefu, Chair
Mikhail Y. Berezin
Joseph P. Culver
Kristen M. Naegle
Lihong V. Wang

Photodynamic Therapy: Agents and Mechanisms

by

Rebecca C. Gilson

A dissertation presented to
The Graduate School
of Washington University in
partial fulfillment of the
requirements for the degree
of Doctor of Philosophy

August 2017
St. Louis, Missouri

Table of Contents

List of Figures

Acknowledgments

I would like to thank my thesis mentor, Samuel Achilefu, for supporting, encouraging, and mentoring me throughout graduate school. Thank you for providing me with flexibility in the scope and direction of my research projects. While not always easy, this independence allowed me to lose myself in the gritty, yet intriguing mechanisms of the photophysical properties of fluorophores.

I would like to thank my thesis committee members: Mikhail Berezin, Joseph Culver, Kristen Naegle, and Lihong V. Wang, for their advice and support throughout graduate school.

Thank you to the fellow graduate students and members of the Optical Radiology Lab. You have made me a better scientist and helped prepare me for the challenges of academic research.

Thank you to the department of Biomedical Engineering and specifically, Karen Teasdale for always bringing cheer to my day.

I would like to thank Nancy Pope and the Spencer T. Olin Fellowship for funding the first four years of my Ph.D. and for providing mentorship and fellowship. Nancy, thank you being a constant source of support: academically and personally. You have taught me a great deal about how to be a sincere and responsible leader.

Thank you to my fellow Spectra officers, past and present, for committing much time and effort to this student initiative. I loved working with you to come up with new exciting learning modules and events.

Thank you, John Edwards, Rochelle Smith, Jessica Miller and Adam Joyce the founders of Connections. I benefited immensely from Connections' supportive and welcoming community.

Rebecca Gilson

Washington University in Saint Louis

August 2017

To my family, without whom I would not be the scientist I am today.

ABSTRACT OF THE DISSERTATION

Photodynamic Therapy: Agents and Mechanisms

By

Rebecca C. Gilson

Doctor of Philosophy in Biomedical Engineering

Washington University in St. Louis, 2017

Advisor: Samuel Achilefu, Ph.D.

<u>Abstract</u>

Despite enormous efforts, cancer remains a leading cause of morbidity and mortality world-wide. The main challenges currently facing cancer therapy include lack of adequate tumor targeting, failure to treat hypoxic tumor cells, and induction therapy resistant tumors. A solution to these limitations can be found in photodynamic therapy (PDT) which combines light and light activatable compounds, photosensitizers (PSs), to produce cytotoxic reactive oxygen species (ROS) to damage tumor tissue. This creates a spatiotemporal therapeutic effect, where cell damage only occurs at the intersection of the PS and light. PDT can treat tumors through unique mechanisms which reduce induction of tumor resistance. Although PDT has had clinical success in treating skin cancer and macular degeneration, it has yet to be a widely adopted or accepted therapy.

In this dissertation, we lay the groundwork for a new PDT strategy which systematically addresses and optimizes each aspect of PDT. To overcome the limitation of PDT to treat hypoxic tumors, we developed a novel nano-photosensitizer, TiO_2-N3, that produces cytotoxic ROS even under hypoxic conditions. Next, to determine the optimal intracellular target for TiO_2-N3, we compared the therapeutic outcome of ROS generated in endosomes, lysosomes, mitochondria, and ER. We identified the ER as the organelle most sensitive to ROS damage and therefore the optimal intracellular target for TiO_2-N3. Finally, to deliver TiO_2-N3 to tumors in vivo, we developed two tumor targeting agents, both

of which are equipped with near-infrared fluorophores for whole body imaging. This work has laid the foundation for a novel PDT strategy by overcoming issues that have limited the clinical adoption of PDT.

Chapter 1 : Introduction

1.1 Cancer therapy

Despite the continuous development of new therapies and diagnostic techniques, cancer remains a leading cause of morbidity and mortality world-wide.[1] It is estimated that 90% of cancer deaths are due to metastasis, a result of late stage diagnosis, failure to surgically resect the entire primary tumor, or development of therapy resistance.[2,3] In an attempt to reduce the risk of metastasis, multiple therapies can be combined (e.g. surgery, chemotherapy, and molecular targeted therapy) in order to inflict damage to the tumor through distinct mechanistic pathways. An alternative to conventional treatment is photodynamic therapy (PDT), a single treatment method that disrupts cancer growth and metastasis through multiple therapeutic pathways.[4]

1.2 Photodynamic therapy of cancer

PDT combines light with light-activatable drugs, photosensitizers (PSs), to produce cytotoxic reactive oxygen species (ROS) (**Figure 1**). PDT affords high spatiotemporal control of the treatment, where cellular damage only occurs at the intersection of the PS and light, minimizing off-target toxicity.[5] The damage inflicted by PDT can be classified into two categories of reactions: type I, oxygen independent free radical production, and type II, oxygen dependent singlet oxygen production.[6] Type I reactions enable the treatment of both normoxic and hypoxic tumors, whereas type II reactions are more effective in highly vascularized and oxygenated tumors. ROS and free reactions cause tumor regression through three pathways: (1) direct cell death through necrosis or apoptosis, (2) disruption of tumor vasculature to starve the tumors of nutrients and oxygen, and (3) activation of the immune system.[4,7] This three-pronged strategy prevents the tumor from developing resistance, enabling multiple administrations of

1

PDT.

Administration of PDT begins with delivery of the PS to the tumor, typically through intravenous injection, topical application, or intratumoral injection. After the PS has accumulated in the tumor, a period called the drug-light-interval (DLI), the tumor is irradiated with a wavelength of light that matches the absorption maximum of the PS. The light-activated PS generates ROS and free radicals to induce tumor regression.
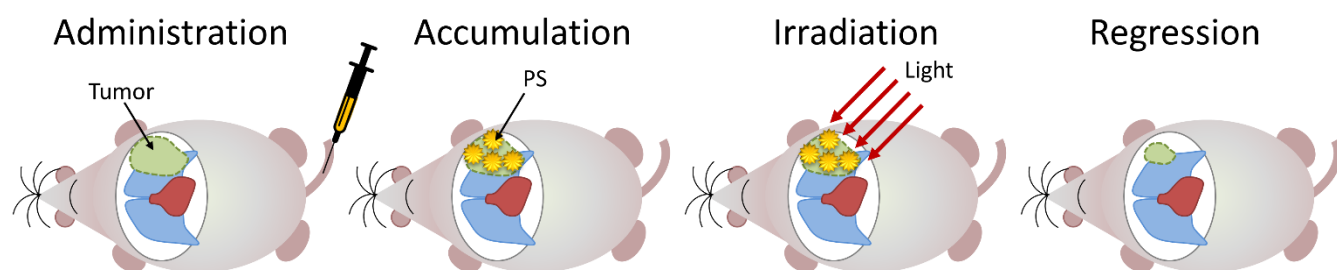
Figure 1. General scheme for PDT.

A careful consideration of a PSs' photophysical properties, pharmacokinetics, and structural features is critical for the development of a successful PDT strategy.[4,8] Photophysical properties dictate the quantity of cytotoxic ROS that will be produced. Pharmacokinetics define the DLI, clearance route, and circulation time of the PS. The PS structure controls solubility, ease of formulation, and ability to add functional groups or targeting ligands. These properties will be discussed further in the following sections.

1.2.1 Clinical PS

There are currently over five clinically approved PSs for treatment of diverse cancers, such as head and neck, pancreas, liver and prostate, in addition to age-related macular degeneration.[4] Most of these PSs are structural derivatives of porphyrins, chlorins, bacteriochlorins or phthalocyanines and are administrated through an intravenous injection (0.1-4 mg/kg).[4,9,10] After a DLI of 0.25-72 h, the tumors are irradiated with light ranging from 8-200

J/cm^2.[4,9,10] The light is delivered either externally or interstitially depending on the site of the tumor. A major side effect of PDT is skin phototoxicity which occurs when PSs have long clearance times, sometimes remaining in the body for days after treatment, and requiring patients to remain inside under low light conditions.[11]

A second class of clinically approved PDT substances are PS precursors, administered through topical application. For example, aminolevulinic acid (ALA) enhances the production of protoporphyrin IX, an endogenous PS.[4,10]

1.2.2 Administration of PS and tumor accumulation

The PS can be administered to a patient through intravenous injection, intratumoral injection, or topical administration. The PS typically accumulates more in the tumor, compared to normal tissue, through the enhanced permeability and retention (EPR) effect that exists in most solid tumors.[4,9,12] However, an increasingly large amount of research focuses on developing tumor-targeted PSs to optimize the distribution and uptake in tumors. A variety of methods are currently being explored, including nanoparticle formulation, and antibody or small peptide based targeting.[13,14] Targeted PSs have yet to be translated into the clinic.

1.2.3 Light delivery

Due to the limited penetration of visible light through biological tissue, several techniques have been developed to ensure light delivery to all parts of the tumor. External radiation from an LED through an optical fiber is used for skin, head and neck,[15] or esophageal cancer.[16] Interstitial irradiation is used for internal organ cancers, such as pancreas and liver cancer.[10,17] For prostate cancer, light diffusing fibers are placed within the prostate to ensure even light dosing.[18] In addition, red and near-infrared (NIR) light penetrates deeper into tissue due to reduced scattering and absorption of endogenous proteins.[19] Therefore, PS that absorption

in the red or NIR are more suitable for treating non-superficial lesions.

1.2.4 Tumor regression mechanism

PDT destroys tumor tissue through multiple pathways, including direct cell death, disruption of tumor vasculature, and stimulation of the immune system.[7] Apoptosis-induced cell death occurs when the intracellular ROS activate the caspase signaling cascade. This typically occurs when the PS is activated in the mitochondria, lysosome, or ER and ROS production results in permeabilization of the organelle's membrane, releasing its contents into the cytosol. Cytochrome c released from the mitochondria activates caspase mediated apoptosis.[20,21] Cathepsins released from the lysosome can activate pro-apoptotic proteins, such as BID, which induce mitochondrial apoptosis.[22,23] Calcium released from the ER can also induce mitochondrial apoptosis.[24] Necrosis occurs when the ROS production is so great that the cell loses plasma membrane integrity before apoptosis can occur.

When the PS is activated while in the microvascular, the ROS produced can disrupt the tumor vasculature. Damage to endothelial cells cause them to release thrombin which clots the vessels,[11] starving the tumor of nutrients and oxygen it needs to proliferate. In addition, vascular PDT may aid in restoration normal tumor vasculature. Renormalization of tumor vasculature can aid in drug and oxygen delivery to the tumor, and has previously been achieved with anti-angiogenic drugs.[25]

Finally, the above two mechanism can produce an inflammatory response.[7,26,27] PDT activates the innate immune system through release of cytokines from tumor cells and tumor associated fibroblasts, resulting in the recruitment of macrophages and neutrophils. In addition, PDT can activate the adaptive immune system, through release of tumor antigens into the extracellular matrix. Tumor antigens then activate dendritic cell maturation[28] and, subsequently,

stimulate cytotoxic T cells against the tumor.[7,28]

1.2.5 Type I/II PDT

The mechanisms of tumor regression depend partially on the type of ROS produced. The first step in ROS production, is the absorption of light by a PS, exciting an electron from the ground singlet state to an excited singlet state (**Figure 2**). The electron can then relax back to the ground state through either emission of a photon, called fluorescence, or through non-radiative decay. A third option, is intersystem crossing (ISC) to the triplet state. ISC is considered a "forbidden" transition because it requires spin inversion which contradicts the Pauli exclusion principle. The low probability of spin inversion results in a long-lived (~μs to ms) triplet state. However, PSs have a higher probability of ISC than fluorophores, meaning they are more likely to populate that triplet state and less likely to emit fluorescent photons. Triplet state electrons can relax to the ground singlet state: through emitting a photon, this time called phosphorescence, through non-radiative decay, or through interactions with molecular oxygen. It is from the triplet state that ROS and free radicals are produced. The long-lived triplet state increases the probability that the election will be able to interact with its environment and produce ROS.

The two types of PDT reactions arise from the ability of the triplet state electron to either ionize substrates or react with molecular oxygen, called type I and type II reactions, respectively (**Figure 2**).[6] Most previous generation PSs rely on type II PDT, which produce singlet oxygen through spin-inversion. The triplet state electron reacts with triplet state oxygen, resulting in return of the electron to the lowest energy singlet state and the oxygen to the excited singlet state.[4,6] Type II PDT is only able to produce ROS when molecular oxygen is available and therefore is ineffective in hypoxic tumors (Section 1.3.2).
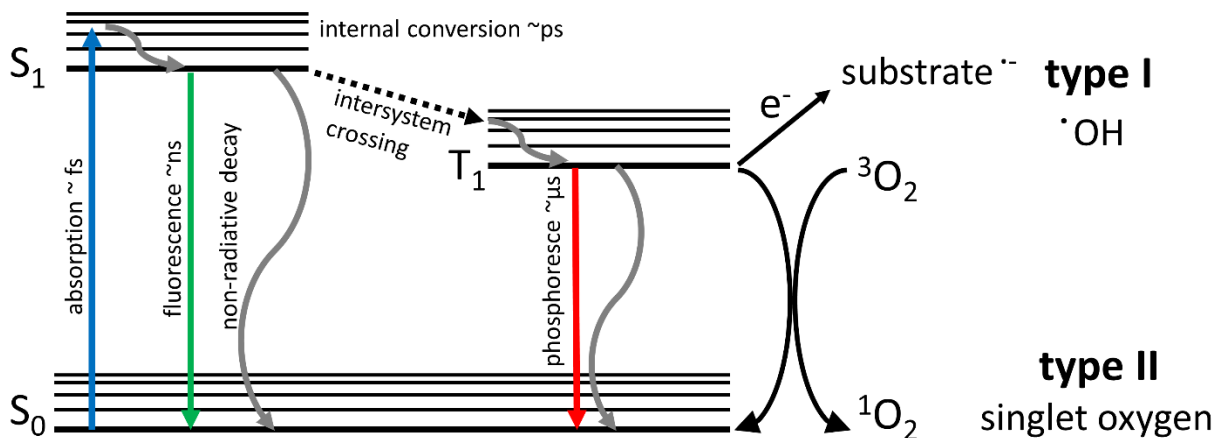
Figure 2. Type I and type II PDT reactions.

Fortunately, type I PDT provides an alternative oxygen independent pathway for producing ROS and free radicals. In type I reactions, the triplet state electron directly ionizes substrates, including biomolecules, to produce ROS such as hydroxyl radicals. Two emerging classes of PSs have higher rates of type I reactions, compared to porphyrin and chlorin based PSs. The first class are organometallic complexes, usually with ruthenium (II) or iridium (III), which have multiple long-lived triplet states, are electron donors, and are less dependent on oxygen to produce ROS.[29-33] The second class of PSs are metal oxide nanoparticles, such as TiO_2, which can catalytically produce potent hydroxyl radicals through the oxidation of water, and superoxide through the reduction of oxygen.[34,35]

1.3 The microenvironment of solid tumors

To develop better PDT strategies and understand the mechanism of subsequent tumor regression, it is important to understand two aspects of the tumor microenvironment: pH and hypoxia.

1.3.1 Acidic extracellular matrix

Tumors utilize enhanced glycolysis in lieu of oxidative phosphorylation for energy production. This is known as the Warburg Effect and causes a build-up of lactate in the cytosol

6

and subsequent decrease in intracellular pH (pHi). To maintain viable at a normal physiological pHi of 7.4, cancer cells actively pump out excess protons.[36] These protons are trapped in the tumor extracellular environment by poor lymphatic function and chaotic vascularization, resulting in a reduction in extracellular pH (pHe) to 6.2–6.9.[36-38]

The acidic pHe of tumors correlates with an aggressive phenotype, including increase in tumor invasiveness and cell proliferation, as well as a decrease in responsiveness to therapy.[36,39-42] However, neutralization of the tumor pHe, by oral administration of sodium bicarbonate can reduced tumor lesions and increase overall survival.[39,42-45] Therefore, the tumor's acidic pHe likely provides an environment that supports growth and metastasis.[46]

1.3.2 Hypoxia

Initially tumors are avascular limiting molecular oxygen delivery and resulting in wide spread hypoxia.[47-49] Moreover, as tumors grow, spatial disorganization of the vasculature produces intercapillary distances greater than the diffusion distance of oxygen creating heterogeneous pockets of hypoxia. Hypoxia occurs in both solid and hematologic tumors, including breast cancer,[50] multiple myeloma,[51] prostate cancer and pancreatic cancer.[52]

Prolonged tumor hypoxia can induce a pro-survival and anti-apoptotic phenotype, a switch to anabolic metabolism, epithelial-to-mesenchymal transitional, invasion, metastasis and the suppression of immune reactivity.[49] Ironically, while starving the tumor of oxygen, hypoxia also increases oxidative stress through the generation of ROS which promote DNA damage and genetic instability.[49]

In fact, hypoxia is one of the many mechanisms that causes tumor resistance to therapy. Radiation therapy and chemotherapy, that induce DNA breaks to induce cell death, both rely on oxygen to produce free radicals.[53] Therefore, to treat hypoxic tumors the dose for ionizing

radiation must be increased by 3-fold for equivalent cell killing.[54] Moreover, hypoxia induced genetic changes prompt resistance to other forms of therapy. For example, hypoxia stabilizes HIF-1, increasing expression of ABC transporters, and inducing multi-drug resistance.

New treatment methods are currently being explored to overcome the therapy resistance induced by hypoxia. One such paradigm, bioreductive prodrugs, are activated by enzyme reduction in hypoxic tissues to produce DNA damage.[49] A second approach uses small molecule inhibitors against pro-survival molecular targets expressed in hypoxic cells, such as HIF-1 and mTor.[55] Unfortunately, with both these approaches a substantial barrier is delivery of the drugs to the hypoxic, avascular regions of the tumor. An approach to overcome drug delivery is normalization of tumor vasculature, achieved through the use of pro- and anti-angiogenic drugs to restructure the tumor's abnormal vascularization into spatially and functionally normal.[25] Restoration of normal vasculature will additionally aid in delivery oxygen to all parts of the tumor.

1.4 Fluorescence sensors

In order to understand and study microenvironment of tumors, it is important to have methods to non-invasively characterize their phenotypes. Optical imaging using fluorescence sensors provides a method for studying the tumor biology from single cells to whole body imaging. Optical imaging can be conducted in real time with inexpensive instrumentation and non-ionizing radiation.[56,57] Fluorescence probes can be made for specific biomarkers and are sensitive (~pM).[56,57] There are several fluorescence based methods for in vivo measurements: fluorescence intensity, ratiometric fluorescence, and fluorescence lifetime.

1.4.1 Intensity based measurements

Single wavelength fluorescence intensity measurements require the simplest instrumentation, data acquisition, and analysis, but lack the ability for adequate quantification, mainly due to dependence on the concentration of the sensor. Ratiometric probes provide a solution to this problem by using a dual wavelength sensor and calculating the ratio of the fluorescence intensities at each wavelength.[58] While this method may work well in solution, wavelength dependent scattering and absorption can cause unpredictable changes in the ratiometric measurements when used for in vivo imaging.[59-61] In addition, it can be difficult to spectrally resolve short wavelength shifts.

1.4.2 Fluorescence lifetime based measurements

In contrast to intensity measurements, fluorescence lifetime is less dependent on the concentration of the fluorophore, instrumentation, and application.[60,62] Fluorescence lifetime is the average time an electron spends in an excited state before emitting a photon and returning to the ground state (**Figure 2**). Following first order kinetics, the average fluorescence lifetime is the time constant for an exponential decay (i.e. the time it takes for 36.8% of the excited electrons to repopulate the ground state.) Fluorescence lifetime measurements can detect conformational changes of proteins (e.g. bound vs unbound)[63] and molecular interactions (e.g. FRET).[60,62] It can also be used for multicomponent separations (e.g. to remove autofluorescence),[64] environmental sensing (e.g. oxygen, pH),[59,65] and tissue characterization by autofluorescence (e.g. collagen).[66]
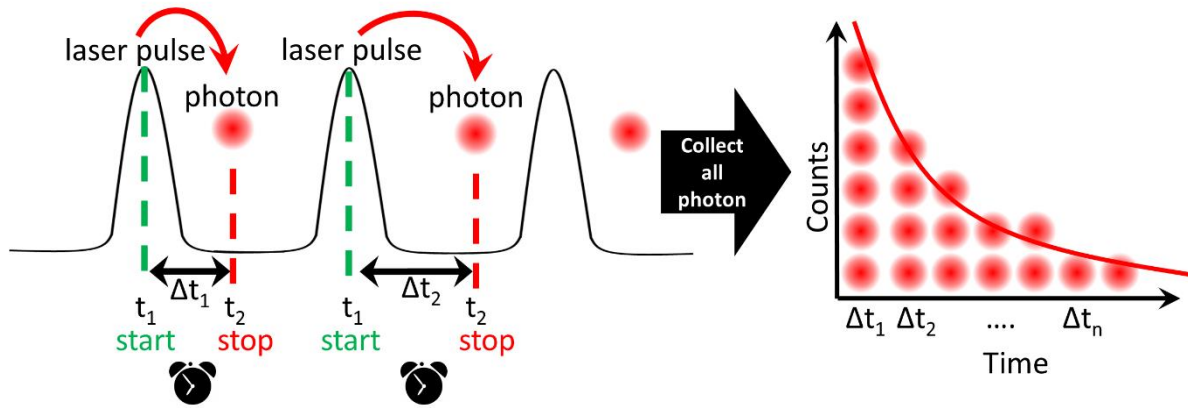
Figure 3. Time correlated single photon counting method of measuring fluorescence lifetime.

Fluorescence lifetime is measured in either the time[67] or frequency domain.[68] In the following studies, we use a time domain method and therefore it will be explained here (**Figure 3**). Time domain methods, including time correlated single photon counting (TCSPC), use complex timing in order to count single photons.[67] A pulsed laser (~70 ps) excites a fluorescence sample and the time of the excitation pulse is recorded as t_1. The excited sample emits a photon which is detected by an avalanche photodiode and the time of detection is recorded as t_2. The difference between these times, Δt, is binned into a histogram. This entire process is repeated thousands of times until the peak of the histogram reaches ~10,000 counts (or enough counts to obtain a reasonable exponential fit). The fluorescence lifetime is the time constant determined by fitting the histogram to an exponential decay. To construct an image using TCSPC, the laser is simply scanned over the entire image, to create a 3D data set (x,y,t).[67] This method can be used for spectroscopy, microscopy, and whole-body animal imaging.[60]

1.5 References

(1)   Ferlay, J.; Soerjomataram, I.; Dikshit, R.; Eser, S.; Mathers, C.; Rebelo, M.; Parkin, D. M.; Forman, D.; Bray, F. *Int. J. Cancer* **2015**, *136*, E359.

(2)   Weigelt, B.; Peterse, J. L.; van 't Veer, L. J. *Nature reviews. Cancer* **2005**, *5*, 591.

(3)   Mehlen, P.; Puisieux, A. *Nature reviews. Cancer* **2006**, *6*, 449.

(4)   Dabrowski, J. M.; Arnaut, L. G. *Photochem. Photobiol. Sci.* **2015**, *14*, 1765.

(5)   Obaid, G.; Broekgaarden, M.; Bulin, A. L.; Huang, H. C.; Kuriakose, J.; Liu, J.; Hasan, T. *Nanoscale* **2016**, *8*, 12471.

(6)   Dolmans, E. J. G. J. D.; Fukumura, D.; Jain, R. K. *Nat. Rev. Cancer* **2003**, *3*, 380.

(7)   Castano, A. P.; Mroz, P.; Hamblin, M. R. *Nat. Rev. Cancer* **2006**, *6*, 535.

(8)   Agostinis, P.; Berg, K.; Cengel, K. A.; Foster, T. H.; Girotti, A. W.; Gollnick, S. O.; Hahn, S. M.; Hamblin, M. R.; Juzeniene, A.; Kessel, D.; Korbelik, M.; Moan, J.; Mroz, P.; Nowis, D.; Piette, J.; Wilson, B. C.; Golab, J. *Ca-Cancer J. Clin.* **2011**, *61*, 250.

(9)   Allison, R. R.; Sibata, C. H. *Photodiagn. Photodyn. Ther.* **2010**, *7*, 61.

(10)   Huang, Z. *Technol. Cancer Res. Treat.* **2005**, *4*, 283.

(11)   Schmidt-Erfurth, U.; Hasan, T. *Surv. Ophthalmol.* **2000**, *45*, 195.

(12)   Allison, R. R.; Downie, G. H.; Cuenca, R.; Hu, X.-H.; Childs, C. J. H.; Sibata, C. H. *Photodiagn. Photodyn. Ther.* **2004**, *1*, 27.

(13)   Spring, B. Q.; Abu-Yousif, A. O.; Palanisami, A.; Rizvi, I.; Zheng, X.; Mai, Z.; Anbil, S.; Sears, R. B.; Mensah, L. B.; Goldschmidt, R.; Erdem, S. S.; Oliva, E.; Hasan, T. *Proc. Natl. Acad. Sci. U. S. A.* **2014**, *111*, E933.

(14)   Spring, B. Q.; Bryan Sears, R.; Zheng, L. Z.; Mai, Z.; Watanabe, R.; Sherwood, M. E.; Schoenfeld, D. A.; Pogue, B. W.; Pereira, S. P.; Villa, E.; Hasan, T. *Nat. Nanotechnol.* **2016**, *11*, 378.

(15)   Lou, P.-J.; Jones, L.; Hopper, C. *Technol. Cancer Res. Treat.* **2003**, *2*, 311.

(16)   Kelty, C. J.; Marcus, S. L.; Ackroyd, R. *Diseases of the Esophagus* **2002**, *15*, 137.

(17)   Lustig, R. A.; Vogl, T. J.; Fromm, D.; Cuenca, R.; Alex Hsi, R.; D'Cruz, A. K.; Krajina, Z.; Turic, M.; Singhal, A.; Chen, J. C. *Cancer* **2003**, *98*, 1767.

(18)   Moore, C. M.; Pendse, D.; Emberton, M. *Nat. Clin. Pract. Urol.* **2009**, *6*, 18.

(19)   Wang, L. V.; Wu, H.-i. *Biomedical Optics: Principles and Imaging*; John Wiley & Sons, Inc.: Hoboken, New Jersey, 2012.

(20)   Tait, S. W.; Green, D. R. *Nat. Rev. Mol. Cell Biol.* **2010**, *11*, 621.

(21)   Orrenius, S.; Zhivotovsky, B. *Nat. Chem. Bio.* **2005**, *1*, 188.

(22)   Liu, L.; Zhang, Z.; Xing, D. *Free Radic. Biol. Med.* **2011**, *51*, 53.

(23)   Aits, S.; Jaattela, M. *J. Cell Sci.* **2013**, *126*, 1905.

(24)   Kim, I.; Xu, W.; Reed, J. C. *Nat. Rev. Drug Discov.* **2008**, *7*, 1013.

(25)   Jain, R. K. *Science* **2005**, *307*, 58.

(26)   Barathan, M.; Mariappan, V.; Shankar, E. M.; Abdullah, B. J.; Goh, K. L.; Vadivelu, J. *Cell Death Dis.* **2013**, *4*, e697.

(27)   Garg, A. D.; Krysko, D. V.; Vandenabeele, P.; Agostinis, P. *Cancer Immunol. & Immunother.* **2012**, *61*, 215.

(28)   Pockley, A. G. *Lancet.* **2003**, *362*, 469.

(29)   Lincoln, R.; Kohler, L.; Monro, S.; Yin, H.; Stephenson, M.; Zong, R.; Chouai, A.; Dorsey, C.; Hennigar, R.; Thummel, R. P.; McFarland, S. A. *J. Am. Chem. Soc.* **2013**, *135*, 17161.

(30)   Reichardt, C.; Pinto, M.; Wachtler, M.; Stephenson, M.; Kupfer, S.; Sainuddin, T.; Guthmuller, J.; McFarland, S. A.; Dietzek, B. *J. Phys. Chem. A* **2015**, *119*, 3986.

(31)   Stephenson, M.; Reichardt, C.; Pinto, M.; Wachtler, M.; Sainuddin, T.; Shi, G.; Yin, H.; Monro, S.; Sampson, E.; Dietzek, B.; McFarland, S. A. *The journal of physical chemistry. A* **2014**, *118*, 10507.

(32)   Shi, G.; Monro, S.; Hennigar, R.; Colpitts, J.; Fong, J.; Kasimova, K.; Yin, H.; DeCoste, R.; Spencer, C.; Chamberlain, L.; Mandel, A.; Lilge, L.; McFarland, S. A. *Coor. Chem. Rev.* **2015**, *282-283*, 127.

(33)   Sun, Y.; Joyce, L. E.; Dickson, N. M.; Turro, C. *Chem. Commun.* **2010**, *46*, 2426.

(34)   Kotagiri, N.; Sudlow, G. P.; Akers, W. J.; Achilefu, S. *Nat. Nanotechnol.* **2015**, *10*, 370.

(35)   Nosaka, Y.; Nosaka, A. Y. In *Photocatalysis and Water Purification: From Fundamentals to Recent Applications*; Pichat, P., Ed.; Wiley-VCH Verlag GmbH & Co. KGaA: Weinheim, Germany, 2013, p 1.

(36)   Cardone, R. A.; Casavola, V.; Reshkin, S. J. *Nat. Rev. Cancer* **2005**, *5*, 786.

(37)   Gillies, R. J.; Raghunand, N.; Karczmar, G. S.; Bhujwalla, Z. M. *J. Magn. Reson. Imaging* **2002**, *16*, 430.

(38)   Gilson, R. C.; Tang, R.; Som, A.; Klajer, C.; Sarder, P.; Sudlow, G. P.; Akers, W. J.; Achilefu, S. *Molecular pharmaceutics* **2015**, *12*, 4237.

(39)   Robey, I. F.; Baggett, B. K.; Kirkpatrick, N. D.; Roe, D. J.; Dosescu, J.; Sloane, B. F.; Hashim, A. I.; Morse, D. L.; Raghunand, N.; Gatenby, R. A.; Gillies, R. J. *Cancer Res.* **2009**, *69*, 2260.

(40)   Wu, X. L.; Kim, J. H.; Koo, H.; Bao, S. M.; Shin, H.; Kim, M. S.; Lee, B.-H.; Park, R.-W.; Kim, I.-S.; Choi, K.; Kwon, I. C.; Kim, K.; Lee, D. S. *Bioconjug. Chem.* **2010**, *21*.

(41)   Raghunand, N.; He, X.; Sluis, R.; Mahoney, B.; Baggett, B.; Taylor, C.; Paine-Murrieta, G.; Roe, D.; Bhujwalla, Z.; Gillies, R. *Brit. J. Cancer* **1999**, *80*, 6.

(42)   Robey, I. F.; Nesbit, L. A. *Biomed. Res. Int.* **2013**, *2013*, 485196.

(43)   Muller, V.; Riethdorf, S.; Rack, B.; Janni, W.; Fasching, P. A.; Solomayer, E.; Aktas, B.; Kasimir-Bauer, S.; Zeitz, J.; Pantel, K.; Fehm, T. *Breast Cancer Res.* **2011**, *13*, R71.

(44)   Neri, D.; Supuran, C. T. *Nat. Rev. Drug Discov.* **2011**, *10*, 767.

(45)   Robey, I. F.; Martin, N. K. *BMC cancer* **2011**, *11*, 235.

(46)   Webb, B. A.; Chimenti, M.; Jacobson, M. P.; Barber, D. L. *Nat. Rev. Cancer* **2011**, *11*, 671.

(47)   Maxwell, P. H.; Dachs, G. U.; Gleadle, J. M.; Nicholls, L. G.; Harris, A. L.; Stratford, I. J.; Hankinson, O.; Pugh, C. W.; Ratcliffe, P. J. *Proc. Natl. Acad. Sci. U S A* **1997**, *94*, 8104.

(48)   Hockel, M.; Vaupel, P. *J. Natl. Cancer Inst.* **2001**, *93*, 266.

(49)   Wilson, W. R.; Hay, M. P. *Nat. Rev. Cancer* **2011**, *11*, 393.

(50)   Semenza, G. L. *Biochim. Biophys. Acta* **2016**, *1863*, 382.

(51)   Hu, J.; Van Valckenborgh, E.; Menu, E.; De Bruyne, E.; Vanderkerken, K. *Dis. Model & Mech.* **2012**, *5*, 763.

(52)   Erickson, L. A.; Highsmith, W. E., Jr.; Fei, P.; Zhang, J. *Drug Des. Devel. Ther.* **2015**, *9*, 2029.

(53)   Teicher, B. A.; Lazo, J. S.; Sartorelli, A. C. *Cancer Res.* **1981**, *41*, 73.

(54)   Gray, L. H.; Conger, A. D.; Ebert, M.; Hornsey, S.; Scott, O. C. A. *Br. J. Radiol.* **1953**, *26*, 638.

(55)   Tennant, D. A.; Duran, R. V.; Gottlieb, E. *Nat. Rev. Cancer* **2010**, *10*, 267.

(56)   Terai, T.; Nagano, T. *Curr. Opin. Chem. Biol.* **2008**, *12*, 515.

(57)   Zhang, X.; Bloch, S.; Akers, W.; Achilefu, S. *Curr. Protoc. Cytom.* **2012**, *Chapter 12*, Unit12 27.

(58)   Han, K.; Wang, S. B.; Lei, Q.; Zhu, J. Y.; Zhang, X. Z. *ACS Nano* **2015**, *9*, 10268.

(59)   Orte, A.; Alvarez-Pez, J. M.; Ruedas-Rama, M. J. *ACS Nano* **2013**, *7*, 6387.

(60)   Sarder, P.; Maji, D.; Achilefu, S. *Bioconjug. Chem.* **2015**, *26*, 963.

(61)   Izquierdo, M. A.; Aurimas, V.; Lermontova, S. A.; Grigoryev, S.; Shilyagina, N. Y.;

Balalaeva, I. V.; Klapshina, L. G.; Kuimova, M. K. *J. Mater. Chem. B.* **2015**, *8*, 1089.

(62)   Berezin, M.; Achilefu, S. *Chem. Rev.* **2010**, *110*, 2641.

(63)   Calleja, V.; Ameer-Beg, S. M.; Vojnovic, B.; Woscholski, R.; Downward, J.; Larijani, B.

Biochem J. **2003**, *372*, 33.

(64)   Kumar, A. T. N.; Chung, E.; Raymond, S. B.; Water, J. A. J. M. v. d.; Shah, K.;

Fukumura, D.; Jain, R. K.; Bacskai, B. J.; Boas, D. A. *Opt. Lett.* **2009**, *34*, 2066.

(65)   Szmacinski, H.; Lakowicz, J. R. *Sens. Actuators, B* **1995**, *29*, 16.

(66)   Schweitzer, D.; Schenke, S.; Hammer, M.; Schweitzer, F.; Jentsch, S.; Birckner, E.;

Becker, W.; Bergmann, A. *Microsc. Res. Tech.* **2007**, *5*, 410.

(67)   Suhling, K.; French, P. M.; Phillips, D. *Photochem. Photobio.l Sci.* **2005**, *4*, 13.

(68)   Gadella, T. W. J.; Jovin, T. M.; Clegg, R. M. *Biophys. Chem.* **1993**, *48*, 221.

Chapter 2 : Hybrid TiO₂-Ruthenium Nano-photosensitizer Synergistically Produces Reactive Oxygen Species in Both Hypoxic and Normoxic Conditions

This chapter is based on a pending article:

2.1 Chapter summary

Photodynamic therapy (PDT) is widely used to treat diverse diseases, but its dependence on oxygen to produce cytotoxic reactive oxygen species (ROS) diminishes the therapeutic effect in a hypoxic environment such as solid tumors. Here, we developed a ROS-producing hybrid nanoparticle-based photosensitizer capable of maintaining high levels of ROS under both normoxic and hypoxic conditions. Conjugation of an organometallic ruthenium complex (N3), a photo-inducible electron donor, to a TiO_2 nanoparticle, an efficient ROS generator, afforded TiO_2-N3. Upon exposure of TiO_2-N3 to light, the N3 injected electrons into TiO_2 to produce three- and four-fold greater hydroxyl radicals and hydrogen peroxide, respectively, than TiO_2 at 160 mmHg. Whereas TiO_2 was unable to generate hydrogen peroxide and only able to produced small amounts of hydroxyl radicals at low oxygen tension (8 mmHg), TiO_2-N3 maintained three-fold higher hydroxyl radicals via N3-facilitated electron hole reduction of adsorbed water molecules and an efficient conversion of low oxygen concentration into hydroxyl radicals to increase the net concentration of this ROS. All the photosensitizers produced high levels of singlet oxygen, except under hypoxic conditions. We delineated the various pathways that TiO_2-N3 uses to enhance hydroxyl production and maintain a significant level of these species in both normoxic and hypoxic conditions. This work demonstrates that the incorporation of N3 transformed TiO_2 from a dual type I and II PDT agent to a predominantly type I photosensitizer, irrespective of the oxygen content. Our findings could enable the application of this strategy to develop highly efficient nano-photosensitizers for PDT.

2.2 Hybrid TiO2-ruthenium nano-photosensitizer synergistically produces reactive oxygen species in both hypoxic and normoxic conditions

ROS are products of normal metabolic processes in living organisms. At low concentrations, these species play vital roles in cell signaling, but they can become cytotoxic at elevated levels via reaction with proteins, DNAs, lipids, and other biological molecules. PDT is a treatment paradigm that selectively elevates ROS levels to induce cell death by multiple pathways.[1] Some molecules, known as photosensitizers (PSs), absorb light of the appropriate wavelengths to produce cytotoxic free radicals and ROS. Many organic PSs mainly produce singlet oxygen ($^1O_2$) formed via spin inversion of triplet oxygen to singlet oxygen (type II PDT).[2] Specific organic PSs can also produce hydrogen peroxide (H_2O_2) and hydroxyl ($^{\bullet}OH$) radicals, formed from direct ionization events (type I PDT).[2] While the highly reactive $^{\bullet}OH$ and $^1O_2$ rapidly interact with adjacent biomolecules to disrupt normal cell functions and induce cell death, the more stable H_2O_2 can travel across cell membranes.[3] Intracellular scavengers, such as catalases or peroxidases can convert H_2O_2 to superoxide radicals.[4] However, ferrous ions can rapidly oxidize H_2O_2 to reactive $^{\bullet}OH$ radicals (Fenton reaction) to enhance the PDT effect, especially in tumor cells where the increased demand for iron is high.[5] Despite these advantages, the reliance of many organic PSs on molecular oxygen limits the effectiveness of PDT in hypoxic environments, which include many solid tumors.[6] During PDT, local oxygen is rapidly consumed, creating transient hypoxia that further decreases the therapeutic effects.[7] Moreover, most organic PSs can react with $^1O_2$ produced during PDT, leading to a depletion of the PSs' concentration via a photobleaching process.[8] As a result, a recent trend in PDT research includes the development of new PSs that are capable of producing cytotoxic ROS, irrespective of the oxygenation status of the microenvironment.

Some studies have shown that organometallic PSs can damage DNA under normoxic and hypoxic conditions.[9] One of such complexes is *cis*-bis(isothiocyanato)bis(2,2'-bipyridyl-4,4'-dicarboxylato)ruthenium(II), abbreviated N3. This complex, which absorbs light in the UV and visible wavelengths, possesses multiple triplet states that can be populated by both metal to ligand charge transfer (^{3}MLCT) and intra-ligand charge transfer ($^3\pi$-π*) mechanisms.[10] Organometallic PSs have long triplet state lifetimes (~ms) that enhances the interaction with oxygen species and subsequent ROS production.[11] Although N3 can produce damage regardless of molecular oxygen content, metal oxides such as TiO_2 produce higher amounts of ROS in the presence of oxygen. The excitation of TiO_2 with radiative energy greater than its band gap of 3.2 eV (387 nm) promotes an electron to the conduction band, creating an electron hole pair.[12] The electrons primarily reduce adsorbed molecular oxygen to superoxide, and the holes largely oxidize substrates such water into a hydrogen ion and an $^\bullet$OH.[12] These processes allow TiO_2 to produce higher amounts of diverse ROS compared to traditional small molecule PS, making TiO_2 a viable PDT agent. However, hypoxic conditions significantly deplete the amount of ROS that TiO_2 forms.

In this study, we synthesized TiO_2-N3 nanoparticles, consisting of a regenerative ROS-producing TiO_2 core that is coated with N3 to enhance ROS production at different levels of oxygen pressure. TiO_2 materials are excellent electron acceptors from organometallic ruthenium complexes, a phenomenon that has been used for converting sunlight into current.[13] By coating the surface of TiO_2 nanoparticles with N3, each ruthenium complex can inject an electron into TiO_2, building up electrons that increase ROS production.[12, 13b, 14]

TiO_2-N3 nanoparticles were prepared by shaking a mixture of 25 nm sized anatase TiO_2 particles and N3 in an ethanol overnight. The particles were then centrifuged and the supernatant discarded, followed by the addition of water to the residue. Subsequent sonication (45 seconds)

19

dispersed and evenly coat the particles. Filtration through a 0.45 um pore removed large aggregates. The absorption spectra of N3 blue-shifts when coated on TiO_2, suggesting that TiO_2 increased the excited state energies of the N3 (**Figure 4a**). The TiO_2-N3 particles contain an average of 125,000 N3 molecules per nanoparticle (**Figure 4b**) with an average hydrodynamic size of 135 nm based on dynamic light scattering measurement (**Figure 4c**). Transmission electron microscopy of TiO_2-N3 showed that the 25 nm TiO_2 cores were maintained in the 135 nm clusters. (**Figure 4d**).
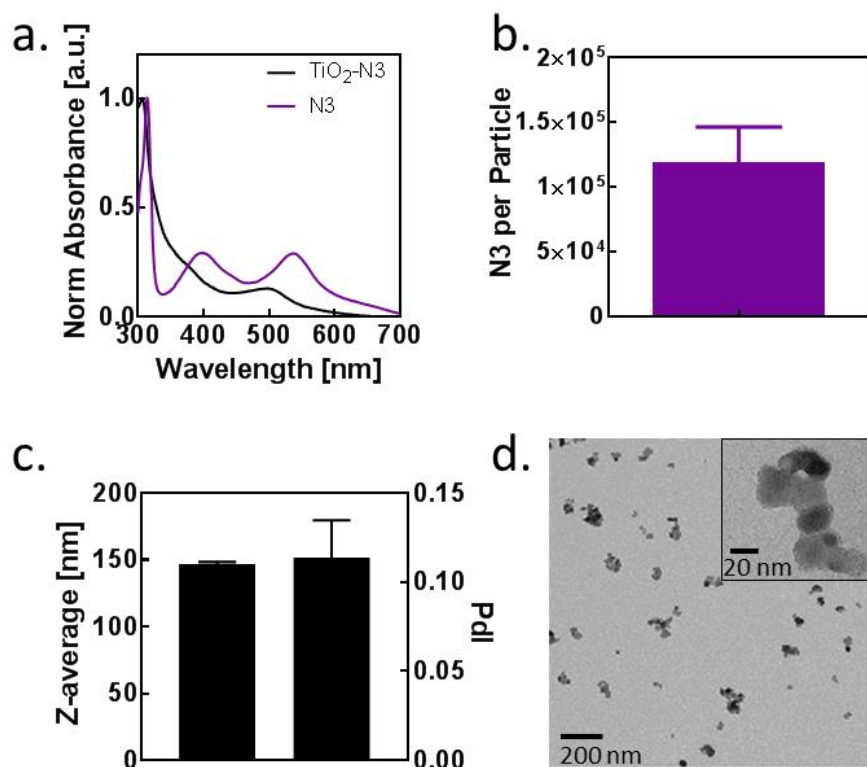
Figure 4. Characterization of TiO_2-N3 nanoparticles. (a) Absorption spectra for N3 and TiO_2-N3. (b) Number of N3 incorporated into a 25 nm TiO_2 particle. (c) Average size of TiO_2-N3 particles after sonication and filtering. (d) Transmission electron microscopy of TiO_2-N3 particles.

To determine the ROS produced by TiO$_2$-N3, bare TiO$_2$, and N3, we used hydroxyphenyl fluorescein (HPF), singlet oxygen sensor green (SOSG), and Amplex Red assay for $^\bullet$OH, ^{1}O$_2$, and H$_2$O$_2$, respectively. For these assays TiO$_2$-N3 was not sonicated or filtered. A solution of 10 µM HPF or SOSG and PS (0.1 mg/mL TiO$_2$, 0.1 mg/mL TiO$_2$-N3, or 7 µM N3) was irradiated at 1.69 mW/cm^2 using a 365 nm light source. For $^\bullet$OH, measurements, aliquots of 100 µL of HPF were diluted in Tris buffer (pH 8.0; 900 µL) at different time points (**Figure 6a**) and the fluorescence of each sample was measured at ex/em 478/515 nm. ^{1}O$_2$ measurements were accomplished by irradiating SOSG in a quartz cuvette continuously for 60 min and the fluorescence was measured every 1 min (ex/em 504/525 nm). H$_2$O$_2$ measurements were performed in a 96 well plate (50 µL) using the same concentrations of each PS as above and an irradiation power of 2.39 mW/cm^2. The fluorescence at ex/em 545/590 nm and a reference standard were used to calculate the concentration of H$_2$O$_2$ in each well. To quantify the amount of the different types of ROS produced, each activation curve was fitted to an exponential plot (**Figure 6a-c**).
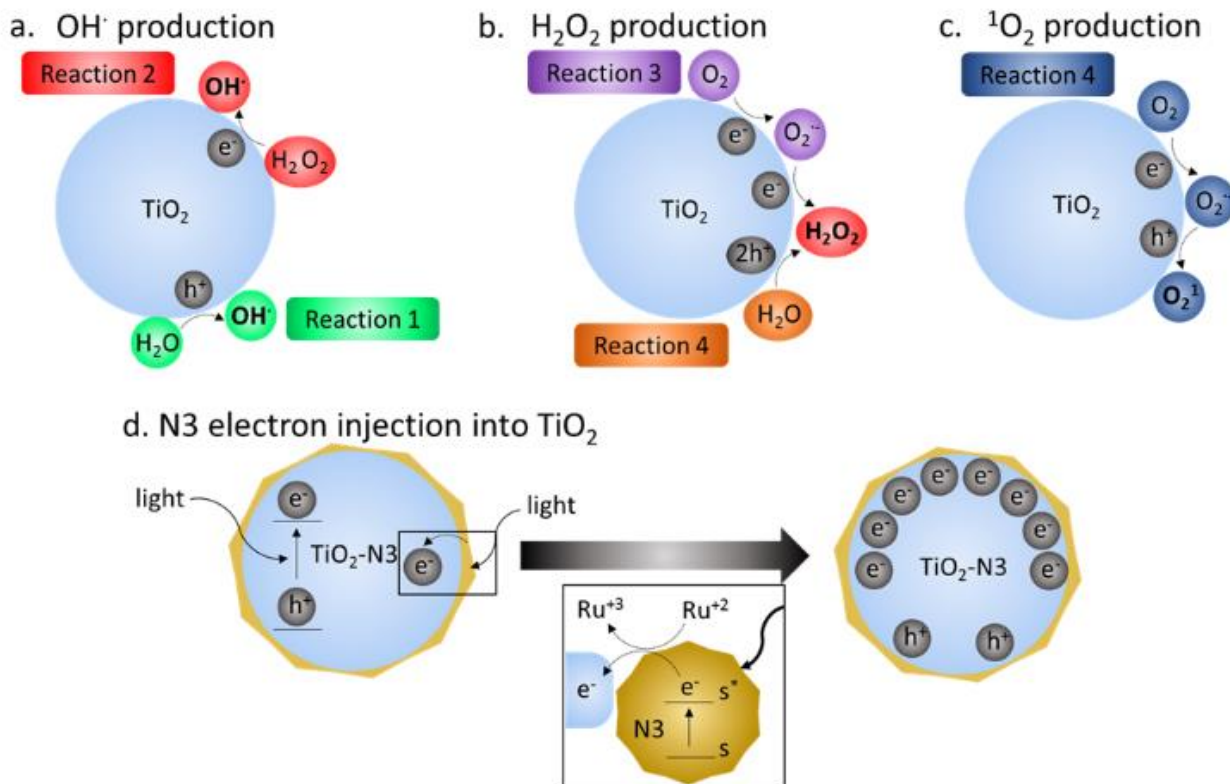
Figure 5. Schematic description of ROS generation by TiO_2 and electron injection to TiO_2 by N3.

Figure 5 illustrates the different pathways to generate ROS ($^{\bullet}OH$, H_2O_2, and $^1O_2$) from TiO_2-N3. Under normal oxygen pressure (160 mmHg), the photo-activation of TiO_2-N3 resulted in about 3-fold higher $^{\bullet}OH$ production compared to TiO_2 and N3 (**Figure 6a**). These radicals could be produced by two mechanisms. Reaction 1 is a one-step oxidation of water to a $^{\bullet}OH$, a primary pathway used by bare TiO_2 nanoparticles (**Figure 5a**). The observed increase in $^{\bullet}OH$ suggested the involvement of another mechanism, Reaction 2, which reduces a precursor H_2O_2 to an $^{\bullet}OH$. Two pathways are available for H_2O_2 formation (**Figure 5b**). In Reaction 3, two conduction band electrons from TiO_2 are used to first reduce oxygen to superoxide, which is subsequently reduced to H_2O_2. In the second mechanism, Reaction 4, two holes on the TiO_2 nanoparticles oxidize adsorbed water molecules to H_2O_2. The complementary molecular oxygen dependent (Reaction 3)

22

and independent (Reaction 4) pathways to produce H_2O_2 ensures the generation of hydroxyl radicals. The bare TiO_2 particles probably rely more on Reaction 1 than 2 for $^\bullet OH$ production because of the direct oxidation of abundant water molecules. Alternatively, the TiO_2 in TiO_2-N3 has higher numbers of conduction band elections due to the injection of electrons from photo-activated N3. This process creates more electrons for Reactions 3 and 2, accounting for the observed 3-fold increase in the $^\bullet OH$ produced (**Figure 5d**).

We next postulated that the high $^\bullet OH$ levels in TiO_2-N3 are associated with a corresponding increase in H_2O_2 production. Upon photoactivation, TiO_2-N3 generated about 4-fold higher H_2O_2 than TiO_2 (**Figure 6b**). The low yield of H_2O_2 from N3 indicates that its contribution to $^\bullet OH$ production was minimal. These results support a mechanism where N3 injected electrons into TiO_2 to increase the conversion of oxygen to H_2O_2 via Reaction 3 and a rapid transformation of H_2O_2 to $^\bullet OH$ through Reaction 2.
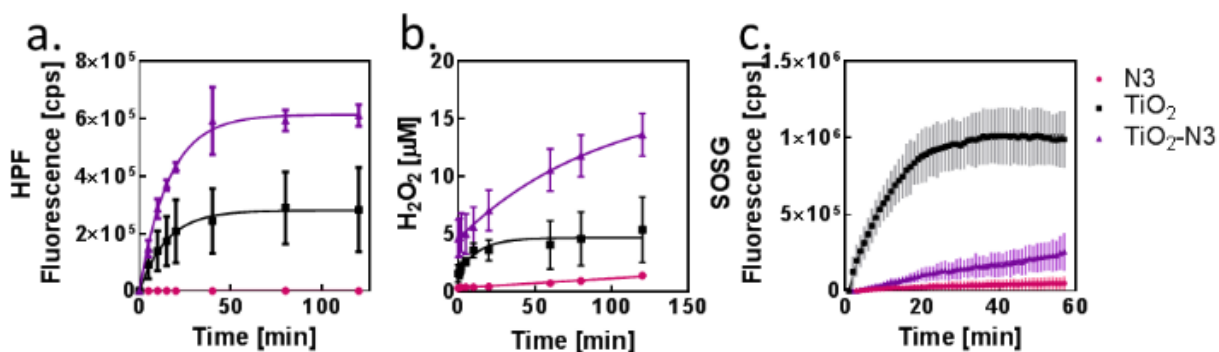
Figure 6. ROS production and characterization. Time course of (a) hydroxyl radical, (b) hydrogen peroxide, and (c) singlet oxygen production, respectively, as PSs are irradiated with 365 nm light.

The other reactive ROS, $^1O_2$, is the primary species involved in oxygen dependent type II PDT. The ease of electron–hole pair generation upon exposure of TiO_2 nanoparticles to light,

facilitates concerted reduction of oxygen to super oxide and subsequent oxidation to $^1O_2$ (**Figure 5c**). Expectedly, our results show that TiO_2-generated $^1O_2$ was an order of magnitude higher than TiO_2-N3 or N3 (**Figure 6c**). In contrast to the synergistic effects of N3 on $^\bullet OH$ and H_2O_2 production by TiO_2-N3, N3 effectively inhibited $^1O_2$ generation. Alone, N3 can produce singlet oxygen through intersystem crossing to the triplet state and spin-inversion of the triplet state of N3 and triplet state of oxygen. Whereas this process takes place on the time scale of microseconds,[11] electron injection into TiO_2 occurs on the time scale femtoseconds.[15] As a result, when N3 is adsorbed onto TiO_2, the probability of electron injection is higher than intersystem crossing and spin-inversion. Thus, N3 favors reduction reactions, which enhances H_2O_2 production that is subsequently used to increase $^\bullet OH$. Effectively, N3 converts TiO_2 from a dual type I and II PDT agent to a predominantly type I PS under normoxic conditions.
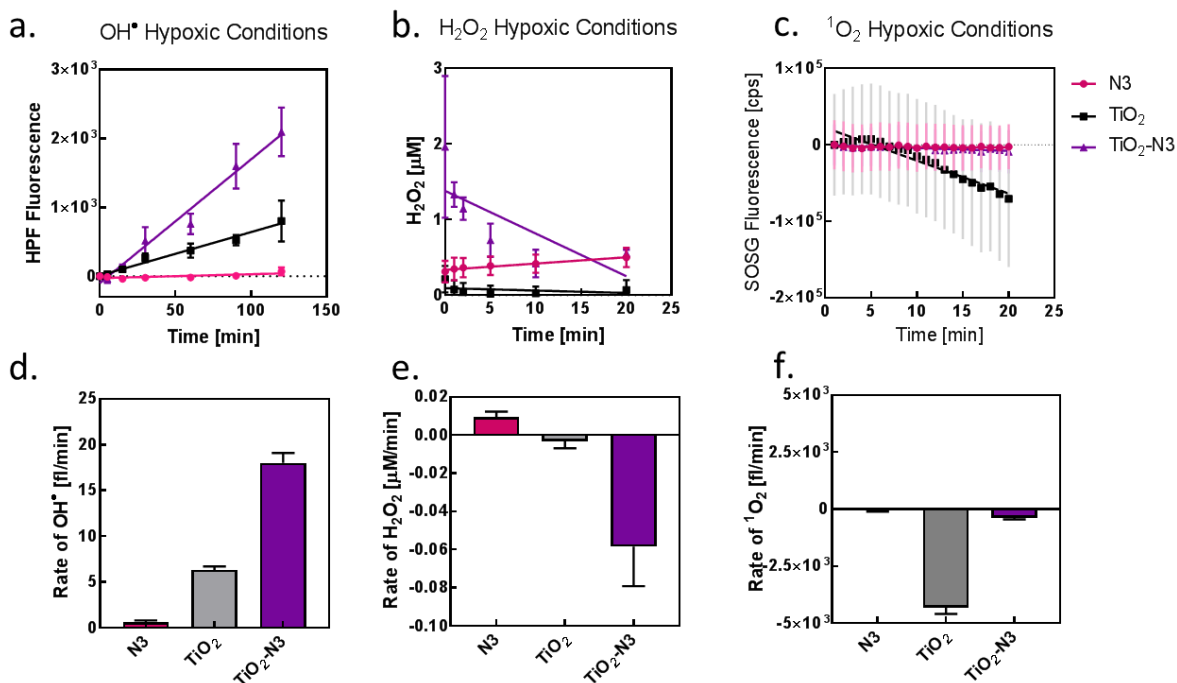
Figure 7. Oxygen dependence on hydroxyl radical production. ROS production of (a) hydroxyl radical, (b) hydrogen peroxide, and (c) singlet oxygen at 8 mmHg oxygen pressure. Rate of (d)

hydroxyl radical, (e) hydrogen peroxide, and (f) singlet oxygen production under hypoxic conditions.

To test the performance of the PSs under severe hypoxic conditions, we bubbled nitrogen in a suspension of the PSs and the appropriate sensors to attain 8 mmHg for all ROS measurements. For H_2O_2 and $^{\bullet}OH$ measurements, the solution was then added to a 96-well plate and incubated in 8 mmHg oxygen pressure atmosphere for an hour. Measurements were taken at different time points after UV irradiation of the solution (**Figure 7**). We found that the $^{\bullet}OH$ production followed the same trend as in normoxic conditions, with TiO_2-N3 generating about 3-fold greater $^{\bullet}OH$ than either TiO_2 or N3 (**Figure 7a**). In addition, the rate of $^{\bullet}OH$ production for TiO_2-N3 was 3-fold higher than TiO_2. These results demonstrate that the reductive effect of N3 on TiO_2 allowed the efficient utilization of oxygen, even at low pressures, to maintain $^{\bullet}OH$ production (**Figure 7d**).

N3 was the only PS that generated H_2O_2 in hypoxic conditions (**Figure 7b, e**). The slopes of H_2O_2 generation for TiO_2 and TiO_2-N3 were both negative in hypoxic conditions, indicating a decrease in baseline H_2O_2 over time. The dependence of the initial on the reduction of oxygen reaction to produce H_2O_2 led to the observed effect for TiO_2 or TiO_2-N3 (Reaction 3). Irrespective of the PS used, the minimal availability of molecular oxygen under hypoxic conditions prevented the production of $^1O_2$ (**Figure 7c, f**).

This work demonstrates that combining the two PSs resulted in changes to their photophysical properties, which altered both the type and amount of ROS produced. It also delineates the various pathways that TiO_2-N3 uses to enhance •OH production and maintain a significant level of these species in normoxic and hypoxic conditions. The addition of N3 to TiO_2 causes a build-up of electrons on the TiO_2 surface, which likely accounts for the synergistic production of H_2O_2 and •OH (**Figure 6a, b** and **Figure 5d**). Furthermore, the inability of TiO_2 to

25

produce H_2O_2 under hypoxic conditions suggests that N3 facilitated the depletion of residual H_2O_2 (**Figure 7b, e**) and the rapid conversion of the low oxygen concentration into •OH, thus increasing the concentration of this species (**Figure 7a, d**). The ensemble of these results demonstrates a mechanism to convert and maintain cytotoxic •OH production by harnessing the reductive power of ruthenium complexes, which efficiently reduces low levels of oxygen for ROS production. Our findings could enable the application of this strategy to develop highly efficient nano-photosensitizers in the future for PDT.

2.3 Acknowledgments

2.4 References

(1)   Castano, A. P.; Mroz, P.; Hamblin, M. R. *Nat. Rev. Cancer* **2006**, *6*, 535.

(2)   Dolmans, E. J. G. J. D.; Fukumura, D.; Jain, R. K. *Nat. Rev. Cancer* **2003**, *3*, 380.

(3)   Fisher, A. B. *Antioxid. Redox Signal* **2009**, *6*, 1349.

(4)   Halliwell, B. *Annu. Rev. Nutr.* **1996**, *16*, 33.

(5)   Torti, S. V.; Torti, F. M. *Nat. Rev. Cancer* **2013**, *13*, 342.

(6)   Hardee, M. E.; Dewhirst, M. W.; Agarwal, N.; Sorg, B. S. *Curr. Mol. Med.* **2009**, *9*, 435.

(7)   Hanahan, D.; Weinberg, R. A. *Cell* **2011**, *144*, 646.

(8)   Maxwell, P. H.; Dachs, G. U.; Gleadle, J. M.; Nicholls, L. G.; Harris, A. L.; Stratford, I. J.; Hankinson, O.; Pugh, C. W.; Ratcliffe, P. J. *Proc. Natl. Acad. Sci. U S A* **1997**, *94*, 8104.

(9)   Mitra, S.; Foster, T. *Neoplasia* **2008**, *10*, 429.

(10)   Celli, J. P.; Spring, B. Q.; Rizvi, I.; Evans, C. L.; Samkoe, K. S.; Verma, S.; Pogue, B. W.; Hasan, T. *Chem. Rev.* **2010**, *110*, 2795.

(11)   Obaid, G.; Broekgaarden, M.; Bulin, A. L.; Huang, H. C.; Kuriakose, J.; Liu, J.; Hasan, T. *Nanoscale* **2016**, *8*, 12471.

(12)   Potter, W. R.; Mang, T. S.; Dougherty, T. J. *Photochem. and Photobiol.* **1987**, *46*, 97.

(13)   Sun, Y.; Joyce, L. E.; Dickson, N. M.; Turro, C. *Chem. Commun.* **2010**, *46*, 2426.

(14)   Shi, G.; Monro, S.; Hennigar, R.; Colpitts, J.; Fong, J.; Kasimova, K.; Yin, H.; DeCoste, R.; Spencer, C.; Chamberlain, L.; Mandel, A.; Lilge, L.; McFarland, S. A. *Coor. Chem. Rev.* **2015**, *282-283*, 127.

(15)   Lv, W.; Zhang, Z.; Zhang, K. Y.; Yang, H.; Liu, S.; Xu, A.; Guo, S.; Zhao, Q.; Huang, W. *Angew. Chem. Int. Ed.* **2016**, *55*, 9947.

(16)   Fantacci, S.; De Angleis, F.; Selloni, A. *J. Am. Chem. Soc.* **2003**, *125*, 4008.

(17)   Lincoln, R.; Kohler, L.; Monro, S.; Yin, H.; Stephenson, M.; Zong, R.; Chouai, A.; Dorsey, C.; Hennigar, R.; Thummel, R. P.; McFarland, S. A. *J. Am. Chem. Soc.* **2013**, *135*, 17161.

(18)   Nosaka, Y.; Nosaka, A. Y. In *Photocatalysis and Water Purification: From Fundamentals to Recent Applications*; Pichat, P., Ed.; Wiley-VCH Verlag GmbH & Co. KGaA: Weinheim, Germany, 2013, p 1.

(19)   O'Regan, B.; Grätzel, M. *Nature* **1991**, *353*, 737.

(20)   Katoh, R.; Furube, A.; Yoshihara, T.; Hara, K.; Fujihashi, G.; Takano, S.; Murata, S.; Arakawa, H.; Tachiya, M. *J. Phys. Chem. B* **2003**, *108*, 4848.

(21)   He, Y. L.; Wang, S.; Zhang, L.; Xin, J.; Wang, J.; Yao, C.; Zhang, Z.; Yang, C. C. *J. Biomed. Opt.* **2016**, *21*, 1.

(22)   Dimitrijevic, N. M.; Rozhkova, E.; Rajh, T. *J. Am. Chem. Soc.* **2009**, *131*, 2893.

(23)   Kotagiri, N.; Sudlow, G. P.; Akers, W. J.; Achilefu, S. *Nat. Nanotechnol.* **2015**, *10*, 370.

(24)   Abdellah, M.; El-Zohry, A. M.; Antila, L. J.; Windle, C. D.; Reisner, E.; Hammarstrom, L. *J. Am. Chem. Soc.* **2017**, *139*, 1226.

(25)   Ashford, D. L.; Song, W.; Concepcion, J. J.; Glasson, C. R.; Brennaman, M. K.; Norris, M. R.; Fang, Z.; Templeton, J. L.; Meyer, T. J. *J. Am. Chem. Soc.* **2012**, *134*, 19189.

(26)   Asbury, J. B.; Hao, E.; Wang, Y.; Ghosh, H. N.; Lain, T. *J. Phys. Chem. B.* **2001**, *105*, 4545.

Chapter 3 : Detection and Selective Destruction of Lysosomes Using Chlorin e6 pH Dependent Lifetime Shifts and ROS Production

This chapter is based on a pending article:

Rebecca C. Gilson, Rui Tang, Daniel Foust, and Samuel Achilefu. Detection and Selective

Destruction of Lysosomes Using Chlorin e6 pH Dependent Lifetime Shifts and ROS Production.

ACS Sensors (To be submitted)

3.1 Chapter summary

Specific selection of therapeutic targets and detection of subsequent damage is vital to understand and optimize photodynamic therapy (PDT) of cancer. Here we present a PS, PS1, which can be used to monitor and disrupt lysosomal function by fluorescence lifetime imaging and light activated ROS production, respectively. As PS1 traffics from early endosomes to lysosomes, its lifetime decreases from 4.8 ± 0.2 to 4.5 ± 0.1 ns, corresponding to a pH change of 5.8 ± 0.5 to 4.9 ± 0.4. Furthermore, inhibition V-ATPases, preventing acidification of lysosomes, resulted in a pH increase to 5.3 as measured by PS1's lifetime. Time-dependent light activation of PS1 produced ROS, inducing lysosomal damage and pH neutralization. This study illustrates the potential use of PS1 to monitor the trafficking of PSs in cells and to spatiotemporally apply PDT to induce cell death. In addition, the fluorescence lifetime of PS1 provides a readout of intracellular pH and lifetime changes can predict cellular response to PDT.

3.2 Introduction

PDT is a treatment method that uses a light activatable drug (PS) to produce cytotoxic ROS. The outcome of the therapy depends on many factors, including the photophysical properties and subcellular location of the PS. Understanding the interplay between these variables is vital in developing an optimal therapy.

Endocytosis serves as the primary mechanism for PS internalization into cells. Throughout endocytosis, the PS encounters a decreasing pH gradient as it traffics through early endosomes (pH 6.5), late endosomes (pH 6.0), and lysosomes (pH 4.5-5).[1] Lysosomes are responsible for the degradation of macromolecules and contain over 50 different enzymes that are optimally active at pH 4.7.[2] In addition, lysosomes contain hydrolases such as cathepsin B/D/L which, when released from the lysosome, can activate caspase mediated apoptosis.[3-4] Release of the lysosome content

can occur through lysosomal membrane permeabilization (LMP). LMP can be formed through several methods: lysosomotropic drugs, microtubule-disrupting anti-cancer drugs, VepA activation which inhibits V-ATPase the proton pump responsible for acidifying lysosomes,[5] and intralysosomal ROS. ROS, such as hydroxyl radicals, can be formed endogenously through processes such as the Fenton reaction,[6-7] or through light activation of a PS localized to the lysosome.[8-9]

When PSs are activated in lysosomes, the ROS produced can trigger LMP, releasing lysosomal contents, and activating apoptosis. LMP will also result in neutralization of the lysosomal pH. Alternatively, activation of the PS in endosomes, before it reaches the lysosome, may result in less damage as endosomes do not contain apoptosis activating cathepsins. Therefore, a PS's subcellular localization can alter the effectiveness of PDT. It is important to determine the time it takes for the PS to traffic from endosomes to lysosomes, as this time indicates when the PS should be irradiated for PDT. This time is called the drug-light interval (DLI).

To detect differences in damage to endocytic vesicles post PDT, we developed a pH sensor to measure the vesicles' ability to maintain a physiological pH gradient. There are several fluorescence based methods for measuring pH in vivo: fluorescence intensity, ratiometric fluorescence, and fluorescence lifetime. Single wavelength fluorescence intensity measurements require the simplest instrumentation, data acquisition, and analysis; however, this method lacks the ability to adequately quantify absolute pH due to dependence on sensor concentration. Ratiometric probes provide a solution to this problem by using a dual channel sensor in which the pH is determined by calculating the ratio of the fluorescence intensities at each channel.[10] While this method may work well for sensors in solution, wavelength dependent scattering and absorption can cause unpredictable changes in the ratiometric measurements.[11-13] Therefore, we

developed a fluorescence lifetime imaging microscopy (FLIM) method tuned to specifically and non-invasively measure the pH of the endosomal pathway. Fluorescence lifetime is less dependent on the concentration of the fluorophore and can be used in both spectroscopy and in vivo measurements.

Here, we describe a novel PS, Ce6-cGRD (PS1) that internalizes through the endosomal pathway. Ce6 is a potent PS and has been developed into a clinical PS, talaporfin, to treat liver and pancreatic cancer.[14-15] PS1 has pH dependent fluorescence lifetime shifts with a pKa of 5.2, within the physiological pH of the endosomal pathway. We used PS1's fluorescence lifetime to measure pH of the endocytic pathway and monitor the integrity of lysosome structure before and after PDT. ROS induced damage to the lysosome, resulted in a pH increase indicative of LMP formation. Activation of PS1 in the lysosome resulted in ~80% more cell killing than activation in endosomes.

3.3 Experimental section

3.3.1 Chemicals and materials

All the fluorenylmethyloxycarbonyl (Fmoc) amino acids and Fmoc-Lys(Boc)-Wang Resin were purchased from AAPPTec (Louisville, KY, USA). All the other chemicals were purchased from Sigma-Aldrich (St. Louis, MO, USA) and used without further purification. Chlorin E6 (Ce6) was purchased from Frontier Scientific (Logan, UT, USA). Water was obtained from Millipore Direct Q3 system (Billerica, MA, USA). Mass-spectrometry was recorded on a Shimadzu LCMS2010 ESI mass Spectrometer (Columbia, MD, USA).

3.3.2 Synthesis of pH-sensitive fluorescent dye, PS1

The linear GRD peptide, H-DCys(Acm)-Gly-Arg(Pbf)-Asp(tBu)-Ser(tBu)-Pro-Cys(Acm)-Lys(Boc)-OH, was prepared via a CEM Liberty microwave peptide synthesizer

(Matthews, NC, USA) on the Fmoc-Lys(Boc)-wang resin (**Figure 15a**). The resin (0.1 mmol)

was swelled in DCM for 1 h before use. Fmoc-amino acids (0.5 mmol, 5 eq), coupling reagent

(HBTU, 0.5 mmol, 5 eq) and DIEA (1 mmol, 10 eq) were added to the resin and the mixture was

reacted for 15 min under MW irradiation (50W, 75 ℃). The resin was washed with DMF for 3

times. Deprotection of Fmoc group was carried out by treatment of 20% piperidine/DMF for 5

min under MW irradiation (50W, 75 ℃). The peptidyl resin was washed and collected.

Cyclization of the peptide to form the disulfide bridge was performed on resin with thallium

trifluoroacetate (1.2 eq) in DMF for 90 min. Subsequently, Ce6 (3 eq) is conjugated to the cyclic

peptide on solid support at the presence of HATU (5 eq) and DIEA (5 eq) in DMF to afford PS1

peptidyl resin. The resulted resin was then treated with a cleavage cocktail of TFA: thioanisol:

phenol: water (85:5:5:5, v/v/v/v) for 90 min at room temperature for 2 hours. The cleaved

peptide product was concentrated *in vacuo*, then purified on reverse-phase HPLC (Gilson,

Middleton, WI, USA). PS1 (Ce6-cyclic (DCys-Gly-Arg-Asp-Ser-Pro-Cys)-Lys-OH), M/W 1441,

ESI-MS observed 1442 (M+1) and 722 (M+2/2) (**Figure 15b**).

3.3.3 Spectral properties and pKa of PS1

The absorption and emission spectra of PS1 were recorded on a UV-vis absorption

spectrophotometer (Beckman DU640, CA, USA) and fluorimeter (Fluorolog-3, Horiba Jobin

Yvon, NJ, USA), respectively. The molar extinction coefficient of PS1 in water is measured to be

24,663 M^{-1} cm^{-1} at 400 nm. For pH titrations, PS1 was dissolved in 0.1M ionic strength NaCl in

water or Dulbecco's Modified Eagle Medium (DMEM) without phenol red. The initial solution

was acidified with dilute aqueous HCl. Incremental increase of the pH value was achieved by

adding small amount of dilute NaOH into the solution. The pH of the solutions were recorded with

a pH meter (Accumet AB15, MA, US). At each pH point, the absorption, fluorescence spectra,

and fluorescence lifetime (ex 640 nm/em 690/70 nm BP) (MicroTime200, PicoQuant, Berlin Germany) were also recorded.

3.3.4 Fluorescence lifetime spectroscopy and FLIM

Fluorescence lifetime of PS1 was measured on a MicroTime200 fluorescence lifetime microscope. Both imaging and spectroscopy was performed with a 40x0.65 objective, Plan N, Achromat, air spaced, working distance = 0.60 mm (Olympus, Center Valley, PA, USA). The time correlated single photon counting (TCSPC) histograms were obtained with a laser repetition rate of 10 MHz. A maximum laser output power of 6±0.6 µW was used.

A bi-exponential tail-fit was used to fit the TCSPCs in a FLIM image. A bi-exponential fit was chosen because (1) the pH titrations of Ce6 and PS1 showed two species, protonated and deprotonated, and (2) bi-exponentials achieved the chi-squared without over fitting (**Figure 8** and **Figure 16**). A tailfit was used to reduce variations between spectroscopy and imaging.

3.3.5 pH maps

pH calculated maps were created by using the standard curve obtained by the PS1 titration in DMEM to back-calculate the pH at each pixel in a FLIM image. At lifetimes higher than the upper saturation point of the standard curve (**Figure 9a**), the pH was assigned to the correspondingly highest pH that the curve predicted (4.724 ns, pH = 6.79), and therefore appear as dark red in the image. This was also done to the lowest pHs (3.595 ns, pH = 0.68), and therefore appear as dark blue in the image.

3.3.6 Bafilomycin A1 neutralization of the lysosomes and colocalization studies

4T1/luc cells were grown on glass bottom (#1) cell culture dishes (In Vitro Scientific, Sunnyvale, California, USA). For colocalization studies the cells were treated with 10 µM PS1 for 2 or 24 h and 75 nM lysotracker green (ThermoFisher Scientific, Waltham, MA, USA) for 2 h.

The cells were then washed with DMEM without phenol red and imaged with the FLIM system. For baflimoycin A1 cells studies, cells were incubated with PS1 for 24 hours, washed, and imaged on the FLIM to obtain baseline measurement. Cells were then treated with 200 nM bafilomycin A1 for 1 h and imaged.

Colocalization scatter plots were generated and Pearson's correlation coefficients were calculated using the ImageJ plugin, JACoP.

All cell imaging was done in a CO2 stage top incubator (In Vivo Scientific, St. Louis, MO, USA).

3.3.7 Photodynamic therapy with PS1

For FLIM PDT studies, 4T1/luc cells were grown on glass bottom (#1) cell culture dishes (In Vitro Scientific, Sunnyvale, California, USA). The cells were incubated with PS1 for 24 h, washed, and then irradiated with 650 nm light at 35 mW/cm^2 of light for 30 min. Pre and post PDT FLIM images were obtained.

For PDT viability studies, 4T1/luc cells were grown in 96-well black walled plates. The cells were incubated with PS1 for 1-24 h, washed, and then irradiated with 650 nm light at 3.65 mW/cm^2 of light for 10 min. 24 h after irradiation, a viability assay was performed using 3.33 μM of Calcein-AM in PBS for 30 min.

3.4 Results and discussion

3.4.1 Spectral properties of pH-sensitive PS, PS1

To use PS1 as a pH sensor, we first characterized the pH sensitivity of its absorption and fluorescence emission. pH titrations of PS1 and Ce6 showed that each absorption peak of PS1 and Ce6 are spectrally pH dependent (**Figure 8b** and **Figure 16a**). The 400 nm and 500 nm peak blue shift with increasing pH, while the 640 nm peak red shifts to 660 nm. Similar shifts were observed

in the fluorescence emission of PS1 and Ce6 (**Figure 8c** and **Figure 16b**). When excited at 400

nm or 620 nm, the emission peak red shifts from 640 to 660 nm. These data indicate two species

of Ce6 exist, protonated and deprotonated. The ratio of these two species is determined by the pH

of solution with a pKa of 5.2 (**Figure 16** and **Figure 17**)
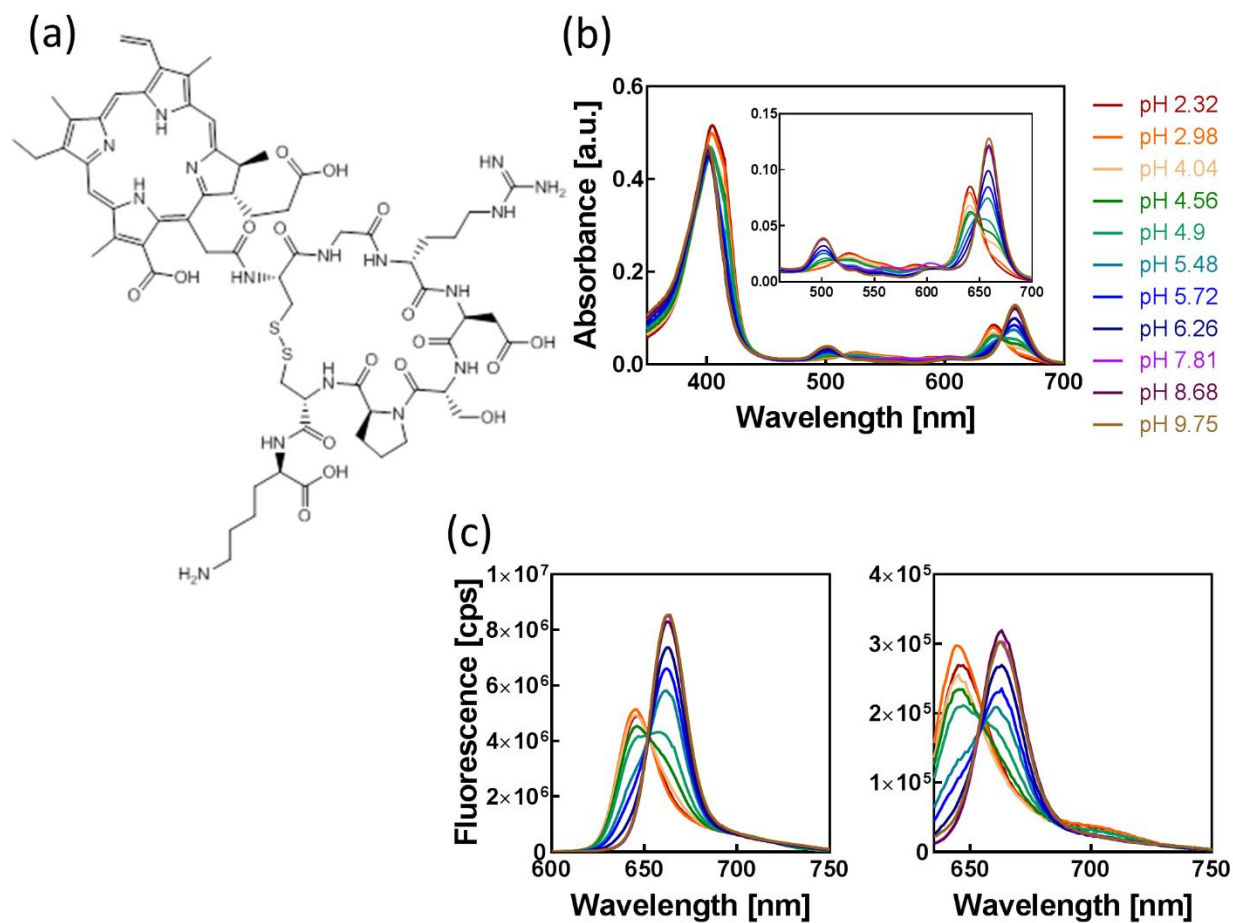
Figure 8. (a) Structure of PS1. (b) Absorption spectra of pH titrated PS1 in NaCl water. (c)

Emission spectra of pH titrated PS1 excited at 400 nm or 620 nm. The legend for b and c are the

same.

3.4.2 pH sensitive fluorescence lifetime properties of PS1

To explore a more robust method to measure pH, compared to the ratiometric pH method,

the fluorescence lifetime of PS1 was measured as a function of pH. The titrations were conducted

in DMEM media without phenol red to mimic the intracellular environment and in saline (**Figure 9a** and **Figure 18**), respectively. The lifetime histograms clearly show two lifetime components (**Figure 9a**). The relative amplitudes of the two lifetimes change as a function of pH while the actual lifetimes remain constant. Lifetime histograms were fit with bi-exponentials tail-fits and the average lifetime at each pH was calculated using the extracted values. We then constructed a standard curve of average lifetime versus measured pH to obtain a sigmoidal curve with a pKa of 5.2 ± 0.1 (**Figure 9b**). This standard curve was used to back calculate the pH based on the measured lifetime (**Figure 9c**). The linear fit of the calculated pH versus the measured pH had a slope of 0.98 ± 0.03 and could be used to predicted pHs from 2.33 to 5.5 with residuals less than the absolute value of 0.3. The pKa of PS1 makes it a suitable candidate for sensing the acidic pH of the lysosomes and the endosomal pathway.
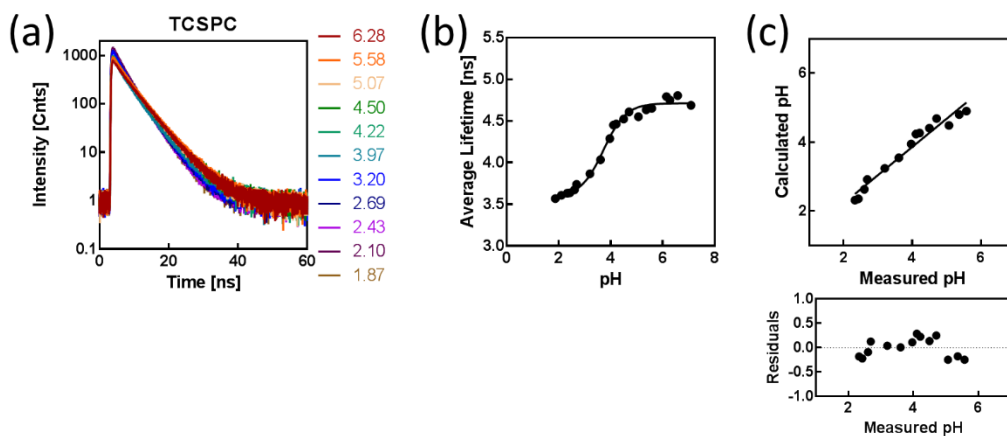
Figure 9. (a) Lifetime histograms of PS1 titrated phenol red free DMEM. (b) Average lifetime of PS1 as a function of pH calculated by fitting the lifetime histograms to a bi-exponential tail-fit, pKa 5.2. (c) Calculated pH corresponds to the measured pH with minimal residuals. n=3 titrations.

3.4.3 PS1 internalizes into the lysosomes

To determine the subcellular localization of PS1, it was incubated with cells for 2 h or 24 h and lysotracker green was added 2 h before imaging. As seen by the yellow overlap of the two dyes PS1 localizes to the lysosomes (**Figure 10a**).[16] In addition, scatter plots of the two channels of each image show a positive correlation between PS1 and lysotracker green (**Figure 10b**). A Pearson correlation coefficient of 0.6, between the two channels, quantitatively confirm colocalization (**Figure 10b,c**).
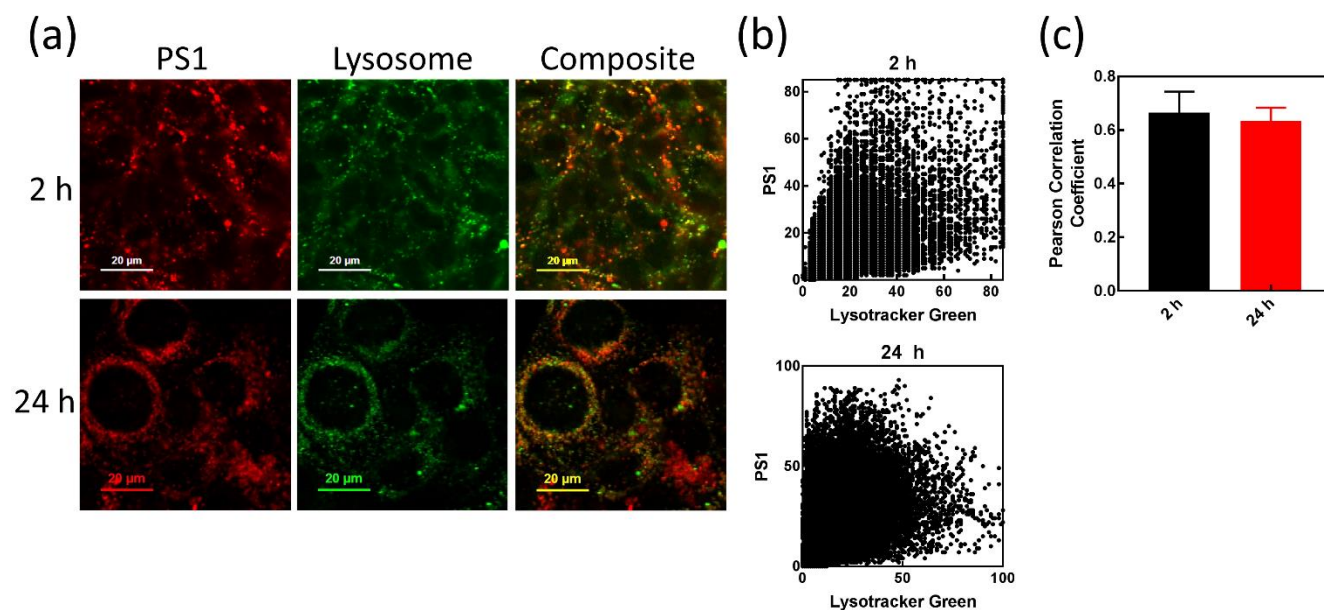
Figure 10. (a) Colocalization between PS1 and lysotracker green at 2 and 24 h. (b) Scatter plots between the red channel and green channel for the two images shown in (a). (c) Pearson correlation coefficient calculated between the red channel and green channel across 5 images.

3.4.4 Fluorescence lifetime of PS1 is an indicator of endosomal pH

Next, we used the fluorescence lifetime of PS1 to measure the pH of the endosomal pathway. Cells were incubated with PS1 for 2 to 24 h followed by FLIM. The fluorescence lifetime images were fit with bi-exponential tail-fits and the average lifetime at each pixel was calculated. From 2 to 24 h the lifetime of PS1 dropped from 4.8 ± 0.2 ns to 4.5 ± 0.1 ns, indicating a decrease

in pH (**Figure 11a** and **Figure 19**). The fluorescence lifetime image was converted into a pH map, such that at each pixel of the image the average lifetime of PS1 was used to calculate the pH of the local environment using the standard curve previously obtained (**Figure 11b** and **Figure 9b**). Quantification of the pH maps indicate that PS1 experiences different pHs: At 2 h the pH is 5.8 ± 0.5, corresponding to the pH of endosomes, while at 24 h the pH is 4.9 ± 0.4, corresponding to the pH of lysosomes (**Figure 11b,d**). This indicates that from 2 h to 24 h PS1 is trafficked through increasingly acidic vesicles of the endosomal pathway and at 24 h resides in the acidic lysosomes. Thus, the lifetime of PS1 is responsive to environmental pH changes and can be used to measure the local pH.
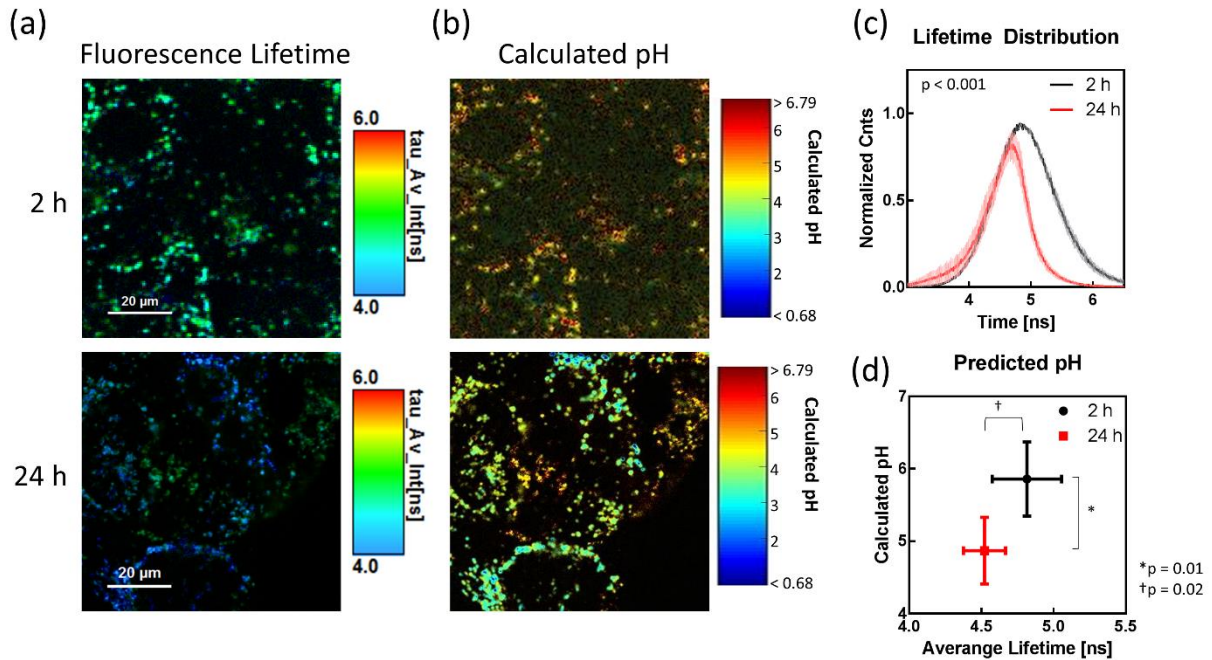
Figure 11. (a) FLIM of PS1 incubated in cells for 2 or 24 h. (b) pH maps of the corresponding fluorescence lifetime images. (c) Normalized lifetime distribution histograms of PS1. (d) Average lifetime of PS1 plotted versus the calculated pH, showing the average pH at 2 h is 5.8 ± 0.5, and at 24 h is 4.9 ± 0.4. n≥3.

3.4.5 PS1 lifetime is responsive to acute changes in lysosomal pH

Next, we characterized the responsiveness of PS1 to lysosome damage in the form of

intra-lysosomal pH change. We chose bafilomycin A1 as a model for lysosome damage.

Bafilomycin A1 inhibits VTP-ases, which are responsible for pumping protons into the

lysosomes to maintain an acidic pH.[17] At both 2 and 24 h of PS1 incubation, bafilomycin A1 was

added to the cells and fluorescence lifetime images were obtained before and after treatment

(**Figure 12a**). The final pH of the vesicles after additional of bafilomycin A1 was ~5.3,

regardless of the starting pH of the endosome or lysosome (**Figure 12b**). Therefore, PS1's

fluorescence lifetime responds to acute changes in pH that indicate lysosomal integrity.
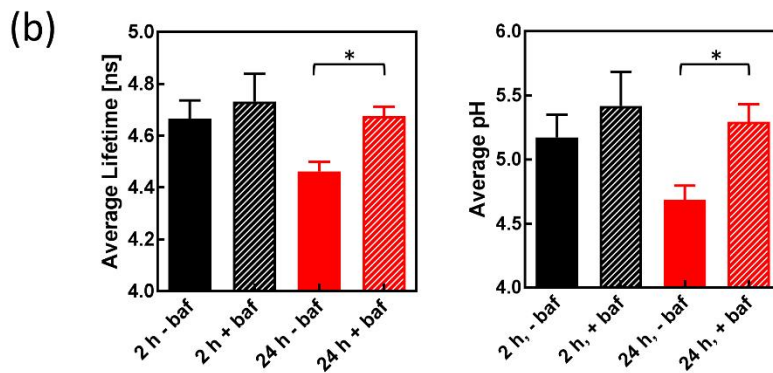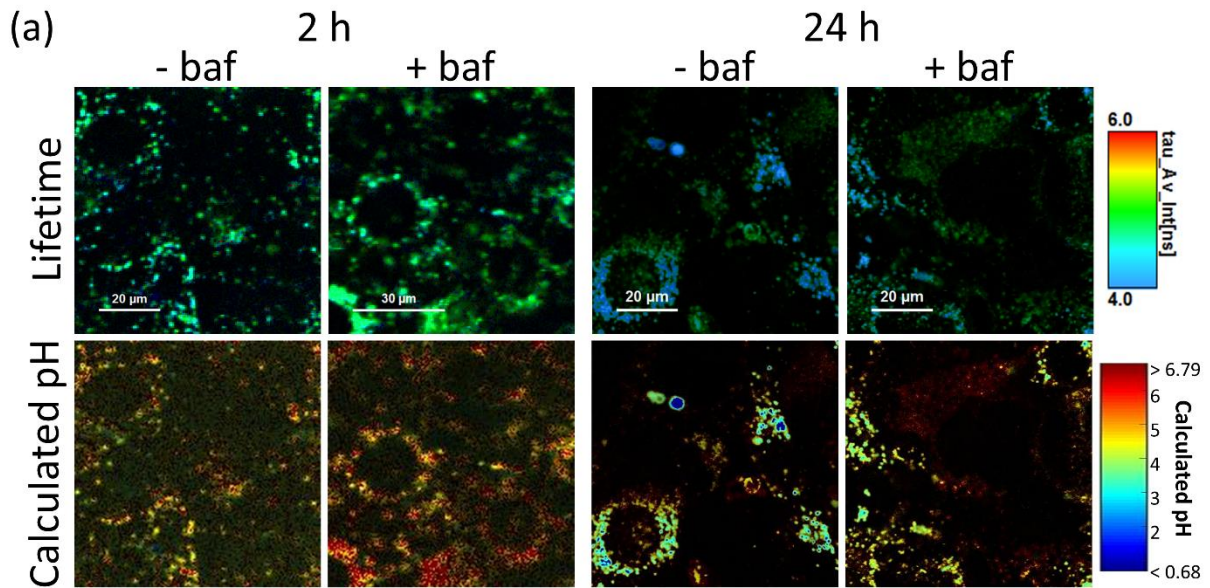
Figure 12. (a) FLIM and pH maps of PS1 at 2 or 24 hours, before and after addition of bafilomycin A1. (b) The average lifetime and pH change before and after the addition of bafilomycin A1 at both timepoints. (*p < 0.05.) n≥3.

3.4.6 Bafilomycin A1 changes the subcellular localization of PS1

PS1 can measure the physiological pH change due to bafilomycin A1. We next sought to determine if bafilomycin A1 induced structural changes to the lysosome that could be asses by the subcellular localization of PS1. We therefore performed colocalization imaging of PS1 and lysotracker green after the addition of bafilomycin A1 and found that, indeed, PS1 and lysotracker green no longer colocalize (**Figure 13a**). This was further quantified in scatter plots and by the

Pearson correlation coefficient (**Figure 13b,c**). Therefore, PS1 is a sensor that can be used to measure the physiological and structural changes to lysosomes after a damaging event.
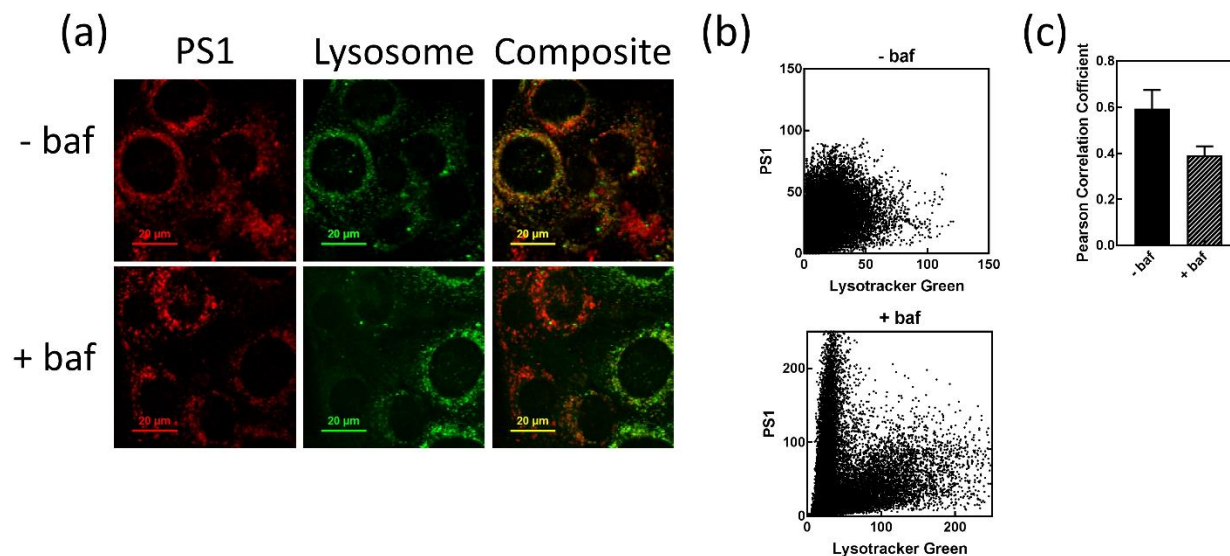
Figure 13. (a) Bafilomycin A1 was added to cells at 24 h post incubation with PS1 and 2 h post incubation of lysotracker green. (b) Scatter plots and (c) Pearson correlation coefficient of red and green channels before and after bafilomycin A1. n=3.

3.4.7 PDT activation of PS1 causes loss in lysosomal integrity

After characterization of PS1's ability to quantify damage using the model system of bafilomycin A1, we tested whether PS1 could be used a dual sensor and lysosome damaging PDT agent. PS1 contains the PS Ce6, which produces ROS and free radicals when activated with red light. We use FLIM to characterize the nature of the cellular damage inflicted by light activation of PS1. The pre- and post- PDT images clearly show an increase in lifetime of PS1, corresponding to an increase in pH to ~6 (**Figure 14a,b**). Moreover, the distribution of PS1 changed from punctate to diffuse, indicating that the ROS inflicted damage to the lysosomes causing the release of PS1 into the cytosol. These physiological and structural changes are similar to the ones that occurred with bafilomycin.

The damage to the lysosome was so significant that it resulted in cell death. (**Figure 14c**). When PS1 localized to the early endosomes, a DLI of 1 and 2 h, the therapy was minimally effective. When PS1 localized to late endosomes, a DLI of 4 the therapy resulted in a 60% loss in viability with minimal dark toxicity. However, the therapy resulted in the greatest loss in viability, when PS1 localized to the lysosomes, a DLI of 24 h, resulting in 97% of cell killing compared to the untreated control. We did observe significant dark toxicity at 24 hours due to just PS1. Lysosome PDT was likely the most effect at inducing cell death due to the release of apoptosis activating cathepsins from the lysosome.
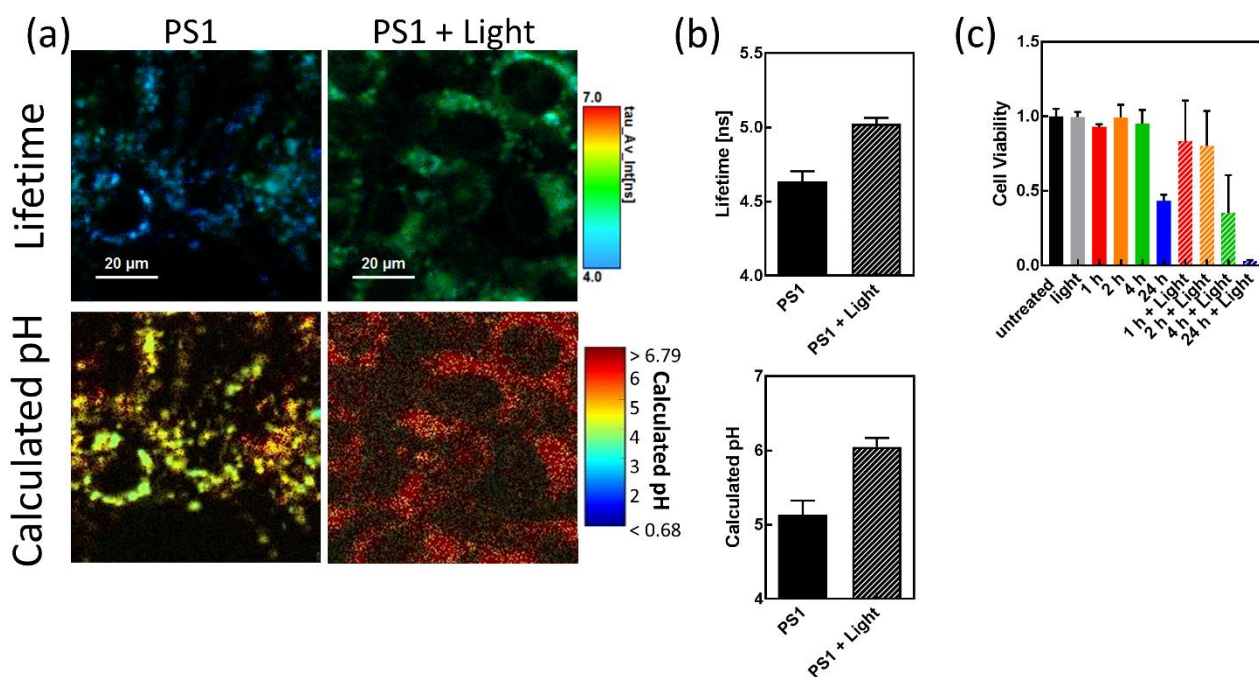
Figure 14. PDT results in loss of lysosome integrity. (a) PS1 was incubated in cells for 24 h. FLIM images were taken of cells before and after PDT. (b) Lifetime and calculated pH change before and after PDT. (c) Cell viability after PDT with a DLI of 1-24 h.

3.5 Conclusion

In summary, we have constructed a pH-sensitive sensor and photosensitizer by conjugation of chlorin e6 to a peptide that undergoes internalization through the endosomal pathway. PS1 has

pH sensitive fluorescence lifetime shifts that enables quantitative and real-time pH measurements of the endosomal pathway. Irradiation of PS1 stimulates ROS production that selectively destroys lysosomes resulting in cell death. Subsequent lifetime measurements of PS1 confirm lysosomal destruction due to increase in pH and loss of ability to maintain a physiological pH gradient. In this study, we showed that PS1 is a dual sensor and PS that enables real-time readout of damage inflicted by PDT.

3.6 Supporting information

(a)

(b)
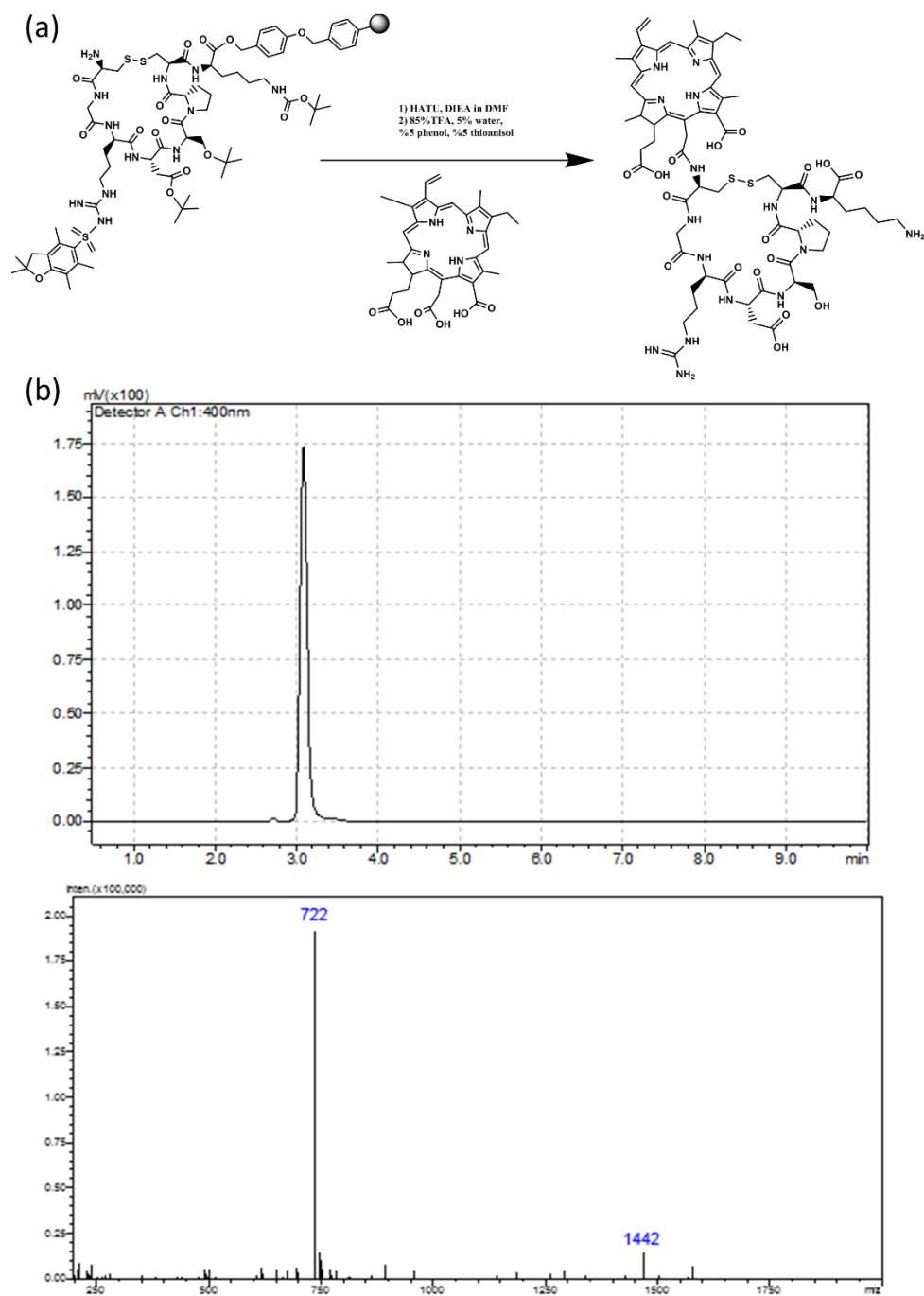
Figure 15. (a) Synthesis scheme of PS1. (b) LCMS spectrum of PS1.
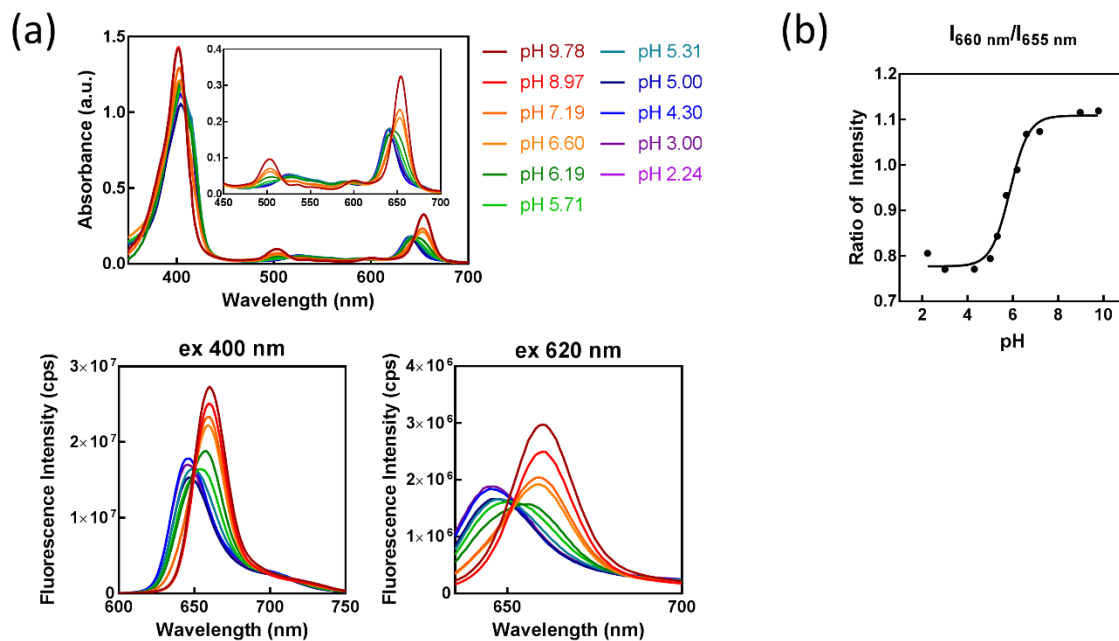
Figure 16. (a) Absorption and emission spectra of pH titrated Ce6 in saline from pH 2.24 to 9.75. All three absorption peaks change according to pH. Emission spectra excited at 400 nm or 620 nm. Both excitation wavelengths result in a red shift of emission as pH increased. (b) Ratiometric pH curve of peak fluorescence at 660 nm and the isosbestic point at 650 nm, pKa 5.87.
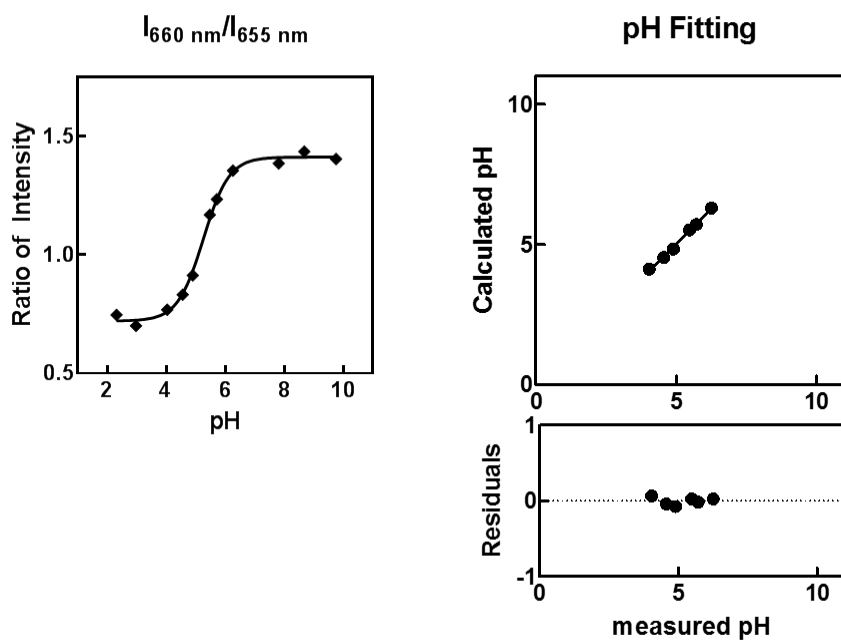
Figure 17. Ratiometric approach for quantifying the pH changes of PS1. The peak emission fluorescence at 660 nm divided by 655 nm, the fluorescence at the isosbestic point. The curve was fit with a sigmoidal equation, pKa 5.2. The sigmoidal curve was used to back-calculate the pH and this was plotted versus the measured pH.
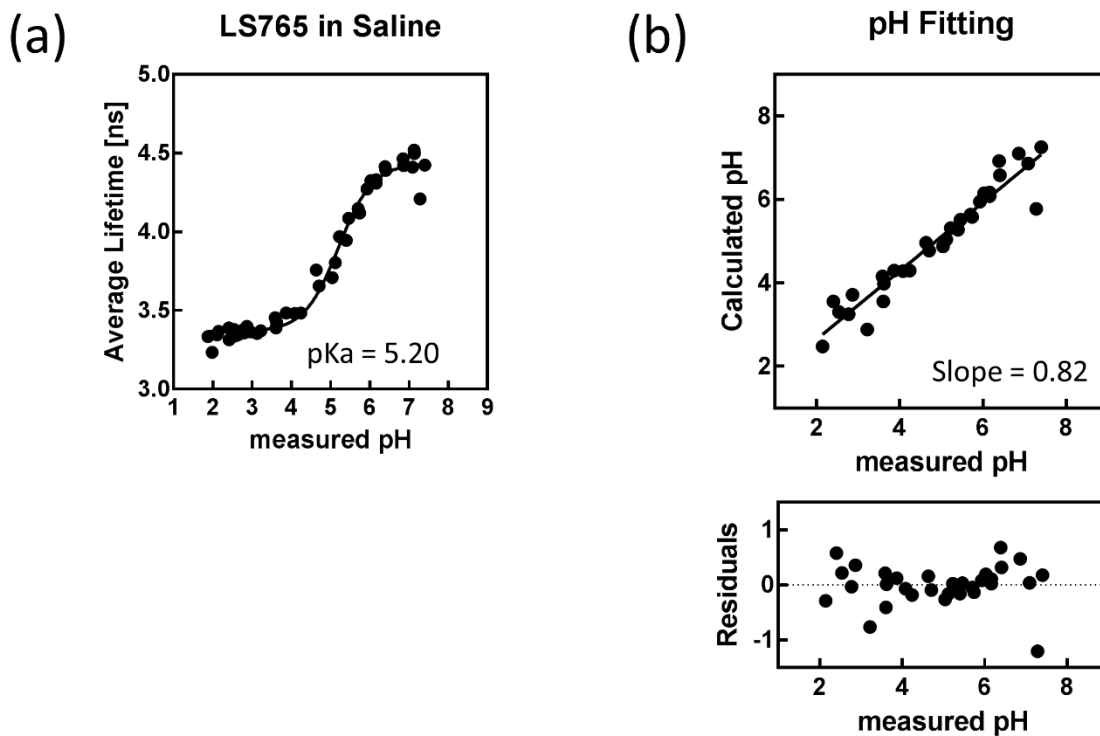
Figure 18. Lifetime titration of PS1 in saline. (a) The lifetime distribution was fit with a sigmoidal equation. (b) The sigmoidal curve was used to back-calculate the pH and this was plotted versus the measured pH. n≥3
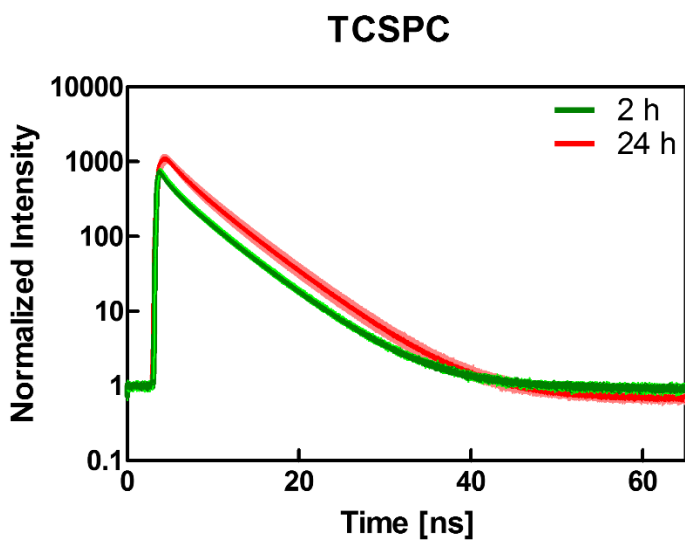
Figure 19. TCSPCs for PS1 incubated in cells for 2 or 24 h. n≥3

3.7 Acknowledgments

3.8 References

(1)   Casey, J. R.; Grinstein, S.; Orlowski, J. *Nat. Rev. Mol. Cell. Biol.* **2010**, *11*, 50.

(2)   Luzio, J. P.; Pryor, P. R.; Bright, N. A. *Nat. Rev. Mol. Cell Biol.* **2007**, *8*, 622.

(3)   Boya, P.; Kroemer, G. *Oncogene* **2008**, *27*, 6434.

(4)   Aits, S.; Jaattela, M. *J. Cell Sci.* **2013**, *126*, 1905.

(5)   Matsuda, S.; Okada, N.; Kodama, T.; Honda, T.; Iida, T. *PLOS Pathog.* **2012**, *8*, e1002803.

(6)   Baird, S. K.; Kurz, T.; Brunk, U. T. *Biochem. J.* **2006**, *394*, 275.

(7)   Schafer, F. Q.; Beuttner, G. R. *Free Radicals Biol. Med.* **2000**, *28*, 1175.

(8)   Tsai, S. R.; Yin, R.; Huang, Y. Y.; Sheu, B. C.; Lee, S. C.; Hamblin, M. R. *Photodiagn. Photodyn. Ther.* **2015**, *12*, 123.

(9)   Aggarwal, N.; Santiago, A. M.; Kessel, D.; Sloane, B. F. *Breast Cancer Res. Treat.* **2015**, *154*, 251.

(10)   Han, K.; Wang, S. B.; Lei, Q.; Zhu, J. Y.; Zhang, X. Z. *ACS Nano* **2015**, *9*, 10268.

(11)   Orte, A.; Alvarez-Pez, J. M.; Ruedas-Rama, M. J. *ACS Nano* **2013**, *7*, 6387.

(12)   Sarder, P.; Maji, D.; Achilefu, S. *Bioconjug. Chem.* **2015**, *26*, 963.

(13)   Izquierdo, M. A.; Aurimas, V.; Lermontova, S. A.; Grigoryev, S.; Shilyagina, N. Y.; Balalaeva, I. V.; Klapshina, L. G.; Kuimova, M. K. *J. Mater. Chem. B.* **2015**, *8*, 1089.

(14)   Nakajima, T.; Sano, K.; Mitsunaga, M.; Choyke, P. L.; Kobayashi, H. *Cancer Res.* **2012**, *72*, 4622.

(15)   Cunderlikova, B.; Gangeskar, L.; Moan, J. *J. Photochem. Photobiol., B* **1999**, *53*, 81.

(16)   Achilefu, S.; Bloch, S.; Markiewicz, M. A.; Zhong, T.; Ye, Y.; Dorshow, R. B.; Chance, B.; Liang, K. *Proc. Natl. Acad. Sci. U. S. A.* **2005**, *102*, 7976.

(17)   Yamamoto, A.; Tagawa, Y.; Yoshimori, T.; Moriyama, Y.; Masaki, R.; Tashiro, Y. *Cell Struct. Funct.* **1998**, *23*, 33.

Chapter 4 : ROS Localized to the ER Results in Greater Cell Death Compared to Lysosomes and Mitochondria

This chapter is based on a pending article:

Rebecca C. Gilson, Rui Tang, and Samuel Achilefu. ROS Localized to the ER Results in Greater Cell Death Compared to Lysosomes and Mitochondria. *Bioconjugate Chemistry (To be submitted)*

4.1 Chapter summary

Photodynamic therapy is a versatile strategy that can treat many forms of cancer including those with resistant phenotypes. However, it remains unclear which subcellular organelle is most susceptible to oxidative damage and therefore where the photosensitizer should be targeted. To elucidate the optimal intracellular target, we conjugated the photosensitizer, Ce6, to ligands that directed it to different organelles: ER (Ce6), lysosome (PS1 and PS2) and dual mitochondria and lysosome (PS3). Conjugation of Ce6 led to alterations in the kinetics of hydroxyl radical and hydrogen peroxide production. At 10 min of irradiation, Ce6 produced significantly more hydroxyl radicals than the conjugates, and PS2 and PS3 produced more hydrogen peroxide that Ce6 or PS1. After normalization of the intracellular concentration of each PS, the therapeutic efficacy of organelle based PDT was assessed. Lysosomal PDT was greatly affected by the PS conjugate used: PS1 resulted in no cell death, while PS2 resulted in 75% cell death. Dual mitochondrial and lysosomal PDT killed 63% of cells. ER PDT resulted in the greatest cell death, killing up to 92% of cells with negligible dark toxicity. In conclusion, we found that ROS production in the ER resulted in the greatest cell killing, compared to the lysosome and the mitochondria.

4.2 Introduction

PDT is a form of cancer treatment that combines light and light activatable drugs, photosensitizers (PSs), to produce cytotoxic reactive oxygen species (ROS). PDT can act through multiple pathways to cause tumor regression: direct damage to tumor cells resulting in necrosis and apoptosis, shut down of microvessels depleting the tumor of nutrients and oxygen, and activation of the acute and innate immune system resulting in inflammation.[1]

The intracellular localization of the PS affects the type of damage that is done to the cell

and therefore the therapeutic outcome. The lysosome is an easily accessible target, as many PSs internalize through the endosomal pathway. Activation of the PS in the lysosome, produces ROS that oxidize lipids causing lysosomal membrane permeabilization (LMP), release of cathepsins into the cytosol, and activation of apoptosis.[2-6] In a similar chain of events, activation of a PS in the mitochondria can permeabilize the mitochondrial membrane, releasing cytochrome c, and activating apoptosis.[7-8] Activation of the PS in the endoplasmic reticulum (ER) can cause the release of large stores of calcium, which again can activate apoptosis.[9]

Despite the development and testing of many PSs, it remains unknown how susceptible each organelle is to ROS. A direct comparison, using the same PS, of lysosomal PDT with mitochondrial PDT found that mitochondrial PDT killed ~20-fold greater HeLa cells than lysosomal PDT, suggesting that mitochondrial PDT was more effective.[10] In a different study, sequential lysosomal and mitochondrial PDT, with NPe6 and benzoporphyrin derivative (BPD), respectively, proved to be more effective than PDT in either organelle separately.[4-5, 11] We therefore hypothesized that a PS targeting both the lysosome and mitochondria would also be more effective than PDT in a single organelle. Few studies have been conducted to directly compare ER PDT with lysosomal or mitochondrial PDT. ER PDT has been linked to activation of anti-tumor immunity a potentially unique tumor regression pathway compared to PDT in other organelles.[12-15]

Difficulty in direct organelle comparisons arise from inability to control for all variables, such as, the local environment of the organelle or the photophysical properties of the PSs. Many previous studies attempt to compare organelle specific PDT with different targeted PSs, failing to isolate the organelle as the single altered variable. To eliminate the PS as an additional variable, we used a single PS, chlorin e6 (Ce6), for all targeted organelles. Ce6 has a high molar extinction

coefficient at 660 nm and low photodecomposition.[16] In addition, a derivative of Ce6, mono-L-aspartyl chlorin e6 (NPe6), has been tested in clinical phase 3 trials to treat hepatocellular carcinoma and colorectal cancer metastatic to the liver.[17]

We tested Ce6 activation in three subcellular localizations, including the: endoplasmic reticulum (ER) with Ce6, lysosomes with PS1 and PS2, and both lysosome and mitochondria with PS3. After correcting for the intracellular PS concentration, we found that for lysosomal PDT was highly dependent on the targeting ligand: PS2 killed ~75-fold more cells than PS1. In addition, we found that lysosomal PDT (PS2) was comparable to dual lysosomal and mitochondrial PDT (PS3). Finally, we found that ER PDT resulted in the greatest loss in viability while maintaining the lowest dark toxicity.

4.3 Experimental section

4.3.1 Chemicals and materials

Dulbecco's modified Eagle's medium (DMEM) culture medium, fetal calf serum, and penicillin-streptomycin were purchased from Gibco, (Life Technologies, NY, USA). Lysotracker green, mitotracker green, ER tracker green, HPF, Amplex Red assay, Calcein AM were purchased from Thermo Fisher Scientific.

4T1/luc murine breast cancer cells were obtained from David Piwnica-Worms, Washington University in St. Louis.[16] Cells were cultured using DMEM supplemented with 10% FBS, and 1% penicillin streptomycin in a humidified incubator at 5% CO2 balanced with air at 37°C. The cells were kept at 50–80% confluence.

4.3.2 Synthesis of PS1

The linear GRD peptide, H-DCys(Acm)-Gly-Arg(Pbf)-Asp(tBu)-Ser(tBu)-Pro-Cys(Acm)-Lys(Boc)-OH, was prepared via a CEM Liberty microwave peptide synthesizer

(Matthews) on the Fmoc-Lys(Boc)-wang resin (**Figure 15**). The resin (0.1 mmol) was swelled in DCM for 1 h before use. Fmoc-amino acids (0.5 mmol, 5 eq), coupling reagent (HBTU, 0.5 mmol, 5 eq) and DIEA (1 mmol, 10 eq) were added to the resin and the mixture was reacted for 15 min under MW irradiation (50W, 75 ºC). The resin was washed with DMF for 3 times. Deprotection of Fmoc group was carried out by treatment of 20% piperidine/DMF for 5 min under MW irradiation (50W, 75 ºC). The peptidyl resin was washed and collected. Cyclization of the peptide to form the disulfide bridge was performed on resin with thallium trifluoroacetate (1.2 eq) in DMF for 90 min. Subsequently, Ce6 (3 eq) is conjugated to the cyclic peptide on solid support at the presence of HATU (5 eq) and DIEA (5 eq) in DMF to afford PS1 peptidyl resin. The resulted resin was then treated with a cleavage cocktail of TFA: thioanisol: phenol: water (85:5:5:5, v/v/v/v) for 90 min at room temperature for 2 hours. The cleaved peptide product was concentrated *in vacuo*, then purified on reverse-phase HPLC (Gilson). PS1 (Ce6-cyclic (DCys-Gly-Arg-Asp-Ser-Pro-Cys)-Lys-OH), M/W 1441, ESI-MS observed 1442 (M+1) and 722 (M+2/2) (**Figure 15b**).

4.3.3 Synthesis of PS2

Synthesis scheme is illustrated in **Figure 25**. Briefly, 86 mg of TPP ((3-caboxypropl)triphenylphosphonium bromide) was dissolved in 1 mL of anhydrous DMF and then 65 mg of CDI (1,1-Carbonyldiimidazole) and 38 μL of N-Boc-ethylenediamine was added following vortexing for 6 h. The product was precipitated with diethyl ether, dried and treated with 95% TFA to remove the boc-protection. The resulted TPP-amine was dried and dissolved in 1 mL of anhydrous DMF, then added 60 mg Ce6 (chlorin e6), 12 mg of DMAP (4-Dimethylaminopyridine) and 76 mg of HATU (1-[Bis(dimethylamino)methylene]-1H-1,2,3-triazolo[4,5-b]pyridinium 3-oxid hexafluorophosphate), subsequently. The reaction mixture was

vortexed for overnight at room temperature. The final product was precipitated with diethyl ether and purified on reverse-phase HPLC (Gilson). PS2, M/W 970. ESI-MS: observed 917(M+1) and 486 (M+2/2).

4.3.4 Synthesis of PS3

Synthesis scheme was illustrated in below **Figure 26**. Briefly, 86 mg of TPP ((3-caboxypropl)triphenylphosphonium bromide) was dissolved in 1 mL of anhydrous DMF and then 65 mg of CDI (1,1-Carbonyldiimidazole) and 87 µL of 2,2-(Ethylenedioxy)bis(ethylamine) was added following vortexing for 6 h. The product was precipitated with diethyl ether. The resulted product was then dried and dissolved in anhydrous 1 mL of DMF, then added 30 mg Ce6 (chlorin e6), 6 mg of DMAP (4-Dimethylaminopyridine) and 36 mg of HATU (1-[Bis(dimethylamino)methylene]-1H-1,2,3-triazolo[4,5-b]pyridinium 3-oxid hexafluorophosphate), subsequently. The reaction mixture is vortexed for overnight at room temperature. The final product was precipitated with diethyl ether and purified on reverse-phase HPLC (Gilson). PS3, M/W 1519. ESI-MS: observed 760 (M+2/2) and 507 (M+3/3).

4.3.5 Colocalization imaging

Colocalization studies were completed on a MicroTime200 (MT200) fluorescence lifetime microscope (PicoQuant) or confocal FV1000 (Olympus). MT200 imaging was completed with a 100x objective. Filters for the PS red channels where ex/em 640/655-725 nm and organelle stain green channel were ex/em 488/510-530 nm. Confocal imaging was completed with a 60x objective. Filters for the PS red channels where ex/em 633/650/750 nm and organelle stain green channel were ex/em 488/510-530 nm.

All PS were incubated with cells for 4 h at 5 µM. Organelle stains were added before PS staining was completed such that at 4 h the cultures were washed and ready for imaging. For

lysosome staining, lysotracker green was incubated in cells for 2 h at 75 nM. For mitochondria

staining, mitotracker green was incubated in cells for 15 min at 50 nM. For ER staining, ER-

tracker green was incubated in cells for 15 min at 1 μM. Imaging was conducted in DMEM

without phenol red.

Line plots were generated by selecting a line of interest, shown on the image, and

generating a profile plot via Image J. The intensities were normalized to the max value of each

line.

Pearson correlation coefficients were calculated using the Image J (NIH, USA) plug-in JACoP,

with at least 3 representative images.[17]

4.3.6 ROS measurements

For both hydroxyl radical and hydrogen peroxide assays, 10 μM of 50 μl PS was

irradiated with 650 nm, 0.84 mW/cm^2. For hydroxyl radical assays, 10 μM of hydroxyphenyl

fluorescein, HPF, was added to the PS. This solution was irradiated on a 96 well plate, in

triplicate for 0-60 min. The fluorescence of each sample was read on a plate reader (BioTek,

USA), ex/em 485/518-538 nm.

For hydrogen peroxide measurements, after irradiation was complete, the Amplex Red

assay was used to quantify hydrogen peroxide concentration. A plate reader was used to read the

fluorescence at ex/em 545/580-600 nm. A reference standard of known hydrogen peroxide

concentration were used to calculate the concentration of hydrogen peroxide produced.

4.3.7 PDT and intracellular PS concentration

4T1 cells were seeded in a 96-well plate at a density of 5,000 cells (100 μl) per well 24 h

prior to PDT experiments. Cells were treated with 0-100 μM Ce6, PS1, PS2 or PS3 for 4 h. Cells

were then washed, their media replaced with phenol free DMEM, and their fluorescence was read

on a plate read (BioTek, USA) ex/em 390/645 nm in order to quantify the amount of PS that had internalized into the cells. Cells were irradiated with 650 nm light for 10 min at either 0.84 mW/cm^2 or 3.25 mW/cm^2. The cells were then cultured for 24 h, at the end of which a viability assay was conducted. Morphology of the cells were monitored with a bright field microscope.

To normalize the intracellular concentration of each PS, cells were treated with different starting concentrations of PS: 6.35 µM (Ce6), 4.68 µM (PS1), 10 µM (PS2), 3.11 µM (PS3) (**Figure 29**, **Figure 24a**). PDT assays were conducted as indicated above.

4.3.8 Cell viability

Cells were washed with PBS 3x prior to viability assay. Cells were incubated with 3.33 µM (100 µl, PBS) per well of Calcein Am for 30 min. Calcein AM fluorescence was read on a plate reader ex/em 485/518-538 nm. Fluorescence was normalized to the untreated control.
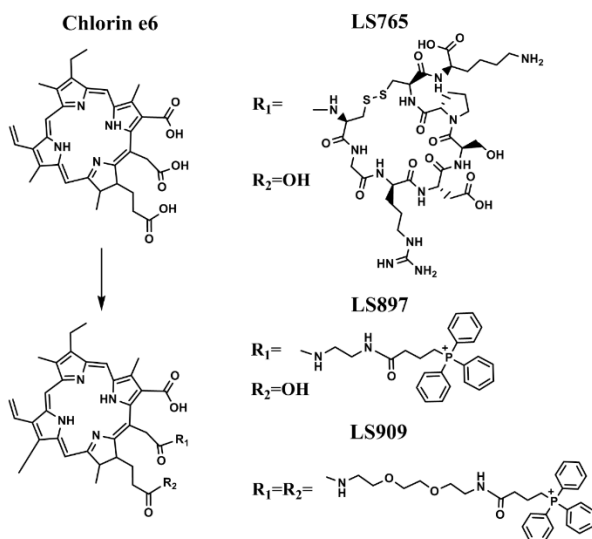
Figure 20. Structures of each four Ce6 based PS.

4.4 Results and discussion

4.4.1 Organelle specific uptake of Ce6 targeted derivatives

All four PSs internalized into 4T1, murine breast cancer cells, by initial plasma membrane binding and subsequent internalization (**Figure 28**).[20-21] After 4 h of incubation with

cells, all PSs have reached their respective organelle of interest as shown by line plots and high

Pearson correlation coefficients between the red (PS) channel and green (organelle marker)

channel (**Figure 21**).

Ce6 traffics with its membrane bound component to the ER.[22] PS1 internalized through the

endosomal pathway and at 4 h resides in the lysosome. PS2, although targeted using TPP which

typically delivers cargo to the mitochondria, again resulted in lysosome accumulation.[10, 23] This

may be due to the hydrophobicity of Ce6. To overcome this, we added a PEG spacer and an

additional TPP to Ce6 to obtain, PS3. At 4 h, PS3 resides in both lysosomes and mitochondria as

indicated by colocalization with both lysotracker and mitotracker with Pearson correlation

coefficients of 0.5 ±0 .3 and 0.6 ±0 .1, respectively (**Figure 21c**). Mitochondrial uptake of PS3

could likely be increased through addition of methyl groups to the TPP phenyl rings.[23]
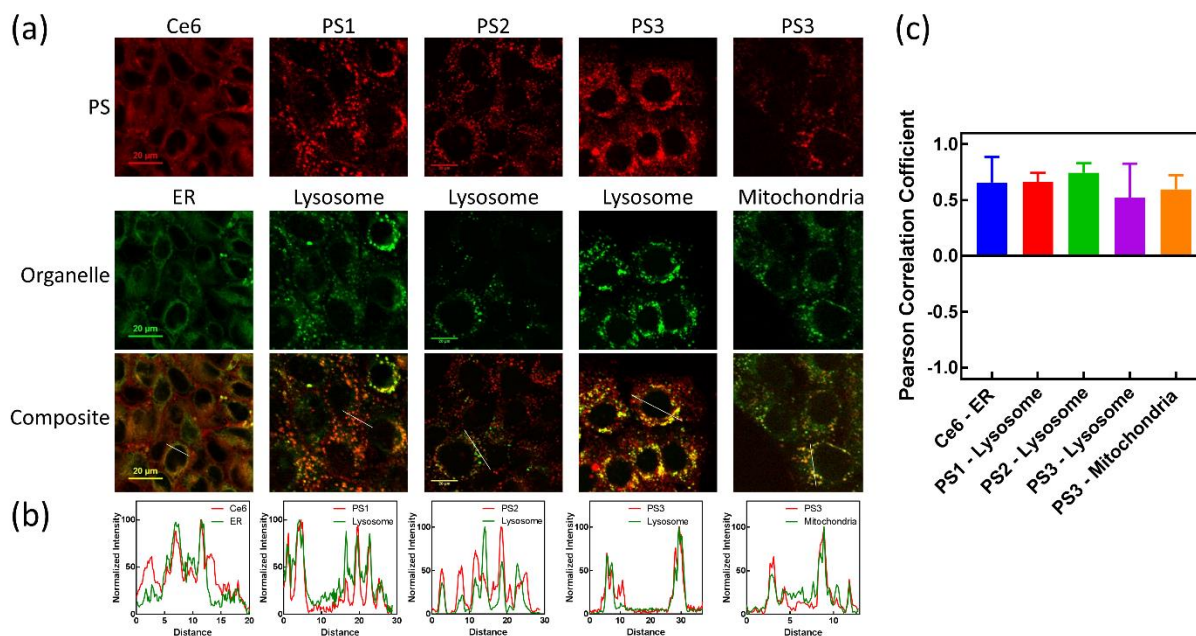
Figure 21. (a) Subcellular localization experiments where each PS (red) was co-incubated with

an organelle stains (green). Composite images show colocalization (yellow) between the two

59

dyes. (b) Normalized intensity of each dye along a line of interest (shown in white). (c) Pearson correlation coefficient between the red and green channel for each PS and organelle staining. $n \geq 3$ images.

4.4.2 Targeting ligand alters ROS production

To ensure all PS retained ROS production after addition of targeting ligands, we measured hydrogen peroxide and hydroxyl radical production upon light activation of the PSs. We used the molar extinction coefficients of Ce6 to calculate concentration of all PSs in order correlate the ROS generation between the PSs. The distinction between hydrogen peroxide and hydroxyl radical production is important when determining the location and type of oxidative damage. Hydrogen peroxide can diffuse through membranes and therefore can inflicted damage at locations distant from where it was produced. At these distant locations, it can also form the more potent hydroxyl radical through the Fenton reaction.[24] On the other hand, hydroxyl radicals are very short lived and highly reactive and therefore will result in the majority of damage near their production site.

In the first 10 min of irradiation, Ce6 and PS1 produced ~0.2 μM of hydrogen peroxide, while PS2 and PS3 produced ~0.37 μM hydrogen peroxide (**Figure 22a**). PS2 and PS3 again have similar kinetics within the first 10 min. After 10 min, the rate of hydrogen peroxide production by Ce6 and PS1 decreased. The rate of hydrogen peroxide production from PS3 increased after 10 minutes. After 10 min, PS2 diverged from the PS3 kinetics, first decreasing hydrogen peroxide production and then at 60 min resuming at a rate similar to that of PS3 from 10-60 min. In a previous study, a fluorescein-TPP conjugate did not have altered ROS production compared to fluorescein alone, indicating that the interaction of TPP with Ce6 in PS2 and PS3 is unique.[23]

All four PSs had similar hydroxyl radical production kinetics over 60 min (**Figure 22b**). Ce6 produced ~1.5-fold greater hydroxyl radicals than the other three PSs, indicating that the conjugation of Ce6 reduces its ability to produce hydroxyl radicals.
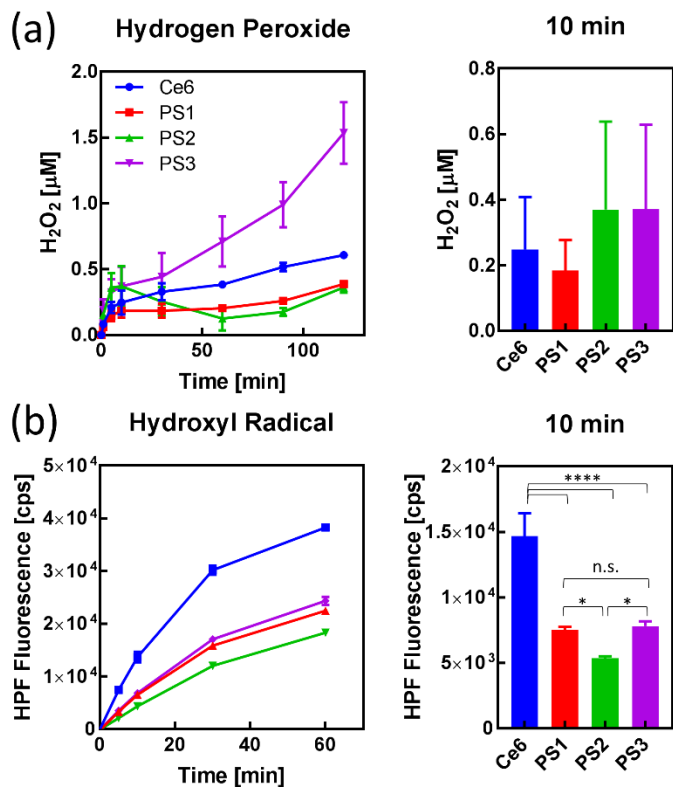
Figure 22. (a) Hydrogen peroxide or (b) hydroxyl radical production by PS irradiation with 650 nm, 0.84 mW/cm^2 light. Bar plot shows comparison at 10 min, the time used for in vivo PDT. n≥3.

4.4.3 Targeting ligand alters cellular concentration of PSs

Addition of organelle targeting ligands to Ce6, altered the amount of PS that accumulated in cells (**Figure 29**). The two TPP ligands on PS3, resulted greater cell uptake. PS1 had higher cell uptake compared to Ce6 and PS2, although the differences was not statistically different.

4.4.4 PDT efficacy in lysosomes is dependent on type of ROS

We first wanted to determine whether targeting ligands effected therapeutic efficacy.

Both PS1 and PS2 localize in the lysosome at 4 h, but they have different targeting ligands. When activated with light for 10 min, at 3.25 mW/cm^2, PS2 killed 82% of cells while PS1 only kill 50% (**Figure 23a**). Minimal dark toxicity was observed for either PS.

A possible explanation for this is the difference in type of ROS produced by each PS. At 10 min of irradiation, PS2 produces ~2-fold greater hydrogen peroxide than PS1. However, PS1 produces ~1.4-fold greater hydroxyl radicals than PS2. This suggests that hydrogen peroxide produced in the lysosomes is more lethal to cells than hydroxyl radicals produced in the lysosomes. Hydrogen peroxide can diffuse out of the lysosome resulting oxidative stress in other parts of the cell, while hydroxyl radicals are so short lived that they can only cause damage to the lysosome. Lysosomal damage does not always result in cell death and in cancer upregulation of HSP70 can aid in stabilization of the lysosome membrane, reducing risk of LMP formation.[25-28] Therefore, when developing PS targeted to the lysosomes, it is ideal to use hydrogen peroxide producing PSs.
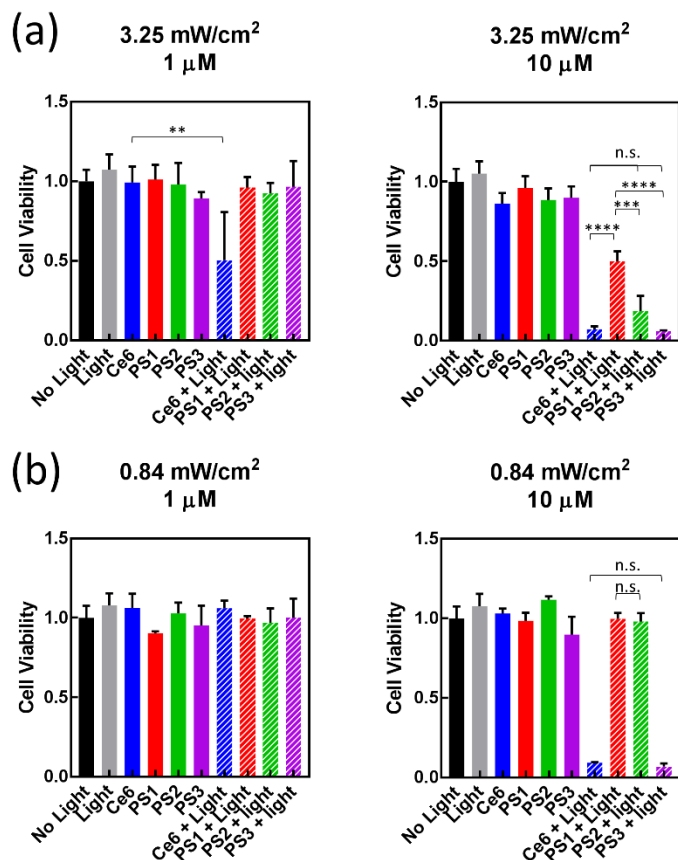
Figure 23. 4T1/luc cells were incubated with 1 or 10 μM of each PS for 4 h, wash and irradiated with 650 nm, (a) 3.25 mW/cm2 or (b) 0.84 mW/cm2 light for 10 min. n≥3.

4.4.5 Enhanced cell uptake of PS3 resulted in greater cell death

PS2 and PS3 produce same amount of hydrogen peroxide at 10 min, while PS1 and PS3 produced the same amount of hydroxyl radicals at 10 min. However, PS3 resulted in 90% cell death at 0.84 mW/cm^2 when PS2 and PS1 resulted in 0% cell death (**Figure 23b**). Therefore, the difference in death is either due to the fraction of PS3 localized to the mitochondria or the high intracellular concentration of PS3. After normalization of intracellular concentration, PS2 and PS3 resulted in the same amount of cell death (**Figure 23b**).

4.4.6 PDT efficacy enhanced in ER

At the highest light dose and PS dose, 3.25 mW/cm^2 and 10 μM, respectively, both Ce6

and PS3 killed ~95% of cells. When the PS dose was reduced to 1 μM, only Ce6 resulted in cell death which was reduced to ~50% (**Figure 23a**). For both Ce6 and PS3, the light dose could be reduced to 0.84 mW/cm^2 with 10 μM PS, maintaining 90% cell killing (**Figure 23b**). However, when the PS dose was reduced to 1 μM no cell death was observed.

4.4.7 Normalization of intracellular PS concentration

Next we altered the starting concentration of each PS in order to obtain the same intracellular concentration across all PSs, ensuring the difference in PDT efficacy is due to organelle specific damage and not amount of PS. An intracellular concentration of ~0.5 μM was obtained in by each PS after 4 h of incubation (**Figure 24a**). The cells were then washed and irradiated with a high light dose, 3.25 mW/cm^2. As with the previous experiments, ER PDT was most effective at killing cells, although, there was no significant difference between ER PDT and lysosomal PDT with PS2 (**Figure 24b**).

Interestingly, there was a greater discrepancy between lysosomal PDT with PS1 and PS2 than previously observed. Both PSs have negligible dark toxicity indicating that the difference in PDT is due to differential ROS production (**Figure 22**). Therefore it is important to consider not only the quantity of ROS produced but the type of ROS.

Moreover, PS2 was more potent than PS3, although not significantly. This was an unexpected result considering the body of literature that showed dual organelle treatment more effective than a single organelle treatment,[4-5] and that mitochondrial PDT is more effective than lysosomal PDT.[10]
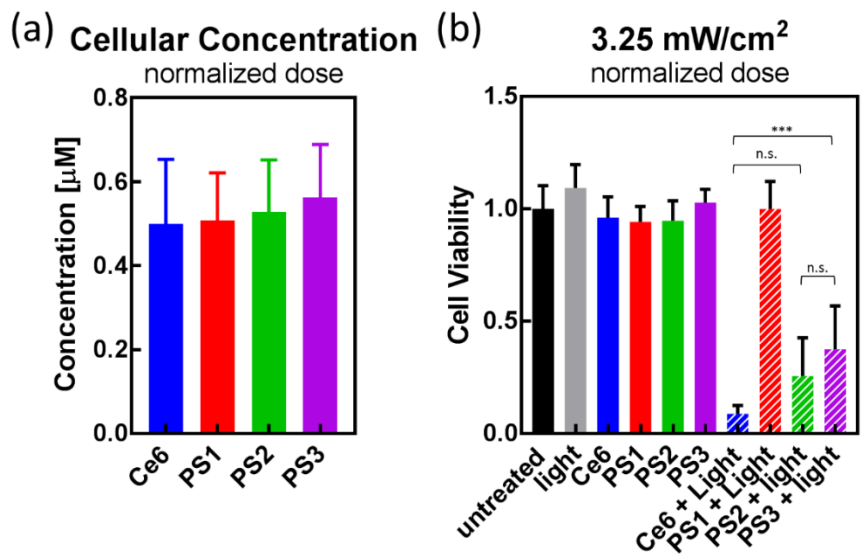
Figure 24. (a) Concentration of PSs in cells after 4 h of incubation with different starting

concentrations PS. (b) Cell viability after PDT with 0.5 μM of intracellular PS. n=3.

4.5 Conclusion

All of the Ce6 based PSs initially bind to the membrane of cells and subsequently

internalize and traffic to specific organelles. Interestingly, we found the subcellular localization

of Ce6 at 4 h is the ER. This has only been reported in one other study[22] and most previous work

have reported that Ce6 is localized to the cytosol, lysosome, or mitochondria. Based on studies of

the pH dependent interaction of Ce6 with lipid membranes, it is possible that the discrepancy in

subcellular localization arises due to differences in cell specific plasma membrane lipid

composition, the pH of the cell growth media, or the intracellular cytosolic pH.[20-21]

In addition, targeting Ce6 with a one or even two TPP, was not sufficient to result in full

localization to the mitochondria. Alterations in the TPP structure, such as methylation of the

phenyl groups, could aid in increasing mitochondrial uptake.[23]

Conjugation of a targeting ligand to Ce6, altered the kinetics of amount of hydroxyl

radicals and hydrogen peroxide produced upon light activation. The difference in type of ROS

produced greatly affected the efficacy of lysosomal PDT, resulting in the hydrogen peroxide producing PS2 to be more potent than PS1.

Through direct comparison of ER, lysosomal, and mitochondrial PDT we have found that ROS production in the ER results in the greatest cell death. ER PDT maintained up to 90% loss in viability, with a light dose of 0.84mW/cm^2 and intracellular concentration of 0.7±0.2 μM. ROS produced in the ER can activated apoptosis through release of high concentrations Ca^{2+}.[29-30] Moreover, ROS induced ER stress can also induce build-up of unfolded or misfolded proteins prompting activation of the unfolded protein response (UPR).[31] UPR can promote the formation of stable complexes of heat shock proteins (HSP) with tumor antigens. When released from the cell, due to necrosis, these antigens can stimulated inflammation and activation of cytotoxic T-cells.[1,9] Previous studies of ER PDT with the PS, hypericin, have found upregulation of cytokines potentially involved in anti-tumor immunity.[13-15] The ability of ER PDT to activate tumor regression through multiple mechanisms (e.g. direct cell death, and activation of the immune system) makes it a promising modality for cancer therapy.

In conclusion, when conducting organelle specific PDT it is vital maintain consistency in the PS used for each organelle and the amount of PS in each organelle, without which the therapy is not comparable. With these considerations in mind, we have found the ROS production in the ER results in the greatest therapeutic efficacy. In the future, we will investigate if Ce6 ER PDT can stimulate additional mechanisms of tumor regression, such as activation of the immune system.

4.6 Supporting information
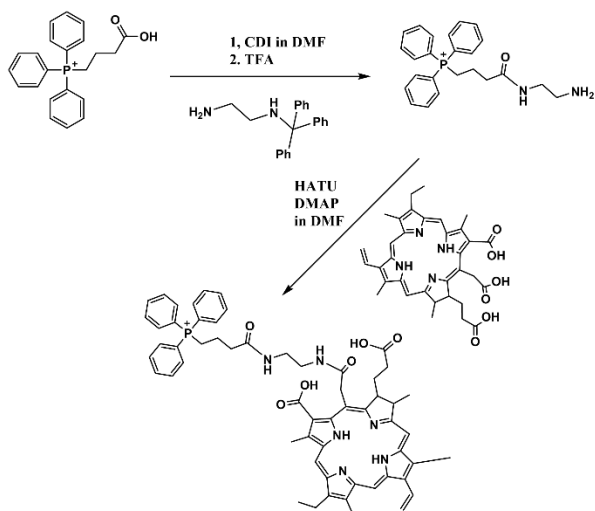
Figure 25. Synthesis of PS2.
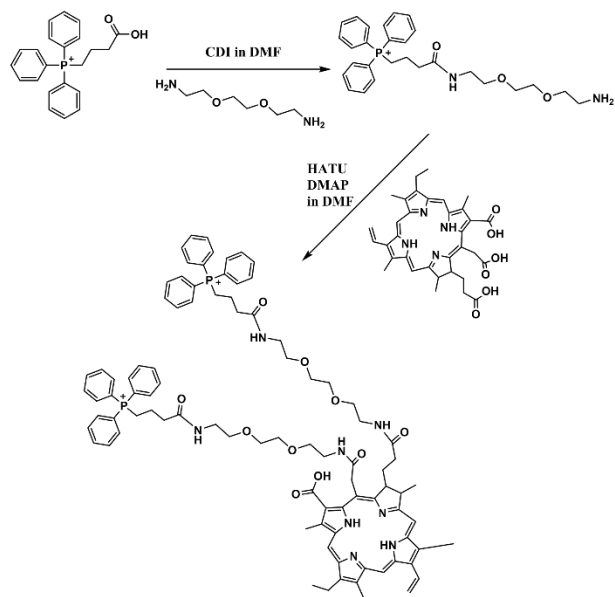
Figure 26. Synthesis of PS3.
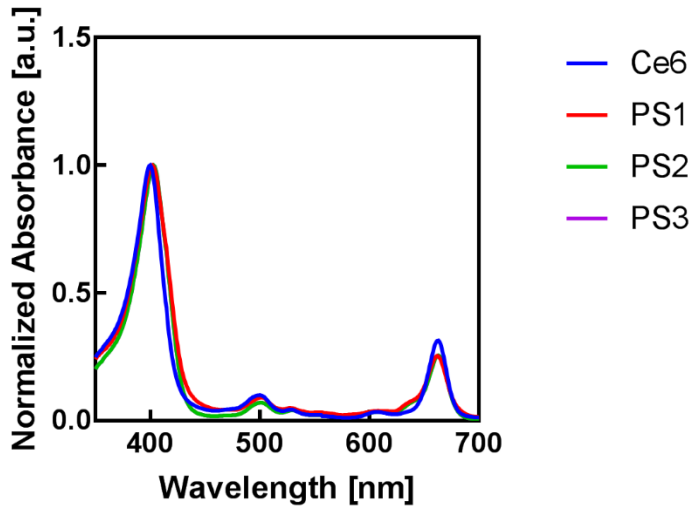
Figure 27. Normalized absorption for all PSs.
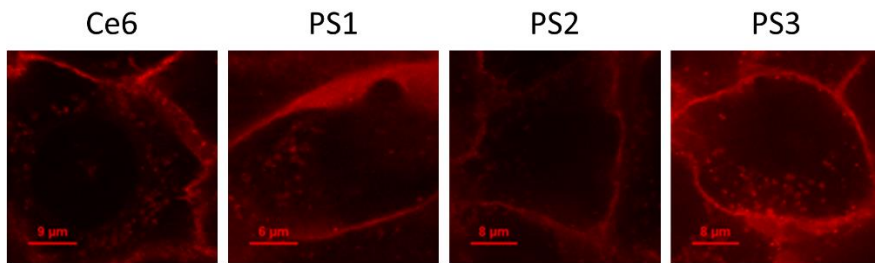
Figure 28. PS initially bind to plasma membranes before internalization.
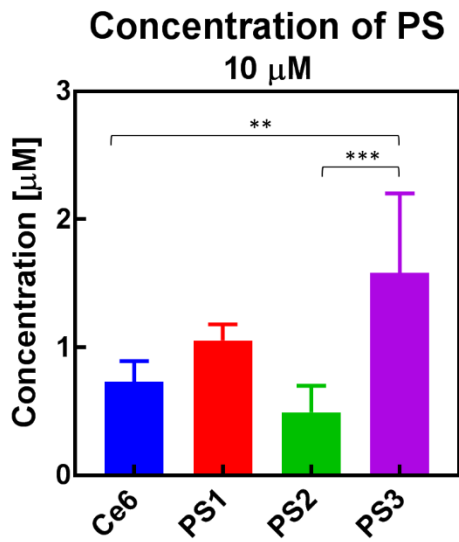
Figure 29. Intracellular concentration of all PSs.
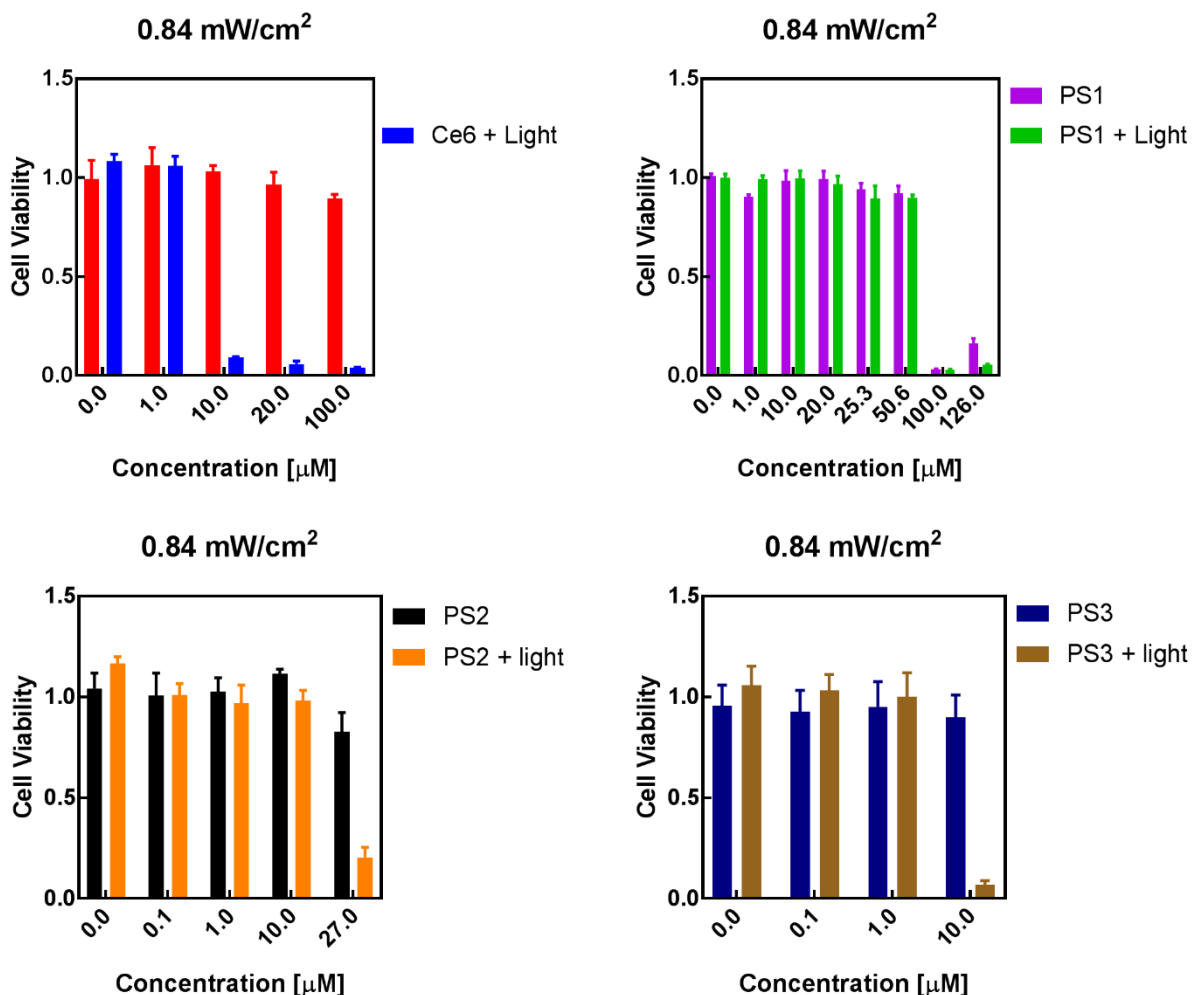
Figure 30. Cell viability at varying concentrations of PSs.

4.7 Acknowledgments

4.8 References

(1)   Castano, A. P.; Mroz, P.; Hamblin, M. R. *Nat. Rev. Cancer* **2006**, *6*, 535.

(2)   Brunk, U. T.; Ericsson, J. L. E. *Histochem. J.* **1972**, *4*, 479.

(3)   Aits, S.; Jaattela, M. *J. Cell Sci.* **2013**, *126*, 1905.

(4)   Aggarwal, N.; Santiago, A. M.; Kessel, D.; Sloane, B. F. *Breast Cancer Res. Treat.* **2015**, *154*, 251.

(5)   Kessel, D. *J. Porphyrins Phthalocyanines* **2016**, *20*, 302.

(6)   Liu, L.; Zhang, Z.; Xing, D. *Free Radic. Biol. Med.* **2011**, *51*, 53.

(7)   Orrenius, S.; Zhivotovsky, B. *Nat. Chem. Bio.* **2005**, *1*, 188.

(8)   Tait, S. W.; Green, D. R. *Nat. Rev. Mol. Cell Biol.* **2010**, *11*, 621.

(9)   Kim, I.; Xu, W.; Reed, J. C. *Nat. Rev. Drug Discov.* **2008**, *7*, 1013.

(10)   Lv, W.; Zhang, Z.; Zhang, K. Y.; Yang, H.; Liu, S.; Xu, A.; Guo, S.; Zhao, Q.; Huang, W. *Angew. Chem. Int. Ed.* **2016**, *55*, 9947.

(11)   Kessel, D.; Reiners, J. J., Jr. *Photochem. Photobiol.* **2015**, *91*, 931.

(12)   Buytaert, E.; Callewaert, G.; Hendrickx, N.; Scorrano, L.; Hartmann, D.; Missiaen, L.; Vandenheede, J. R.; Heirman, I.; Grooten, J.; Agostinis, P. *FASEB J.* **2006**, *3*, 756.

(13)   Garg, A. D.; Krysko, D. V.; Vandenabeele, P.; Agostinis, P. *Cancer Immunol. & Immunother.* **2012**, *61*, 215.

(14)   Barathan, M.; Mariappan, V.; Shankar, E. M.; Abdullah, B. J.; Goh, K. L.; Vadivelu, J. *Cell Death Dis.* **2013**, *4*, e697.

(15)   Buytaert, E.; Matroule, J. Y.; Durinck, S.; Close, P.; Kocanova, S.; Vandenheede, J. R.; de Witte, P. A.; Piette, J.; Agostinis, P. *Oncogene* **2008**, *27*, 1916.

(16)   Dabrowski, J. M.; Arnaut, L. G. *Photochem. Photobiol. Sci.* **2015**, *14*, 1765.

(17)   Wang, S.; Bromley, E.; Xu, L.; Chen, J. C.; Keltner, L. *Expert. Opin. Pharmacother.* **2010**, *11*, 133.

(18)   Smith, M. C. P.; Luker, K. E.; Garbow, J. R.; Prior, J. L.; Jackson, E.; Piwnica-Worms, D.; Luker, G. D. *Cancer Res.* **2004**, *64*, 8604.

(19)   Bolte, S.; Cordelieres, F. P. *J. Microsc.* **2006**, *224*, 2013.

(20)   Mojzisova, H.; Bonneau, S.; Vever-Bizet, C.; Brault, D. *Biochem. Biophys. Acta* **2007**, *1768*, 2748.

(21)   Mojzisova, H.; Bonneau, S.; Vever-Bizet, C.; Brault, D. *Biochim. Biophys. Acta* **2007**, *1768*, 366.

(22)   Li, Y.; Yu, Y.; Kang, L.; Lu, Y. *Int. J. Clin. Exp. Med.* **2014**, *7*, 1867.

(23)   Hu, Z.; Sim, Y.; Kon, O. L.; Ng, W. H.; Ribeiro, A. J.; Ramos, M. J.; Fernandes, P. A.; Ganguly, R.; Xing, B.; Garcia, F.; Yeow, E. K. *Bioconjug. Chem.* **2017**, *28*, 590.

(24)   Fenton, H. J. H. *J. Chem. Soc., Trans.* **1894**, *65*, 899.

(25)   Kroemer, G.; Jaattela, M. *Nat. Rev. Cancer* **2005**, *5*, 886.

(26)   Boya, P.; Kroemer, G. *Oncogene* **2008**, *27*, 6434.

(27)   Doerks, T.; Copley, R. R.; Schultz, J.; Ponting, C. P.; Bork, P. *Genome Res.* **2002**, *12*, 47.

(28)   Nylandsted, J.; Rohde, M.; Brand, K.; Bastholm, L.; Elling, F.; Jaattela, M. *Proc. Natl. Acad. Sci. U. S. A.* **2000**, *97*, 7871.

(29)   Li, G.; Mongillo, M.; Chin, K. T.; Harding, H.; Ron, D.; Marks, A. R.; Tabas, I. *J. Cell Biol.* **2009**, *186*, 783.

(30)   Li, G.; Scull, C.; Ozcan, L.; Tabas, I. *J. Cell Biol.* **2010**, *191*, 1113.

(31)   Delaunay-Moisan, A.; Appenzeller-Herzog, C. *Free Radic. Biol. Med.* **2015**, *83*, 341.

Chapter 5 : Theranostic Molecular System Comprising a Photosensitizer and a Near Infrared Fluorescent Probe Enables Spatiotemporal Imaging and Treatment of Squamous Cell Carcinoma

5.1 Chapter summary

Cutaneous squamous cell carcinoma (SCC) is a common malignancy caused by the malignant transformation of keratinocytes, impacting millions worldwide. Treatment can be challenging when the disease is invasive. Here we developed an SCC12 orthotopic model that recapitulates the morphological disease appearance, along with the histological markers that are consistent with the disease. Using this model, we demonstrate that a novel theranostic agent, LS797, can image and treat SCC when excited with 780 nm and 650 nm light, respectively. In vitro data show that LS797 exhibits selective tumor cell accumulation, and when irradiated with 650 nm light, induces cell death via apoptosis. In mice, the therapy resulted in a reduction in tumor growth rate of 78% and an overall decrease in tumor volume post treatment of 81% compared to the untreated controls. The combination of distinct molecular probe and photosensitizer with a tumor-targeting peptide allows for spatiotemporal tumor detection and therapy.

5.2 Introduction

Non-melanoma skin cancer (NMSC) is comprised of both squamous cell carcinoma (SCC) and basal cell carcinoma, and is the most common cancer worldwide impacting an estimated 2 to 3 million people each year.[1] SCC accounts for approximately 20% of NMSC diagnosed, making it a considerable portion of all cancers.[2,3] Cutaneous SCC is caused by a malignant transformation of epidermal keratinocytes that leads to tumor formation, and has been linked to a number of risk factors including exposure to ultraviolet light, aging, light skin type, and chronic inflammation.[4-8] Unlike basal cell carcinomas, SCCs have high metastatic potential, requiring the development of effective treatment strategies.[3]

73

Numerous treatment options are available for cutaneous SCC. However, large-scale clinical studies have yet to determine a superior treatment option.[9,10] One option for treating SCC is photodynamic therapy (PDT), where light is used to activate a photosensitizer (PS) that in turn induces cell death. Methyl-δ-aminolevulinic acid-PDT (MAL-PDT) is the most common form of PDT for NMSC. Although MAL-PDT can successfully treat 70 to 90% of NMSC, it has not been successful in treating invasive SCC cases. This unfavorable result is likely because MAL-PDT relies on the focal nature of lesions, as the PS is topically applied in suspicious regions. When invasion occurs in more advanced cases of SCC, the topical application of methyl-δ-aminolevulinic acid becomes less practical because of the difficulty in identifying the exact tumor location.

To overcome the limitations in delivering the PS to metastases and invasive portions of the tumor, several targeting methods have been used, such as: nanoparticle formulations, antibodies, and peptide ligands.[11-13] For visualization, most of these compounds rely on the fluorescence produced by the PS, which tends to have low quantum yields, and therefore low signal. In addition, the fluorescence is the visible range which interferes with autofluorescence.

Therefore, we developed a theranostic bioconjugate (LS797) which combines a peptide targeting ligand (cGRD),[14,15] an efficient PS, Ce6, and a near infrared (NIR) imaging molecule, to create a compound that can overcome the challenges of clinical PDT. The NIR fluorescence of cypate prevents overlap in the signal with autofluorescence, allowing for increased contrast between the tumor and uninvolved tissue. We have previously shown that the targeting ligand, cGRD, is able to deliver cypate to a variety of tumor types.[14] Here we demonstrate its ability to deliver Ce6 in addition to cypate, to a SCC model. The targeting of LS797, increases its concentration in the tumor as well as decreases the side effect of skin photosensitivity, by clearing

74

quickly from uninvolved tissue. Excitation of LS797, with 650 nm light, resulted in activation of caspase 9 and apoptosis, in vitro. In the SCC murine model that we developed, activation of LS797, resulted in a decrease in tumor growth and tumor size. The typical scabbing associated with PDT can only be seen in tumors treated with LS797 and light. Finally, an increase in cleaved caspase-3 in tumor histology of treated tumors, supports the in vitro data, that LS797 activates apoptosis. We demonstrate that LS797 allows for efficient tumor targeting, NIR visualization of the tumor and selective PDT.

5.3 Materials and methods

5.3.1 Materials

Fluorenylmethyloxycarbonyl (Fmoc) amino acids and Fmoc-Lys(Boc)-Wang Resin were purchased from AAPPTec (Louisville, KY, USA). Dichloromethane (DCM), acetic acid, thioanisole, phenol, hydroxy benzotriazole (HOBt), N,N-diisopropyl ethylamine (DIEA), N-trityl-1,2-ethanediamine, thioanisol, dimethylformamide(DMF), N,N'-diisopropyl carbodiimide (DIC), trifluoroacetic acid(TFA), thallium(III) trifluoroacetate and O-(7-azabenzotriazol-1-yl)-N,N,N',N'-tetramethyluronium hexafluorophosphate(HATU) were purchased from Sigma-Aldrich (St. Louis, MO, USA). Chlorin E6 was purchased from Frontier-Scientific (Logan, UT, USA). Water was obtained from Millipore Q3 system. SCC12 wells were obtained from Dr. J. Rheinwald. Cells were cultured using DMEM supplemented with 10% FBS, and 1% penicillin streptomycin in a humidified incubator at 5% CO_2 balanced with air at 37°C. The cells were kept at 50-80% confluence. Mass spectrometryt was performed on Shimadzu LCMS2010 system (Columbia, MD, USA) under the positive mode. The UV-vis spectra and fluorescence spectra were recorded on a Beckman-Coulter DU640 spectrophotometer (Indianapolis, IN, USA) and Horiba Jobin Yvon Fluorolog-3 spectrophotometer (Edison, NJ, USA).

5.3.2 Synthesis of LS301 (cypate-cyclic(DCys-Gly-Arg-Asp-Ser-Pro-Cys)-Lys-OH)

LS301 was synthesized according to a previous report.[15] Briefly, the linear GRD peptide, H-DCys(Acm)-Gly-Arg(Pbf)-Asp(tBu)-Ser(tBu)-Pro-Cys(Acm)-Lys(Boc)-OH, was prepared via a CEM Liberty microwave peptide synthesizer (Matthews, NC, USA) on the Fmoc-Lys(Boc)-wang resin. The resin (0.1 mmol) was swelled in DCM for 1 hour before use. Fmoc-amino acids (0.5 mmol, 5 eq), coupling reagent (HBTU, 0.5 mmol, 5 eq) and DIEA (1 mmol, 10 eq) were added to the resin and the mixture was reacted for 15 min under microwave irradiation (50W, 75 °C). The resin was washed with DMF for 3 times. Deprotection of Fmoc group was carried out by treatment of 20% piperidine/DMF for 5 min under microwave irradiation (50W, 75 °C). The peptidyl resin was washed and collected. Cyclization of the peptide to form the disulfide bridge was performed on resin with thallium trifluoroacetate (1.2 eq) in DMF for 90 min. Subsequently, NIR dye cypate (3 eq) is conjugated to the cyclic peptide on solid support at the presence of DIC (5 eq) in DMF to result in LS301 peptidyl resin.
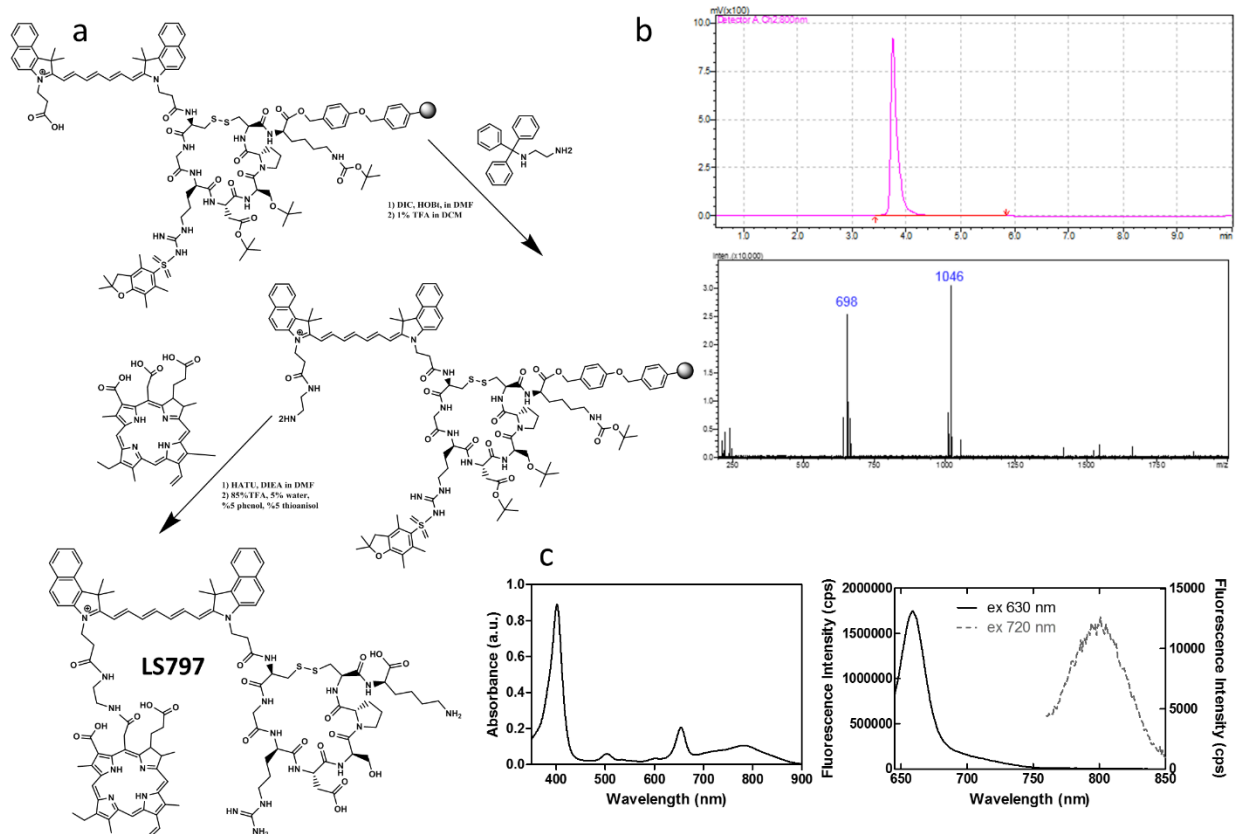
Figure 31. Synthesis and photochemical properties of LS797. (a) Synthesis route of LS797. (b) LCMS spectra of LS797. (c) Absorption and emission of LS797 showing fluoresce emission from Ce6 excitation (630 nm) and cypate excitation (720 nm).

5.3.3 Synthesis of LS797 (Ce6-LS301)

LS301 on peptidyl resin was reacted with N-trityl-1,2-ethanediamine in the presence of DIC in DMF for 16 hours followed by treated with 1% TFA in DCM for 2 hours to de-protect the trityl group. Chlorin E6 (3 eq) was added along with HATU (6 eq) and DIEA (6 eq) in DMF, the peptidyl resin was allowed to react for another 12 hours. The resulted resin was treated with a cleavage cocktail of TFA: thioanisol: phenol: water (85:5:5:5, v/v/v/v) for 90 min at room temperature. The cleaved peptide product was concentrated in vacuo, and then purified on reverse-phase HPLC (Gilson, Middleton, WI, USA). LS797 (Ce6-cypate-cyclic(DCys-Gly-Arg-

Asp-Ser-Pro-Cys)-Lys-OH), M/W 2090, ESI-MS observed 1046 (M+2/2) and 698 (M+3/3) (Fig. S1).

5.3.4 In vitro uptake assay

Uptake assays were conducted using the human skin cancer cell line, SCC12, and the murine fibroblast cell line, 3T3. Cells were cultured on an 8-well slide, (BD Biosciences, NJ, USA), with a 4:1 ratio of SCC12 cells to fibroblasts. The fibroblasts were GFP-expressing. Cells were incubated with 1 μM of LS797 for 4 or 24 hours, washed with PBS and imaged. Confocal microscopy was performed using an FV1000 confocal microscope with a UPLanApo/IR 60X/1.20W water immersion objective lens (Olympus, PA, USA) at 488 nm (GFP) or 785 nm (cypate) excitation laser, and fluorescence was detected at 550/50 nm (GFP), or 850 LP (cypate).

5.3.5 In vitro photodynamic therapy

SCC12 cells were cultured in MatTek dishes (MatTek, MA, USA). Individual dishes were either left untreated, exposed to light at 35 mW/cm^2, for 5, 15, or 30 minutes, incubated with LS797 for 4 hours, or incubated with LS797 for 4 hours and then irradiated. After each treatment was completed, cells were incubated with 1 μM of the caspase-9 sensor, CaspaLux® 9-M2D2, (OncoImmunin, MD, USA) for 30 minutes, and imaged using a confocal microscope (details in above) at 543 nm excitation, and 600/25 nm emission. The cultures were then grown for 3 days, after which they were stained with 0.5 μM of the cell death marker, EthD-1, for 45 minutes and imaged on the confocal at 543 nm excitation and 600/25 nm emission.

5.3.6 Induction of tumors in murine model

All animal studies were performed in compliance with the Washington University Animal Study Committee's requirements for the care and use of laboratory animals in research. Squamous cell carcinoma xenografts were initiated using SCC12 by injecting approximately 2.5x 10^6 cells

into the bilateral shoulder and flank regions of 6-8 week old female athymic NCR-nu/nu mice (22 – 25 g). The SCC12 cells were injected into the intradermal compartment. Tumors were allowed to grow until they were visible and measurable. In some cases, the tumors did not graft, and these regions were not included in the study. The tumor volume was calculated by measuring the length and width of each tumor, and recorded as calculated $V = LW^2$, where V, L, and W are the tumor volume, length, and width, respectively.

5.3.7 In vivo and ex vivo tumor imaging

LS797 was dissolved in 20% DMSO and diluted in 80% PBS to a final concentration of 0.5 mg/kg dose for imaging, or a 6.8 mg/kg dose for therapy. All doses were administered via a 100 µl tail vein injection. The corresponding Ce6 doses were 0.1 mg/kg and 2.0 mg/kg for imaging and therapy studies, respectively.[16,17] Fluorescent imaging was performed using the Pearl NIR fluorescence imaging system, ex/em 785/820 nm (LICOR Biosciences, NE, USA) before injection and up to 24 hours post injection. After 24 hours, the mice were euthanized and organs of interests were removed, placed on a petri dish, and imaged with the Pearl imager. The region of interest (ROI) analysis was performed with the Pearl imaging software. The mean fluorescence intensities were measured for each tissue type to assess the biodistribution of each compound.

5.3.8 In vivo photodynamic therapy

At 4, 8, and 24 hours after a 6.8 mg/kg injection of LS797, the treated tumors were irradiated for 30 minutes. Therapeutic light doses were administered using a 650 nm laser with a power output of 35 mW and a beam area of 1.0 cm^2. For control mice, there was no injection of LS797 and a subset of the tumors was irradiated to obtain untreated controls and light only controls, respectively. For mice injected with LS797, a subset of the tumors was irradiated to obtain LS797 only controls and PDT (LS797 + light).

5.3.9 Histological analysis

Excised tumor tissues were flash-frozen in OCT (Tissue Tek, CA, USA) and stored at –20 ℃. The tumors were sliced at a thickness of 10 μm (Cryocut 1800, IL, USA). Immunohistochemical staining of excised tumor and surrounding tissues was used for histologic validation of tissue types. Immunohistochemistry (IHC) was conducted using an immune-peroxidase method. Primary antibody was diluted in DaVinci Green (BioCare, CA, USA) at the following dilutions: Ki-67 (Thermo Scientific, MA, USA) 1:400, CK-10 (Abcam, MA, USA) 1:400, CK-8/18 (Abcam, MA, USA) 1:200, E-Cad (Abcam, MA, USA) 1:200. Anti-rabbit secondary antibody (Perkin-Elmer, MA, USA) was diluted in PBST at a dilution of 1:800, Streptavidin (Jackson Labs, PA, USA) in PBST at a dilution of 1:1600. A polymer method was used for p53 and CC3 staining with the following dilutions: p53 (Cell Signaling Technology, MA, USA) 1:100, and CC3 (Cell Signaling Technology, MA, USA) 1:10,000. Universal Polymer (Biocare, CA, USA) secondary antibody was diluted in PBST 1:4. All IHC was conducted by the Digestive Diseases Research Core Center – Advanced Imaging and Tissue Analysis Core (DDRCC-AITAC) at the Washington University School of Medicine, St. Louis, MO. Microscopy was performed with an Olympus BX51 upright microscope (Olympus America, PA, USA).

5.4 Results

5.4.1 Development of a skin cancer orthotopic model

We first sought to develop a cutaneous SCC model that would be appropriate for the assessment of PS accumulation in tumors and subsequent PDT. Chemical carcinogenesis animal models have previously been developed using a two-step approach of initiation and promotion. This method generates tumors on the skin after a progression from normal, to papilloma, to differentiated SCC, and then to poorly differentiated SCC.[18] Typically, this process occurs within

20 to 50 weeks, with varying percentages of carcinoma formation. We investigated an orthotopic model in order to decrease the time to tumor development and increase the yield of tumors. An SCC12 orthotopic model was first developed by culturing cells derived from cutaneous SCC biopsies and injected them into nude mice.[19]

We subdermally injected SCC12 cells into the shoulders and flanks of nude mice, and were able to develop tumors within 14 days. These tumors grew in volume for over a month with a doubling rate of 9.45 ± 3.91 days, and progressed through different morphological states (**Figure 32**). The tumors initially appeared as small bumps, next they became erythemic with cystic spaces, and finally they became ulcerative with a central clearing. This final state resembled the gross appearance of cutaneous SCC in humans (**Figure 32**).[20]
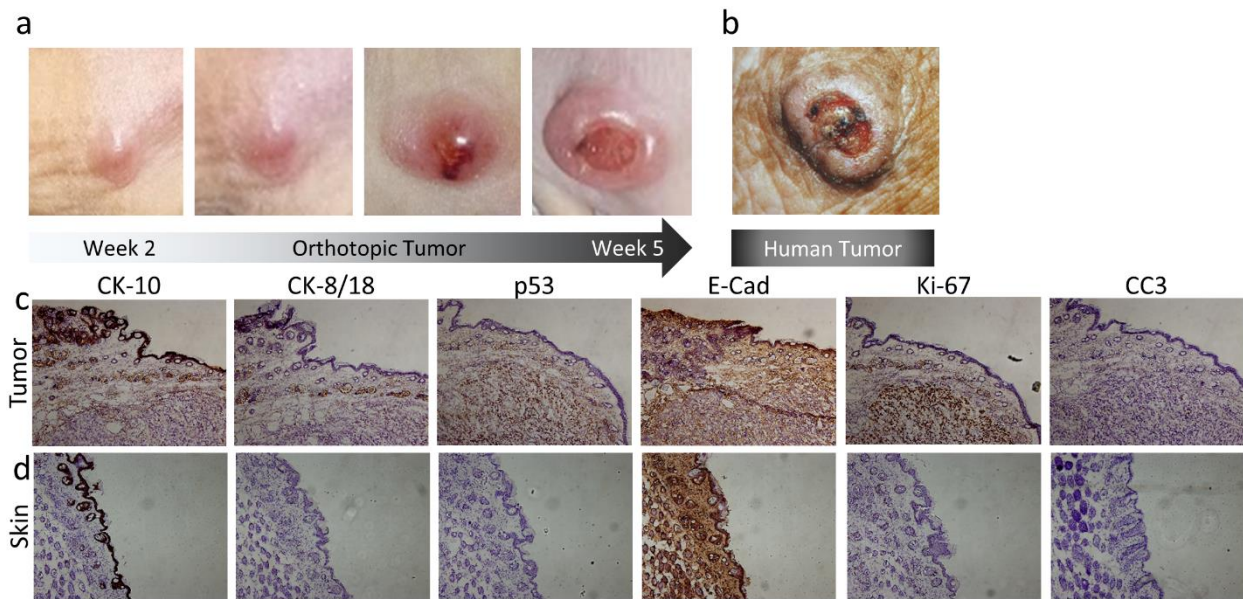
Figure 32. Characterization of SCC12 model formed through subdermal injections of SCC12 cells. (a) Morphologic growth characteristics of SCC12 xenograft, (b) Human SCC, image adapted from Rothnagel et al.[20] (c) SCC12 IHC of tumor, and (d) normal skin. Microscopy conducted at 10x magnification.

After establishing the growth characteristics, the cutaneous SCC12 model was examined using immunohistochemistry (IHC) staining (**Figure 32**). The tumor was sectioned so that the epidermal and dermal layers were visible. Cytokeratin-10 (CK-10) is a type-1 keratin that is produced by keratinocytes and is typically located in the epidermis of normal skin. Mutations in the gene encoding CK-10 are linked to hyperproliferative disorders.[21] CK-10 was expressed in the epidermis of both the normal skin and the tumor. However, the tumor had epidermal thickening and more extensive CK-10 expression. There were small regions of CK-10 expression found throughout the dermis and within the tumor, but these dermal regions of CK-10 expression were not present in healthy skin. Cytokeratin-8 and 18 (CK-8/18) are expressed by secretory epithelia, absent from non-secretory epithelia, and expressed by a range of malignant cells. CK-8/18 was absent from the normal skin, however it was found throughout the tumor section in both the glandular regions and the cellular tumor region. The tumor suppressor gene protein p53 expression is common in cutaneous SCC tumors that originate from ultraviolet DNA damage,[3] and has been shown to be expressed in SCC at higher levels than normal skin.[22,23] p53 was largely absent from the normal skin section and present in the tumor section.[24,25] E-Cadherin was the same between the skin and tumor, indicating that the intracellular epithelial junctions remained intact in our tumor model. Ki-67 is a marker of cell proliferation that is upregulated in cutaneous SCCs compared to normal skin.[24,25] Our model demonstrated increased Ki-67 staining as compared to the healthy skin. Cleaved caspase 3 (CC3) is a marker for cell apoptosis, which was present in the tumor section and largely absent from the skin. The presence of both Ki-67 and CC3 in the tumor indicated that there was increased cellular turnover.

5.4.2 Spectral properties of theranostic agent, LS797

LS797 was synthesized through the conjugation of LS301[26] to Ce6 (**Figure 31**). LS301

served as the tumor targeting and NIR imaging agent (cypate), while the Ce6 acted as the PS. The

resulting LS797 bioconjugate contains the three characteristic absorption peaks of Ce6 at 400 nm,

500 nm and 650 nm, and the absorption peak for cypate at 780 nm (**Figure 31**). The emission peak

of Ce6 was seen at 660 nm when excited at 630 nm and the emission peak of cypate was seen at

800 nm when excited at 720 nm. Due to the minimal spectral overlap of the two fluorophores,

there were no spectral changes in the integrated molecule compared to the fluorophores on their

own.

5.4.3 Evaluation of LS797 as a targeting imaging and therapeutic agent in vitro

To determine the tumor targeting ability of LS797, GFP-expressing 3T3 fibroblasts and

SCC12 cells were co-cultured before adding LS797 to the cultures for 4 or 24 hours. The mean

LS797 fluorescence was greater in the SCC12 cells compared to the fibroblasts, and the contrast

of signal from SCC12 cells compared to fibroblasts increased over time, from 1.6 ± 0.3 at 4 hours

to 2.8 ± 0.3 at 24 hours (**Figure 33**).
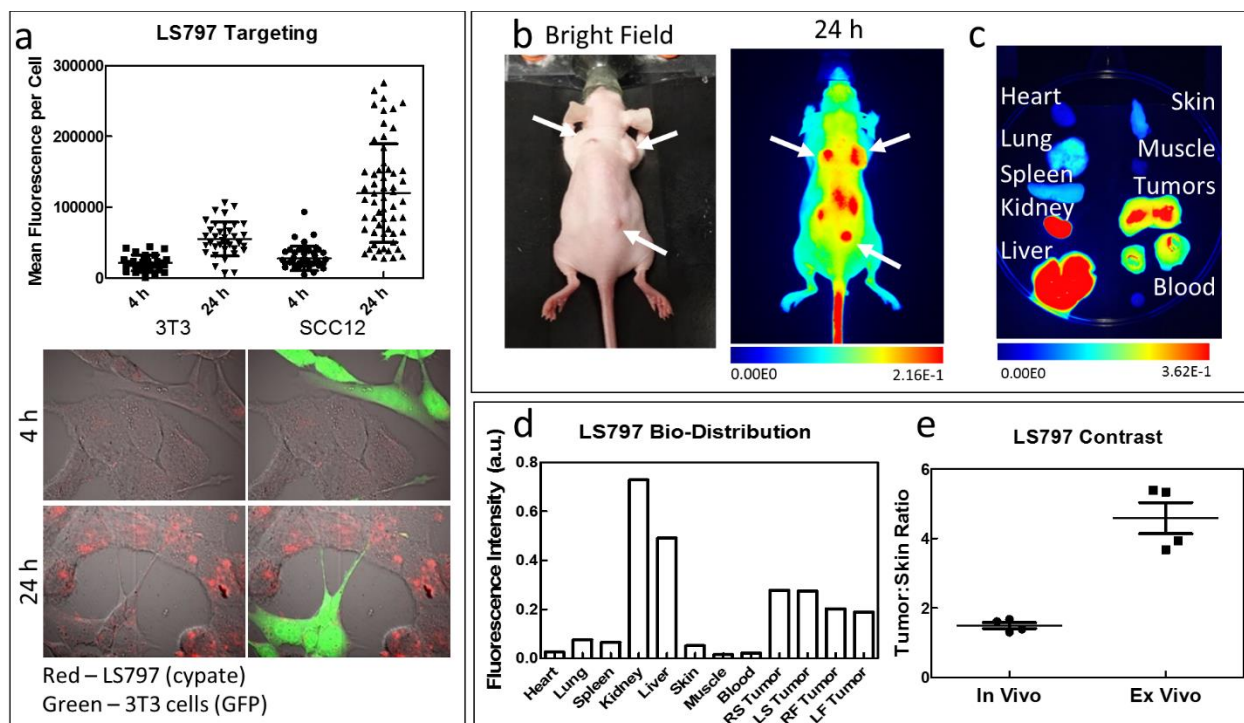
Figure 33. Targeting of LS797 in vitro and in vivo. (a) Quantitative analysis of LS797 internalization into co-cultures of SCC12 cells and 3T3/GFP fibroblasts. Each point represents fluorescence in a single cell. Representative images show LS797 (red) in SCC12 cells and GFP (green) to distinguish the 3T3 fibroblasts. (b) Bright field image of mouse and NIR image at 24 hours post injection. Tumors (white arrows) apparent at 24 hours post injection. (c) Bio-distribution of a mouse injected with LS797. LS797 visible in tumors and excretion organs. (d) Quantification of a bio-distribution. (e) *In vivo* and *ex vivo* tumor to skin contrast (n = 4).

After determining that LS797 targeted tumor cells *in vitro*, we then moved to *in vivo* studies using an SCC12 orthotopic model. An imaging dose of LS797 (0.5 mg/kg, 0.1 mg/kg Ce6) successfully identified tumors from the surrounding normal skin in each of the tumors imaged (**Figure 33**), with an *in vivo* tumor to skin contrast of *1.5 ± 0.09* at 24 hours (**Figure 33**). The kinetics of LS797 show that the compound was primarily localized to the tumors within 4 hours,

and was retained after 24 hours (**Figure 34**). Twenty-four hours after LS797 injection, the mice were sacrificed to obtain a biological distribution of the compound (**Figure 33**). LS797 accumulated in the tumor and the major excretion organs (**Figure 33**). Because the region of interest for the tumors was the skin, the signal from the excretion organs did not obscure visualization of the tumors. The *ex vivo* signal contrast between the tumor and skin was *4.6 ± 0.4*.
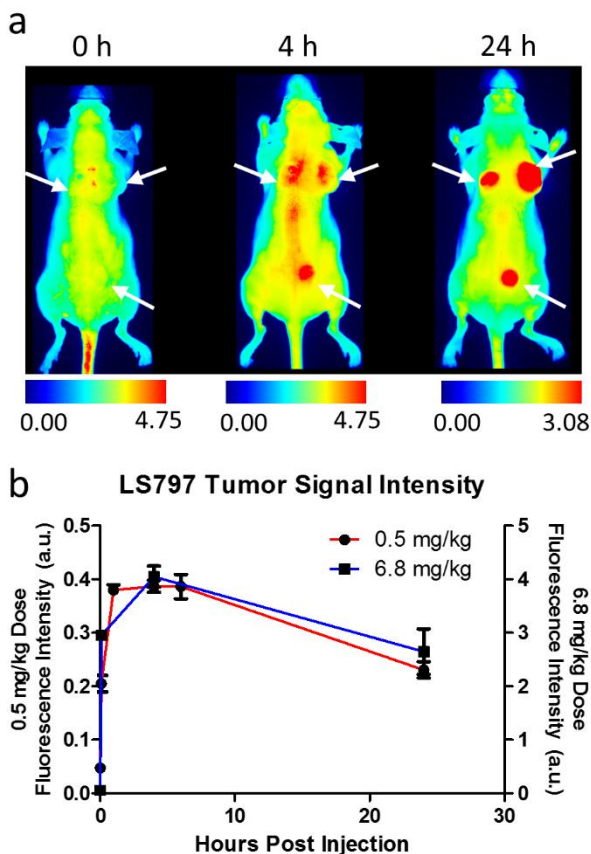
Figure 34. Therapeutic dose of LS797 shows similar kinetics as an imaging dose. (a) Therapeutic dose of LS797 immediately post injection, and at 4 and 24 hours post-injection. Tumors indicated by white arrows. (b) LS797 tumor kinetics to 24 hours post injection (n = 7). Tumor signal maximal at 4 hours and contrast maximal at 24 hours.

A therapeutic dose of LS797 (6.8 mg/kg,) was administered to elicit a dose response to PDT. The kinetics of the therapeutic dose mimicked those of the imaging dose, with initial entry into all tissues followed by localization in the tumor within 24 hours (**Figure 34**). The kinetics of LS797 at therapy dose were virtually the same as imaging dose, with the maximum tumor fluorescence value occurring at 4 hours, and a higher tumor to skin contrast value at 24 hours (**Figure 34**).

5.4.4 Photodynamic therapy in cells causes apoptosis

Once the imaging efficacy of LS797 was demonstrated, its therapeutic efficacy was tested. SCC12 cells were incubated with LS797 (30 μM) for 4 hours and then irradiated with light (35 mW/cm^2) for 5, 15, or 30 minutes to obtain total doses of, 10.5, 31.5, and 63 J/cm^2, respectively. Caspase 9 activity indicates the activation of apoptotic pathways. Increased caspase 9 activation was seen in cells that were irradiated for 15 or 30 minutes. In contrast, only a baseline activation was seen in cells irradiated for 5 minutes (**Figure 35**). Three days after PDT, the cultures were stained with EthD-1 to visualize the dead cells remaining in the culture (**Figure 35**). EthD-1 stains the nuclei of dead cells. Control cell cultures showed sheets of cells with normal cell morphology and minimal EthD-1 staining, indicating cellular damage did not occur. The PDT cultures irradiated for 30 minutes showed high EthD-1 staining along with regions without intact cells. The PDT cultures irradiated for 15 minutes showed regions of morphologically healthy cells and regions of only debris. This variable regional morphology was supported by high levels of EthD-1 staining in some regions and low staining in others. The 15-minute irradiation group also exhibited lower caspase 9 activation, which may explain the limited cell death. The cells irradiated for 5 minutes showed normal morphology. The caspase 9 activation in these cells was similar to the baseline activation seen in the control cells. Based on the three light power settings examined,

these findings suggest that cell death occurred in a light-dose dependent manner, and that 63 J/cm^2 was the minimum light power needed to achieve complete cell death *in vitro*. With lower light doses, caspase 9 activation was still observed, but it was not sufficient to cause apoptosis.
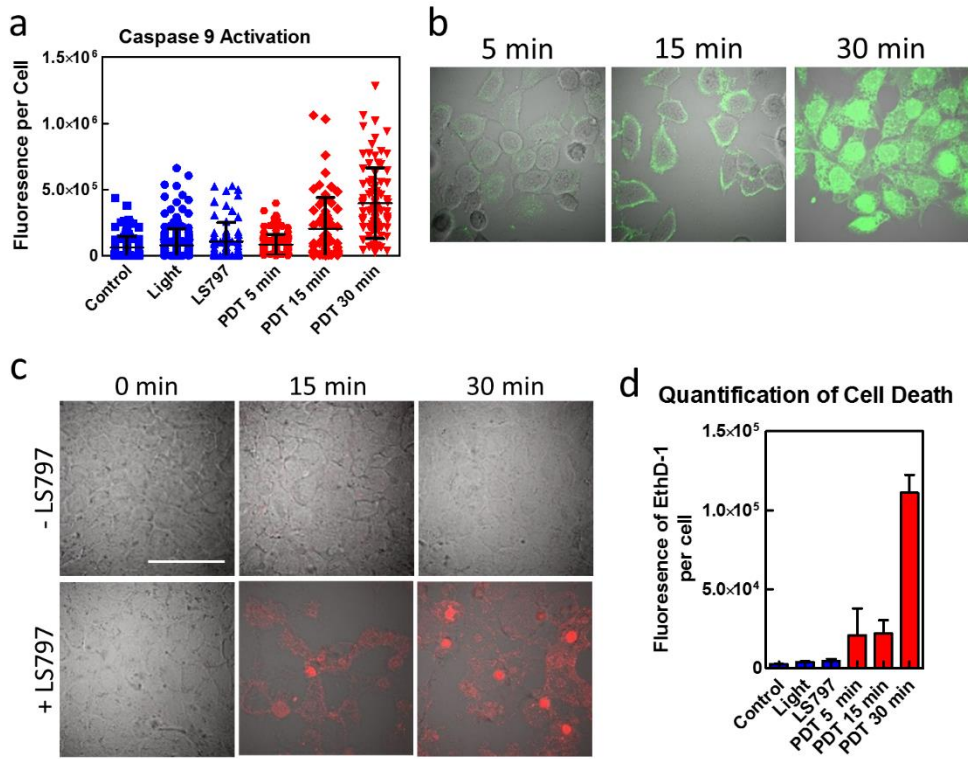
Figure 35. Photodynamic therapy in cells shows caspase 9 activation and subsequent cell death. SCC12 were exposed to light, LS797 or both to determine the efficacy of PDT with LS797. (a) Quantification of caspase 9 activation, 30 minutes after light delivery or at the corresponding time for cells that were not treated with light. (b) Representative images of caspase 9 activation for the PDT-treated cells at different light exposures. (c) Three days after PDT or control treatment, cells were stained with EthD-1, imaged to determine to morphology and the cellular viability. (d) Cell death only occurred in the condition where both light and LS797 were present as shown by the quantification of the fluorescence of EthD-1 per cell.

5.4.5 Photodynamic therapy in animals causes tumor scabbing and regression

For *in vivo* PDT, LS797 was administered via tail vein injection and a 650 nm laser was applied at 4, 8 and 24 hours post-injection. The tumors that were not undergoing light therapy were masked. This approach allowed us to delineate the effects of PDT on tumor growth from LS797 treatment alone. The PDT setup consisted of an LED controller that modulated a 650 nm LED (**Figure 36**). The LED was used with a power output of 35 mW and a spot size of 1 cm^2, giving a total power density of 35 mW/cm^2. Each tumor received a total dose of 189 J/cm^2 over a 24-hour period.
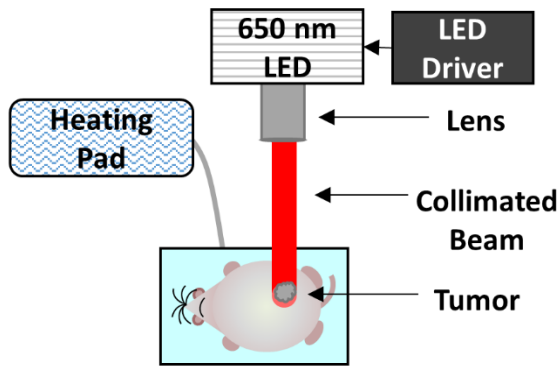
Figure 36. PDT setup with 650 nm LED.

The tumor growth was tracked by measuring the length and width of each tumor, and recorded as a volume. The tumor growth analysis consisted of an average change in tumor growth as a function of the original size, allowing each tumor to serve as its own control. The 24 hours between injection and the final light treatment were considered day zero. Tumor volumes were measured for 6 days before and after day zero and were compared. An average change in tumor volume (ACTV) was calculated for each tumor using Equation 1.

$$\text{ACTV} = (\text{Average}(V_{D(1)} \text{ to } V_{D(6)}) - \text{Average}(V_{D(-6)} \text{ to } V_{D(-1)})) / \text{Average}(V_{D(-6)} \text{ to } V_{D(-1)}) \qquad \text{Eq. 1}$$

Where day 0 is the day PDT occurred, $V_{D(-1)}$ is the tumor volume 1 day prior to PDT, $V_{D(-6)}$ is the tumor volume 6 days prior to PDT, $V_{D(1)}$ is 1 day post-PDT, and $V_{D(6)}$ is 6 days post PDT.
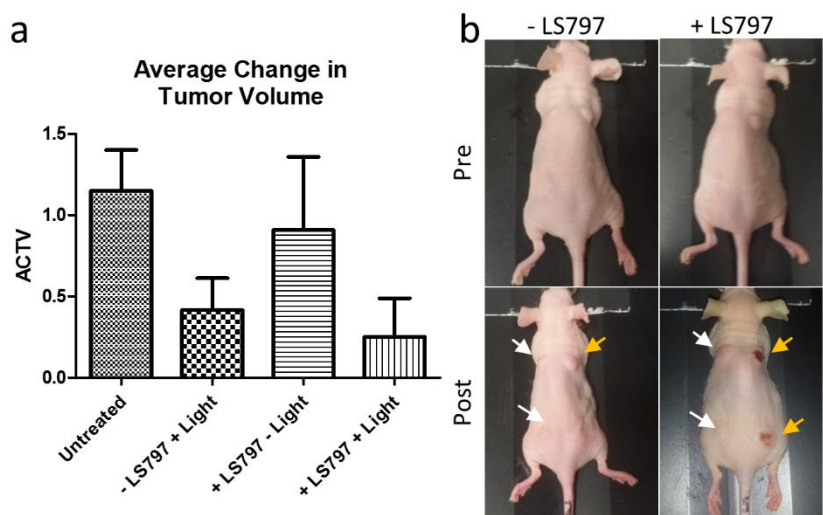
Figure 37. Photodynamic therapy in animals shows scabbing and decrease in tumor volume. (a) Average change in tumor volume, ACTV, demonstrating a decrease in tumor growth with PDT for untreated (n = 3), light only (n = 3), LS797 only (n = 3), and LS797 + light (n = 4). (b) Bright field images of a mouse receiving PDT or light, 24 hours after the start of therapy. Irradiated tumors indicated by yellow arrows and non-irradiated tumors indicated by white arrows.

The tumors treated with LS797 and light initially swelled with PDT, then scabbed and shrank in size over a few days, as is common in PDT. The data showed that the tumors treated with LS797 and light resulted in a lower growth rate (ACTV) as compared to other treatment groups (**Figure 37**). When tumors within a single mouse were compared for LS797 only vs. LS797 with light, the PDT tumors were visibly altered by the therapy (**Figure 37**). Although the tumors exposed to solely light had a reduction in growth rate, the decrease was less than the PDT group, nor exhibit a scabbed appearance. This difference in appearance indicated that LS797 contributed to the enhanced cell death in the PDT group as compared to light alone. The therapy resulted in a

reduction in ACTV of 78% compared to untreated tumors. PDT suppressed the tumor volume for 6 days on average after initial treatment resulting in an overall decrease in tumor volume post therapy of 81% compared to the untreated controls (**Figure 38**). At the conclusion of the study, only a small papule was present in the original location of the tumors treated with PDT (**Figure 38**). IHC analysis of the tumor sections revealed that the PDT tumors had larger regions of apoptosis (CC3 staining) and smaller regions of cell proliferation (Ki-67 staining) compared to the untreated tumors (**Figure 38**), indicating that a mechanism of reduced tumor volume can be attributed to the induction of apoptosis.
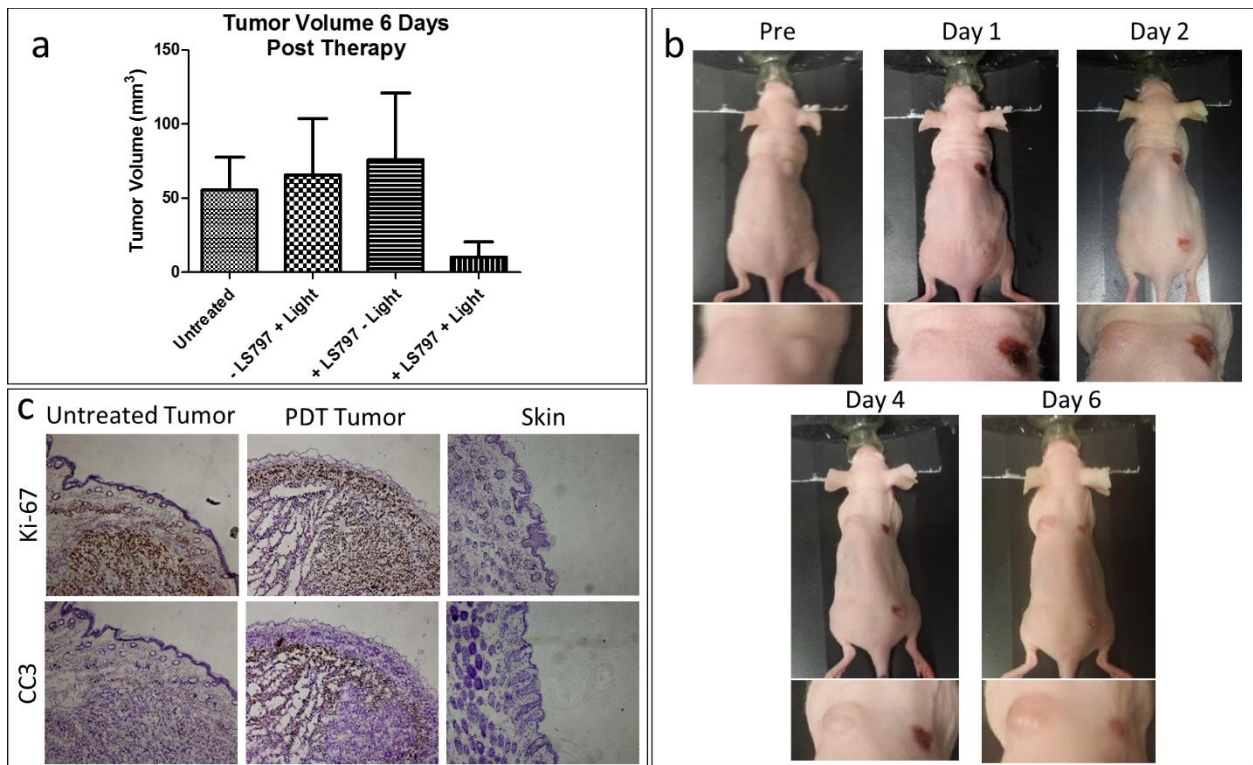
Figure 38. Long-term effects of photodynamic therapy. (a) Tumor volume at 6 days post therapy, untreated (n = 3), light only (n = 3), LS797 only (n = 2), and LS797 + light (n = 2). (b) Tumor morphological appearance pre and post therapy. (c) IHC of the untreated tumor, PDT

tumor, and skin stained for proliferation (Ki-67) and apoptosis (CC3). Microscopy conducted at 10x magnification.

5.5 Discussion

We have characterized a cutaneous SCC model that morphologically resembles human SCC. This orthotopic model develops measurable tumors within 2 weeks after cell injection. We demonstrated that this SCC12 model has differential IHC expression of CK-10, CK-8/18, p53, Ki-67 and CC3, relative to normal skin. The increased Ki-67 and CC3 expression is indicative of the rapid growth and turnover of tumor cells in the dermis.[27] An increase in CK-10 expression supports the increased activity of keratinocytes because of the underlying tumor. This finding is consistent with clinical findings such as hyperkeratosis and keratin horn development in cutaneous SCC.[20] The combination of the IHC profile, the presence of CK-8/18, the upregulation of p53, and the tumor morphological appearance from benign to ulcerating indicates that this orthotopic model recapitulates the pathophysiologic behavior of cutaneous SCC. In contrast to the 50 weeks needed for the two-step chemical carcinogenesis model, our model develops tumors within 2 weeks, which is advantageous for rapid screening and optimization of drugs and imaging agents *in vivo*. Another advantage of an orthotopic model is that injection of tumor cells allows the researcher to know exactly where the tumors will grow on the animal for more precise design of experiments, while avoiding inducing skin pigmentation that is a side-effect of the promotion phase of the chemically-induced model.

The multifunctional theranostic LS797 allows for tumor visualization by optical imaging, followed by PDT. The dual excitation of cypate for imaging, and Ce6 for PDT, provides image guidance for spatiotemporal generation of cytotoxic reactive oxygen species in the tumor region. LS797 may be used to guide surgical resection or tumor margin assessment before or after PDT.

Particularly, LS797 causes visible contrast between the tumor and surrounding skin both when the skin is overlying and after the skin has been reflected. This contrast could allow for visualization of the tumor by a clinician when resecting a tumor surgically, for real-time feedback during procedures such as Mohs surgery. When the residual tumor is detected in the tumor bed, additional light can be applied at the site for added therapeutic efficacy. LS797 may provide an alternative to MAL-PDT as it does not require the treated tumors to be focal in nature for the administration of the agent, allowing for wide-field light application to still induce tumor-specific therapy due to the targeted nature of the agent. Targeted PDT can further enhance the selectivity to treat cancer cells over the normal host cells even at the smaller doses, improving outcomes and reducing potential side effects.

Recently, Ce6 has been used in other theranostic probes that have utilizes self-quenching properties to form activatable nanoparticles, or its pi-pi stacking and hydrophobic interactions to increase loading capacities of graphene nanocarriers.[28-30] Although these techniques have not been tested in vivo, they reveal the possibility of creating PS with an increased level of selectivity and sensitivity. In addition, other formulations of Ce6 have been used to increase water solubility, for example, pluronic F127.[17] Ce6 conjugated to pluornic F127 (PCe6-1) had increased tumor uptake and decreased uptake in uninvolved organs compared to Ce6 alone and had increased therapeutic efficacy. However, the lack of NIR imaging capability makes it difficult to distinguish autofluorescence from PCe6-1 signal, and therefore the compound could not be used to identify tumor metastasis or invasion.

Our initial studies demonstrate that LS797 was able to identify all tumors via NIR fluorescence imaging. LS797-mediated PDT inhibits tumor growth, and activated apoptosis of cell in vitro. The tumor targeting, NIR imaging, and PDT capabilities of LS797 make it a unique

theranostic agent. Further optimization of LS797 dose, light dose, and drug-light interval is necessary in order to reveal the full potential of LS797.

5.6 Acknowledgements

5.7 References

(1)   World Health Organization: 2011; Vol. 2015.

(2)   American Cancer Society: 2014; Vol. 2015.

(3)   Alam, M.; Ratner, D. *N Engl. J. Med.* **2001**, *344*, 975.

(4)   Armstrong, B.; Krickerb, A. *Photochem. and Photobiol.* **2001**, *63*, 8.

(5)   Brash, D.; Rudolph, J.; Simon, J.; Lin, A.; McKenna, G.; Baden, H.; Halperin, A.;
Pontén, J. *Proc. Nat. Acad. of Sci. U. S. A.* **1991**, *88*, 10124.

(6)   Gloster, H. M., Jr.; Neal, K. *J. Am. Acad. Dermatol.* **2006**, *55*, 741.

(7)   Gray, D. T.; Suman, V. J.; Su, W. P.; Clay, R. P.; Harmsen, W. S.; Roenigk, R. K. *Arch. Dermatol.* **1997**, *133*, 735.

(8)   Karagas, M. R.; Greenberg, E. R.; Spencer, S. K.; Stuckel, T. A.; Mott, L. A. *Int. J. Cancer* **1999**, *81*.

(9)   Lansbury, L.; Leonardi-Bee, J.; Perkins, W.; Goodacre, T.; Tweed, J. A.; Bath-Hextall, F. J. *Cochrane Database Syst. Rev.* **2010**, *14*.

(10)   Lansbury, L.; Bath-Hextall, F.; Perkins, W.; Stanton, W.; Leonardi-Bee, J. *B. M. J.* **2013**, *347*, f6153.

(11)   Sato, K.; Nagaya, T.; Choyke, P. L.; Kobayashi, H. *Theranostics* **2015**, *5*, 698.

(12)   Li, R.; Zheng, K.; Hu, P.; Chen, Z.; Zhou, S.; Chen, J.; Yuan, C.; Chen, S.; Zheng, W.; Ma, E.; Zhang, F.; Xue, J.; Chen, X.; Huang, M. *Theranostics* **2014**, *4*, 642.

(13)   Peng, P. C.; Hong, R. L.; Tsai, Y. J.; Li, P. T.; Tsai, T.; Chen, C. T. *Lasers Surg. Med.* **2015**, *47*, 77.

(14)   Mondal, S. B.; Gao, S.; Zhu, N.; Sudlow, G. P.; Liang, K.; Som, A.; Akers, W. J.; Fields, R. C.; Margenthaler, J.; Liang, R.; Gruev, V.; Achilefu, S. *Sci. Rep.* **2015**, *5*, 12117.

(15)   Achilefu, S.; Bloch, S.; Markiewicz, M.; Zhong, T.; Ye, Y.; Dorshow, R.; Chance, B.; Liang, K. *Proc. Nat. Acad. Sci. U. S. A.* **2005**, *102*, 7976.

(16)   Biswas, R.; Moon, J. H.; Ahn, J. C. *Photochem. Photobiol.* **2014**, *90*, 1108.

(17)   Park, H.; Na, K. *Biomaterials* **2013**, *34*, 6992.

(18)   Abel, E. L.; Angel, J. M.; Kiguchi, K.; DiGiovanni, J. *Nat. protoc.* **2009**, *4*, 1350.

(20)   Norman, R. A.; Young, E. M. **2014**, 329.

(21)   Rothnagel, J.; Dominey, A.; Dempsey, L.; Longley, M.; Greenhalgh, D.; Gagne, T.; Huber, M.; Frenk, E.; Hohl, D.; Roop, D. *Science* **1992**, *257*, 1128.

(22)   Einspahr, J. G.; Alberts, D. S.; Warneke, J. A.; Bozzo, P.; Basye, J.; Grogan, T. M.; Nelson, M. A.; Bowden, G. T. *Neoplasia* **1999**, *1*, 468.

(23)   McLaughlin, R. A.; Scolaro, L.; Robbins, P.; Hamza, S.; Saunders, C.; Sampson, D. D. *Cancer Res.* **2010**, *70*, 2579.

(24)   Bagazgoitia, L.; Cuevas Santos, J.; Juarranz, A.; Jaen, P. *Br. J. Derm.* **2011**, *165*, 144.

(25)   Talghini, S.; Halimi, M.; Baybordi, H. *Pak. J. Biol. Sci.* **2009**, *12*, 929.

(26)   Liu, Y.; Bauer, A.; Akers, W.; Sudlow, G.; Liang, K.; Shen, D.; Berezin, M.; Culver, J.; Achilefu, S. *Surgery* **2011**, *149*, 689.

(27)   Verhaegen, M. E.; Mangelberger, D.; Harms, P. W.; Vozheiko, T. D.; Weick, J. W.; Wilbert, D. M.; Saunders, T. L.; Ermilov, A. N.; Bichakjian, C. K.; Johnson, T. M.; Imperiale, M. J.; Dlugosz, A. A. *J. Invest. Derm.* **2015**, *135*, 1415.

(28)   Huang, P.; Xu, C.; Lin, J.; Wang, C.; Wang, X.; Zhang, C.; Zhou, X.; Guo, S.; Cui, D. *Theranostics* **2011**, *240-50*, 10.

(29)   Kim, H.; Kim, Y.; Kim, I. H.; Kim, K.; Choi, Y. *Theranostics* **2013**, *4*, 1.

(30)   Choi, J.; Kim, H.; Choi, Y. *Quant. Imag. Med. Surg.* **2015**, *5*, 656.

Chapter 6 : Protonation and Trapping of a Small pH-Sensitive Near-Infrared Fluorescent Molecule in the Acidic Tumor Environment Delineate Diverse Tumors In Vivo

This chapter is based on a previously published article:

6.1 Chapter summary

Enhanced glycolysis and poor perfusion in most solid malignant tumors create an acidic extracellular environment, which enhances tumor growth, invasion, and metastasis. Complex molecular systems have been explored for imaging and treating these tumors. Here, we report the development of a small molecule, LS662, that emits near-infrared (NIR) fluorescence upon protonation by the extracellular acidic pH environment of diverse solid tumors. Protonation of LS662 induces selective internalization into tumor cells and retention in the tumor microenvironment. Noninvasive NIR imaging demonstrates selective retention of the pH sensor in diverse tumors and two-photon microscopy of *ex vivo* tumors reveals significant retention of LS662 in tumor cells and the acid tumor microenvironment. Passive and active internalization processes combine to enhance NIR fluorescence in tumors over time. The low background fluorescence allows detection of tumors with high sensitivity, as well as delineation of dead or dying cells from healthy cells. In addition to demonstrating the feasibility of using small molecule pH sensors to image multiple aggressive solid tumor types via protonation-induced internalization and retention pathway, the study reveals the potential to use LS662 for monitoring treatment response and tumor-targeted drug delivery.

6.2 Introduction

Aggressive solid tumors utilize enhanced glycolysis for energy production and proliferation, leading to a net increase in intracellular protons relative to that in healthy cells. To remain viable at a normal physiological intracellular pH (pHi) of 7.4, cancer cells actively pump out the excess protons.[1] However, the poor lymphatic function and chaotic vascularization of tumors result in an inefficient buffering or removal of the effluxed protons, leading to a significant reduction in extracellular pH (pHe) from 7.4 to 6.2–6.9.[1,2]

Previous studies have demonstrated that the acidic pHe of solid tumors correlates with an increase in tumor invasiveness and cell proliferation, as well as a decrease in chemotherapeutic efficacy.[1, 3-6] The therapeutic effect of modulating the acidic pHe was demonstrated in preclinical models by oral administration of sodium bicarbonate, which systemically neutralized the pHe of the whole body, including tumors. The systemic neutralization reduced tumor burden and decreased the number of circulating tumor cells.[3, 4, 7-9] These results suggest that the acidic pHe of solid tumors is not only a byproduct of mitochondrial dysfunction and enhanced glycolysis[10] but also represents an important survival pathway that supports tumor growth and metastasis. Thus, the ability to noninvasively image the pHe of tumors affords new means to determine the aggressiveness and severity of cancer or to monitor treatment response.

A variety of molecular imaging probes and nanoparticles have been developed for *in vivo* imaging of pH changes.[2, 11-14] Although chemical exchange saturation transfer (CEST) enhanced magnetic resonance imaging provides depth-independent assessment of pH *in vivo*, the method requires long acquisition times[15] and the use of a high concentration of the CEST contrast agent.[16] For small animal imaging or the assessment of superficial and endoscopically accessible tumors, optical methods represent a high-throughput imaging platform for real-time image display[17] and detection of pH changes *in vivo* via multiple contrast-generating molecular probe designs.

An interesting approach is the wide use of activatable molecular probes to amplify the signal-to-background ratio. This approach has been used successfully to report enzyme activities,[18-24] intracellular pH,[11-13, 25] and intracellular levels of reactive oxygen species.[26] To combine targeted delivery with fluorescence enhancement *in vivo*, recent studies have conjugated pH-sensitive dyes to tumor-targeting ligands such as RGD peptides,[11] where the progressive pH

98

decrease along the endocytotic pathway culminates into high fluorescence in the lysosomes of tumor cells.[11-13] The pK_a of pH sensors can be tuned to minimize background fluorescence in nonacidic cell compartments or tissue environments. However, tumor heterogeneity dictates significant variability in the expression of the targeted proteins in tumor cells. When pH sensors are conjugated to tumor-targeting ligands, the primary mode of fluorescence enhancement for the pH sensors is through intracellular acidic organelles, with limited access to the acidic extracellular tumor environment.

In this study, we have developed a pH-sensitive molecule, LS662, for noninvasive imaging of the acidic pHe of solid tumors. We demonstrate that protonation of the small NIR fluorescent molecule (~700 Da) in the mildly acidic environment of diverse solid tumor types induces an absorption spectral shift from the visible to the NIR region. We used the ensuing NIR fluorescence to successfully identify three different tumor models, including syngeneic and spontaneous murine and human xenograft tumors. The selective retention of LS662 in tumor cells and the acidic environment for over 3 days suggests that protonation traps the small molecule and facilitates its internalization in cancer cells without conjugating the dye to a tumor-targeting protein or peptide.[11] This study demonstrates the potential use of LS662 for interrogating physiologic parameters in a broad range of cancers.

6.3 Materials and methods

6.3.1 Materials
All chemicals were purchased from Sigma-Aldrich (St. Louis, MO, USA) and were used without further purification. ^{1}H NMR data were recorded on a Varian 400 MHz spectrometer (Palo Alto, CA, USA) at ambient temperature in DMSO-d_6 and referenced to tetramethylsilane

(TMS) as an internal standard. Mass-spectrometry was recorded on a Shimadzu LCMS2010 ESI-TOF mass Spectrometer (Columbia, MD, USA).

Dulbecco's modified Eagle's medium (DMEM) culture medium, fetal calf serum, and penicillin–streptomycin were purchased from Gibco (Life Technologies, NY, USA). Vectashield was purchased from Vector Laboratories (CA, USA).

Human epidermoid cancer (A431) cells were obtained from ATCC (VA, USA), and 4T1/luc murine breast cancer cells were obtained from David Piwnica-Worms, Washington University in St. Louis.[27] Cells were cultured using DMEM supplemented with 10% FBS and 1% penicillin–streptomycin in a humidified incubator at 5% CO_2 balanced with air at 37 °C. The cells were kept at 50–80% confluence.

Female BALB/c and female athymic NCr-nu/nu mice were obtained from Charles River Laboratories (MA, USA). Female PyMT mice were bred in-house. All animal studies were performed with accordance with protocols approved by the Washington University School of Medicine Animal Studies Committee.

6.3.2 Synthesis of pH-Sensitive NIR fluorescent dye LS662

The synthesis of LS662 is summarized in (**Figure 40**). A mixture of Vilsmeier reagent 1 (1.1 g, 3 mmol) and 4-carboxylphenyboronic acid (1 g, 6 mmol) was heated overnight under reflux in DMF in the presence of potassium acetate (66 mg, 0.69 mmol) and tetrakis(triphenylphosphine)palladium(0) (0.22 g, 0.19 mmol). The reaction mixture was allowed to cool to room temperature, and DMF was evaporated. HPLC purification of product 2 afforded 0.67 g of a blue-green solid (55% yield). A mixture of indolenium sulfonate 3 (100 mg, 0.38 mmol) and Suzuki product 2 (73 mg, 0.18 mmol) was heated under reflux in the presence of

sodium acetate (55 mg, 0.67 mmol) in 10 mL of an ethanol/acetic anhydride solution (50/50, v/v) for 20 h. After cooling, 2 mL of a 3% aqueous HCl solution was added to the resultant mixture. The crude product was purified by reverse-phase C-18 column chromatography, and the desired compound was eluted with CH3CN/H2O (57 mg; 45% yield); 1H NMR (400 MHz, DMSO-d6) δ 1.26 (s, 12 H), 1.90 (m, 2H), 2.60 (m, 4H), 6.96 (d, J = 14 Hz, 2H), 7.04 (d, J = 8 Hz, 2H), 7.34 (d, J = 8 Hz, 2H), 7.52 (d, J = 8 Hz, 2H), 7.61 (s, 2H), 8.15 (d, J = 8 Hz, 2H). ESI-MS: m/z 701 (M + H, 100%).

6.3.3 Spectral properties and pK_a of LS662

The absorption and emission spectra of LS662 were recorded on a spectrophotometer (Beckman DU640, CA, USA) and fluorometer (Fluorolog-3, Horiba Jobin Yvon, NJ, USA), respectively. Determination of the absorption and emission maxima was reported in solutions with pH values below and above 5. The fluorescence quantum yield of LS662 in PBS was determined by using a literature method and referenced to indocyanine green dye.[11] For pH titrations, LS662 was dissolved in 30 mL of water. 175 mg of NaCl (0.003 mmol) was added to provide a relative constant ionic strength of 0.1 M. The initial solution was acidified with dilute aqueous HCl (0.1 M) to achieve a pH of 2.34. Increment changes of the pH value were achieved by adding a small amount of dilute NaOH (vary from 0.1 to 0.0001 M) into the dye solution. The pH of the solutions was measured with a pH meter (Accumet AB15, MA, USA). At each pH point, the absorption and fluorescence spectra were recorded. The pKa of LS662 was determined using sigmoidal dose–response curve fitting software (GraphPad Prism 5.0, CA, USA).

To obtain optical images of the dye at pH 6.0 and 6.5, 2-(N-morpholino)ethanesulfonic acid (MES; 1 M) was prepared in water and titrated with NaOH to the appropriate pH. For pH

7.0 and 7.5 medium, 4-(2-hydroxyethyl)-1-piperazineethanesulfonic acid (HEPES; 1 M) was prepared in water and titrated with HCl or NaOH to the appropriate pH. These solutions were diluted with phenol red- and bicarbonate-free DMEM to obtain a final concentration of 20 mM. LS662 (10 μM) was dissolved in each solution (100 μL) in a 96-well plate and imaged on the Pearl NIR fluorescence imaging system, ex/em 785/820 nm (LICOR Biosciences, NE, USA).

6.3.4 Blocking and pH variable internalization

A431 cells were grown in 96-well plates (BD Biosciences, NJ, USA). The cells were treated with 1 μM LS662 for 1–8 h in either acidic (pH 6.4) or neutral (pH 7.4) medium. Acidic medium was made by adding 25 μL of 1 M HCl per 1 mL of medium. For blocking studies, 10 mM sodium azide, an active transport inhibitor, was coincubated with the cells. After treatment, the cells were rinsed with PBS and imaged using a BX-51 epifluorescent microscope (Olympus, PA, USA). A cy5 U-N41008 (Chroma Technology Corp., VT, USA) filter cube was used for excitation at 620/60 nm and emission collection at 700/75 nm.

4T1/luc cells were grown in an 8-well slide (BD Biosciences, NJ, USA). The cells were treated with 10 μM LS662 or 1 μM cypate for 2 or 8 h in either acidic (pH 6.4) or neutral (pH 7.4) medium. After treatment, the cells were rinsed with acidic or neutral medium and imaged using a FV1000 confocal microscope with an UPLanApo/IR 60×/1.20W water immersion objective lens (Olympus, PA, USA) at 633 nm (LS662) or 785 nm (cypate) excitation, and fluorescence was detected at 690/50 nm (LS662) or 850 LP (cypate).

6.3.5 Cell death assay

A431 cells were grown on 8-well microscope slides (BD Biosciences, NJ, USA). To determine if LS662 preferentially stains dead cells, three conditions of A431 cells were incubated with 1 μM LS662 or 1 μM cypate for 2 h: healthy cells (cell in medium with LS662),

dying cells (cell incubated with PBS with LS662), and dead cells (cell pretreated with 50% ethanol in PBS for 30 min, with LS662 added after the treatment with ethanol). After treatment, the cells were rinsed with PBS, mounted with Vectashield (Vector Laboratories, CA, USA), and coversliped. The slides were imaged using a FV1000 confocal microscope with an UPLanApo/IR 60×/1.20W water immersion objective lens (Olympus, PA, USA) at 633 nm (LS662) or 785 nm (cypate) excitation, and fluorescence was detected at 690/50 nm (LS662) or 850 LP (cypate).

6.3.6 Induction of tumors in murine models

All animal studies were performed in accordance with protocols approved by the Washington University School of Medicine Animal Studies Committee. Syngeneic 4T1/luc murine breast tumors were initiated in mice by injecting 5×10^5 4T1/luc breast cancer cells subcutaneously in the right flank of 6–8 week old female BALB/c mice. Imaging studies were performed after the tumors had grown for approximately 10 days to a size of 5–7 mm in diameter. A431 human epithelial carcinoma xenografts were grown in 6–8 week old female athymic NCr-nu/nu mice by bilaterally injecting A431 cells into the mammary fat pad. Imaging studies were conducted after tumors had grown for approximately 15 days to a size of 5–7 mm in diameter. The spontaneous breast cancer mouse model, expressing the polyomavirus middle T antigen via the mouse mammary tumor virus long terminal repeat promoter (PyMT), was bred in-house. Heterozygous mice developed spontaneous, multifocal mammary adenocarcinomas at about 8–12 weeks of age.

6.3.7 In vivo and ex vivo tumor imaging

LS662 or cypate was dissolved in DMSO and then diluted with PBS for a final concentration of 60 µM in 100 µL of 20% DMSO and 80% PBS. The solution was injected

intravenously via the lateral tail vein. Fluorescent imaging was performed using the Pearl NIR

fluorescence imaging system (ex/em 785/820 nm) before injection and at 1, 2, 4, 6, 24, 48, and

72 h postinjection. After 72 h, the mice were euthanized, and organs of interest were removed,

placed on a Petri dish, and imaged with the Pearl imager. Region of interest (ROI) analysis was

performed with Pearl imaging software. The mean fluorescence intensities were measured for

each tissue to assess the biodistribution of each compound. In addition, *in vivo* ROIs for tumor

and normal tissues were used to determine the accumulation of the probe over time. The normal

tissue regions were chosen that did not include any excretory organs or tumors in order to obtain

a reliable background measurement.

6.3.8 Ex vivo multiphoton imaging

After excision, tumors were cut into 1 mm slices and imaged using a custom built two-

photon microscope at the Washington University School of Medicine. The visible emission from

LS662 was excited with a Chameleon XR Ti-Sapphire laser (coherent) and visualized with an

Olympus XLUMPlanFl 20× objective (water immersion, NA 0.95). Fluorescence emission from

collagen, elastin, and LS662 was separated using 515 and 560 nm dichroic mirrors and detected

using the red (560–650 nm), green (490–560 nm), and blue (second harmonic <458 nm) channels

of three-head-type Bialkali photomultiplier tubes.[28, 29] *z*-stack images were acquired by taking 20

sequential images at a step size of 2.5 μm, and 15 video rate frames were averaged for each *z*-

slice. Imaris (Bitplane, MA, USA) and ImageJ (NIH, MD, USA) were used for multidimensional

rendering.[30]

6.3.9 Histological analysis

Excised tumor tissues were flash-frozen in OCT (Tissue Tek, CA, USA) and stored at

−20 °C. The tumors were sliced at a thickness of 10 μm (Cryocut 1800, IL, USA). Fluorescence

imaging was performed with an Olympus BX51 upright epifluorescent microscope (Olympus America, PA, USA). A cy5 U-N41008 (Chroma Technology Corp., VT, USA) filter cube was used for excitation at 620/60 nm and emission collection at 700/75 nm. Muscle samples, taken from the mouse's left leg, were imaged with the above settings as non-tumor control samples. To confirm that lack of LS662 fluorescence was not due to inactivation, acidic PBS (pH 4.0) was added to the sample to activate any LS662. H&E staining of excised tumor and surrounding tissues was used for histologic validation of tissue types.

6.3.10 Statistical analysis

All cell studies were performed in triplicate. The mean fluorescence per image was calculated after background fluorescence subtraction and normalized to the number of cells per image. These values were then averaged, and error bars represent the standard deviation. For in vivo quantification of fluorescence of tumor and normal tissues, the following numbers of replicates were used: three for 4T1/luc tumor and normal, two for A431 tumor and three for A431 normal, and three for PyMT tumor and normal. For ex vivo quantification of tumor and muscle fluorescence, the following numbers of replicates were used: three for 4T1/luc tumor and muscle, two A431 tumor and one for A431 muscle, and three for PyMT tumor and one for PyMT muscle. When more than three replicates were present, the standard deviation was calculated and is displayed as error bars. Statistical significance was calculated using Student's t-test, and p-values less than 0.05 were considered to be statistically significant.

6.4 Results

6.4.1 Synthesis and spectral properties of pH-Sensitive NIR fluorescent dye LS662

We have developed LS662 as a pH-sensitive small molecule for identifying tumors.

Upon protonation in acidic media, the molecule undergoes a significant spectral shift from

visible to NIR wavelengths. The high NIR fluorescence is useful for identifying diverse tumors

(**Figure 39**).
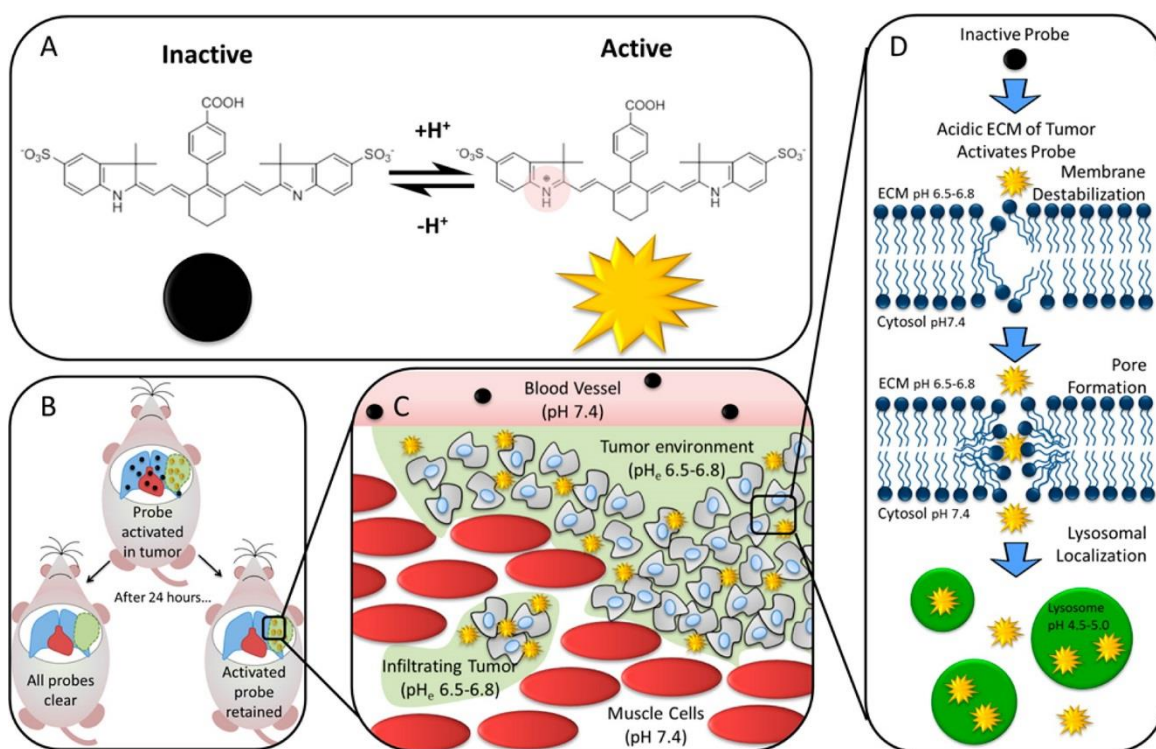
Figure 39. (A) LS662 is a pH-activated probe that becomes highly fluorescent in acidic solution.

(B) *In vivo*, LS662 is activated in tumors, and the inactive probe clears from uninvolved tissue,

simultaneously increasing contrast and decreasing the dose of LS662 at non-tumor regions. (C)

LS662 is selectively activated in an infiltrating tumor. (D) Once LS662 is activated by

protonation of the indolium ring nitrogen, it acts as an amphiphilic small molecule that can

penetrate into tumor cells by destabilization of the cell membrane. Once inside the cell, its activated form can be visualized in the acidic lysosomes.

LS662 was synthesized by modifying our previously reported method (**Figure 40A**). [11] To overcome the low yields of this synthesis, we used modified Suzuki-coupling conditions in which Vilsmeier reagent 1 was reacted with 4-carboxyphenylboronic acid in the presence of tetrakis(triphenylphosphine)palladium(0) and anhydrous potassium acetate. Purified LS662 was obtained as blue-green solid. The dye is stable in powder form; although the aqueous solution can be stored at 4 °C for several weeks, it is best to use freshly prepared solutions for each study. pH titration showed that LS662 has low NIR fluorescence in basic and neutral solutions, displaying an absorption maximum (λ_{abs}) at 503 nm (**Figure 40C**). A significant hypsochromic shift from 503 to 750 nm λ_{abs} and an intense NIR emission maximum (λ_{em}) at 768 nm were observed in acidic solutions (pH < 6), with corresponding pK_a, molar absorptivity (ε), and fluorescence quantum yield (Φ_F) of 5.2, 120 000 M^{-1} cm^{-1}, and 0.025, respectively, in PBS. Protonation of one indolenium ring nitrogen in LS662 converts the molecule into a donor–acceptor fluorophore system, which exhibits a large spectral shift.[11] Pseudocolor fluorescence images of LS662 solutions in buffers of different pH demonstrate the visual changes in fluorescence intensity that take place with increasing pH (**Figure 40D**).
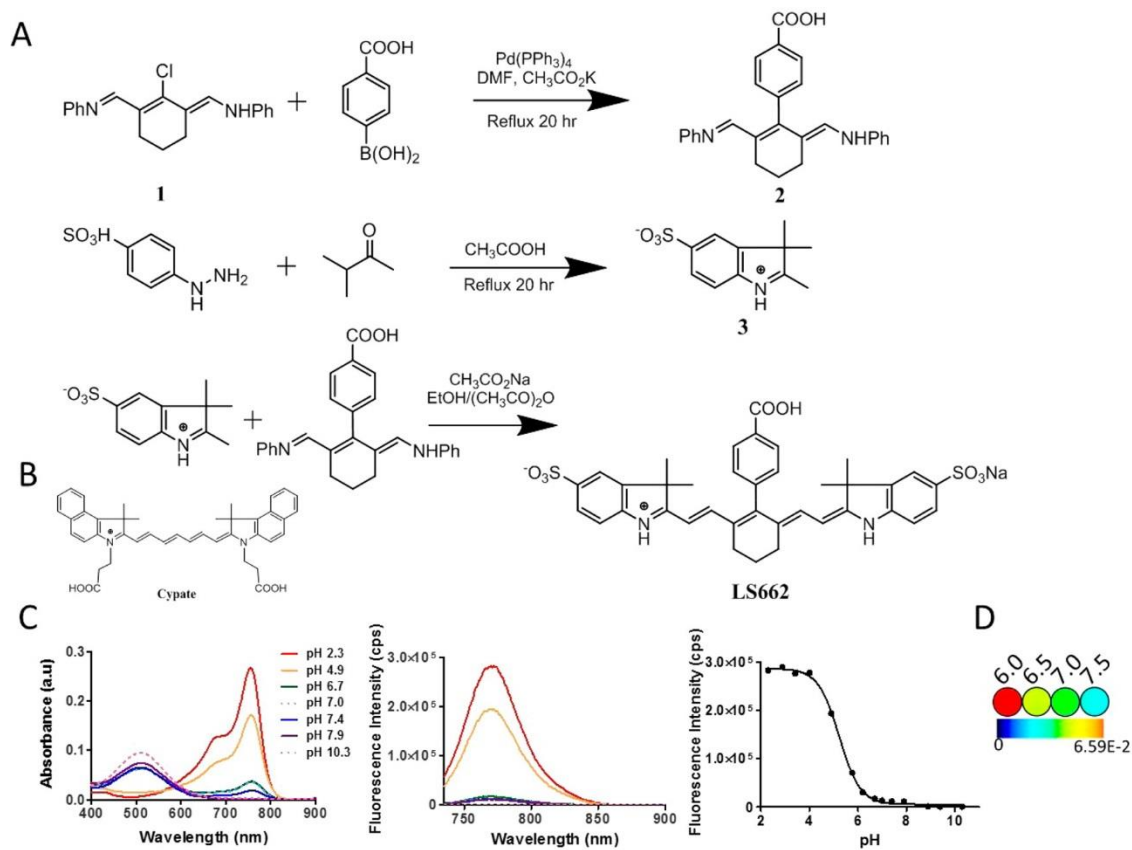
Figure 40. (A) Synthesis route of LS662. (B) Chemical structure of cypate. (C) Absorption and emission spectra of pH-titrated LS662 in water from pH 2 to 10. Absorption in basic solution occurs primarily in the visible range, whereas absorption in acid solution occurs in the NIR region. In acidic solution, excitation at 720 nm results in fluorescence at 758 nm. LS662 has a pK_a of 5.2. (D) Pseudocolor images of a solution of LS662 at pH 6.0, 6.5, 7.0, and 7.5 (see Materials and methods section for solution preparation).

6.4.2 LS662 differentially internalizes in tumor cells via dual ATP-dependent and -independent pathways in neutral and acidic culture media

We postulated that protonation of LS662 under mild acidic conditions found in the pHe of many solid tumors will decrease the molecule's net negative charge, enhance NIR fluorescence, and facilitate internalization in cells. To test this hypothesis, LS662 was incubated

with representative tumor cells (A431 or 4T1/luc) in buffer solutions at pH 7.4 and 6.4 to simulate normal physiological and acidic tumor pHe values, respectively (**Figure 41A**). At pH 7.4, only a few cells exhibited high NIR fluorescence within a 2 h incubation. Longer incubation times showed weak and diffuse NIR fluorescence in nearly all cells. A similar trend was observed in acidic solutions, in which the internalization of LS662 occurred in only a few cells within a 2 h incubation, but it increased significantly at the 8 h measurement time point. The few cells exhibiting high NIR fluorescence within 2 h in both normal and acidic media are probably dying or dead cells. From a structural consideration alone, internalization of the highly negatively charged LS662 into cells at neutral pH would not be expected because of electrostatic repulsion from the cell membrane's phosphate groups. Therefore, the delayed but significant accumulation of the molecular probe in cancer cells at long incubation times suggests a molecular rearrangement that facilitates passive or active transport in cells. Compared with cells treated at pH 7.4, fluorescence of LS662 was significantly higher under acidic conditions. This internalization process could be mediated by electrostatic interactions of protonated LS662 with the phosphate groups in cell membranes (**Figure 39D**). As a control, a less physiologically pH-sensitive dye cypate (**Figure 40B**)[31] was also incubated with 4T1/luc cells. As expected, the internalization of cypate was not pH-dependent (**Figure 41B**).

To investigate the mechanism of LS662 internalization, we incubated A431 or 4T1/luc cells with the pH sensor in acidic (pHe 6.4) and neutral (pHe 7.4) media in the presence or absence of sodium azide, an active transport inhibitor (**Figure 41A**).[32, 33] In both acidic and neutral solutions, cells treated with sodium azide exhibited lower NIR fluorescence than that of the untreated control. However, the decrease in LS662 fluorescence was higher under neutral (77% A431, 32% 4T1/luc) conditions at 8 h postincubation than it was under acidic conditions

(13% A431, 9.5% 4T1/luc) (**Figure 41B**). This finding suggests that the highly negatively

charged, nonprotonated LS662 overcomes electrostatic repulsion at the plasma membrane via an

active transport process. In the protonated form, ATP-independent endocytosis is the dominant

mechanism of LS662 internalization. Cypate internalization was not blocked by the addition of

sodium azide.

Because the NIR fluorescence of LS662 is weak under neutral pH, the high intracellular

fluorescence most likely occurred through the acidic endosomal pathway or by translocation into

acidic intracellular organelles. Coincubating LS662 with a lysosomal reporter, lysotracker green,

showed that the punctate LS662 fluorescence colocalized with the lysotracker dye, indicating

that LS662 is in the acidic lysosomes (**Figure 41D**).
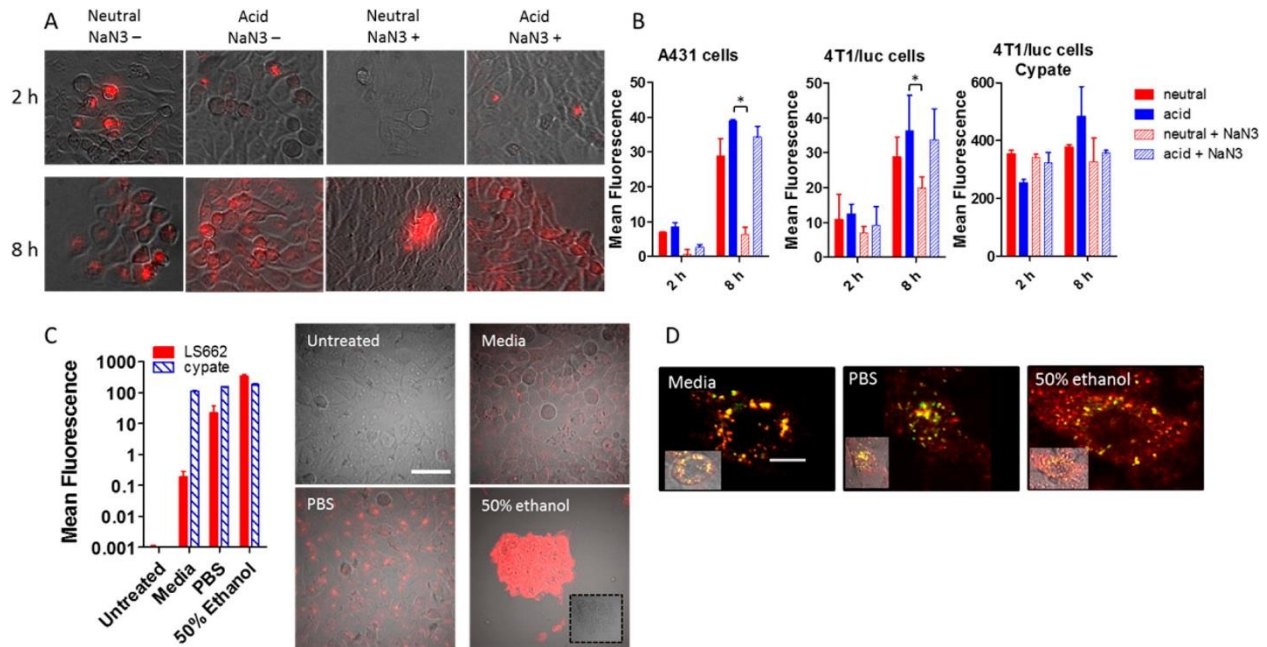
Figure 41. (A) Images of cellular uptake of LS662 in A431 cells for 2 or 8 h in normal

physiological (pH 7.4; neutral) or acidic (pH 6.4; acid) media. Sodium azide (NaN$_3$+) was added

to each condition to determine whether the internalization of LS662 is energy-dependent. (B)

Quantification of the cellular uptake, described in (A), in A431 and 4T1/luc cells with LS662 and cypate; *, p-value < 0.05. (C) Cellular uptake of LS662 and cypate in A431 cells treated under three conditions, media, PBS, and 50% ethanol, to probe healthy, dying, and dead cells, respectively. The images show LS662 fluorescence; cypate images are not shown. (D) Healthy, dying, and dead cells were coincubated with LS662 (red) and lysotracker (green) to investigate the subcellular localization of LS662. Scale bar = 10 μm.

6.4.3 LS662 is a highly sensitive reporter of dying and dead cells

Regardless of the treatment conditions, some cells exhibited bright LS662 fluorescence within 2 h post incubation, suggesting that the molecular probe could serve as reporter of cell death. To explore this capability, A431 cells were incubated with LS662 for 2 h under three different conditions, normal culture media, PBS solution, or 50% ethanol in PBS, to obtain predominantly healthy, dying, and dead cells, respectively (**Figure 41C**). Cypate was incubated with cells under similar conditions (**Figure 41C**). As cells die, a 5000-fold increase in LS662 fluorescence was observed, whereas the fluorescence from cypate only showed a moderate 2-fold increase. The small increase in cypate fluorescence could be attributed to nonspecific uptake in dead cells.

Previous studies have shown that cells undergoing necrosis or apoptosis are characterized by the disruption of their organelles' membranes, leading to the release of their contents and acidification of the cytosol, with fewer residual intact lysosomes.[14, 34, 35] Thus, the high increase in LS662 fluorescence in dead or dying cells suggests protonation of the molecule under the mild intracellular acidic conditions of these cells (**Figure 41C**). Loss of intracellular membrane integrity transforms the highly punctate LS662 fluorescence to a more diffuse intracellular

pattern. These results illustrate the multidimensional use of LS662 to localize tumors and possibly to identify dying cells in response to treatment.

6.4.4 Protonation of LS662 enhances NIR fluorescence in mouse and human cancer models

The primary goal of this study was to evaluate the feasibility of imaging diverse solid tumors using the simple pH-sensitive molecular probe in vivo. Starting with subcutaneous 4T1/luc tumors in the flanks of mice, fluorescence of LS662 in the tumor region was evident as early as 1 h postinjection, attaining maximum contrast at 72 h (**Figure 42Ai,ii**). The high tumor tissue-selective contrast was confirmed by ex vivo imaging and region of interest analysis of the tumor, with a tumor-to-muscle contrast of 15.7 ± 0.3 (**Figure 42Aiii**). The high fluorescence in the kidneys and liver suggests a bimodal excretion route for LS662. As a small hydrophilic molecule, renal excretion was expected. The significant hepatobiliary excretion indicates that a fraction of the dye was bound to blood proteins, which then presents the molecules to the liver for subsequent excretion. The widely used NIR fluorescent dyes, ICG and cypate, are excreted from the body by a similar hepatobiliary pathway (**Figure 42D**).[36, 37] Low uptake in the spleen and lungs suggests minimal aggregation of the molecular probe in vivo.
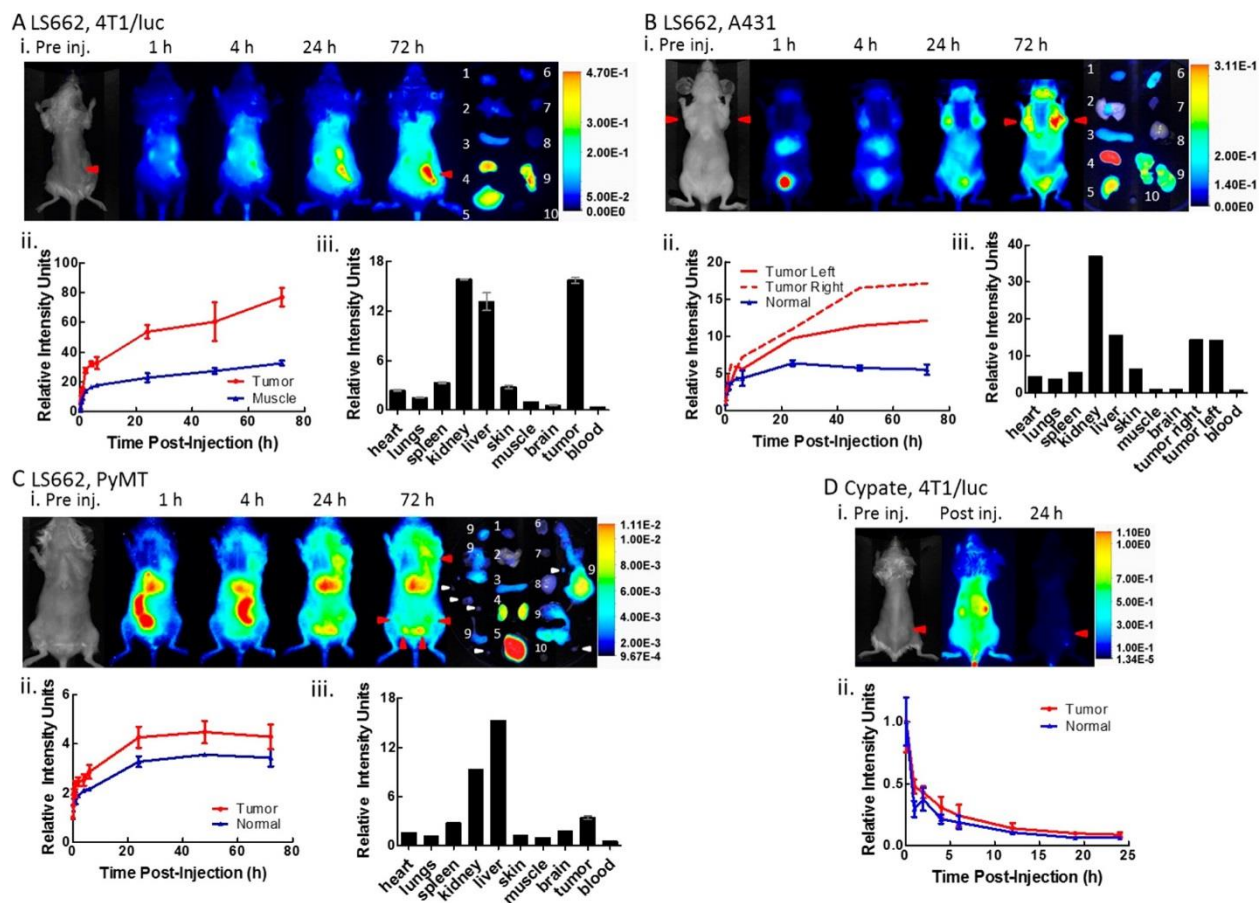
Figure 42. (A–C) LS662 in 4T1/luc murine breast cancer (A), A431 human epidermal cancer (B), and PyMT spontaneous breast cancer (C). (i) Fluorescence images of a tumor-bearing mouse at the indicated times postinjection. Red arrows indicate the location of the tumor. Preinjection image show a bright-field image of the mouse. (ii) Plot of the average fluorescence values of the tumor region compared to normal tissue control region obtained from the *in vivo* images. The values are normalized to the postinjection fluorescence intensity of each region. (iii) Fluorescence intensity in organs of interest after the mouse was sacrificed and the organs were excised. All values are normalized to the muscle signal. (D) Cypate in the 4T1/luc murine breast cancer model (*n* = 3). Error bars are shown for cases where *n* ≥ 3.

We compared the uptake of the pH-sensitive dye with that of cypate, a similar cyanine dye exhibiting less pH responsiveness.[31, 38] Longitudinal imaging of cypate in 4T1/luc tumor-bearing mice showed rapid clearance from the body within 1 h postinjection. The fluorescence of cypate was barely detectable after 24 h postinjection (**Figure 42D**). Quantitative image analysis shows that there is no selective accumulation or retention of cypate in tumors. A similar result using cypate was obtained with LS798 (**Figure 45**). This compound is structurally similar to LS662, but its fluorescence and absorption spectra do not respond to pH changes in the physiologically relevant range of pH 4–8 (**Figure 44**). These results lend credence to the use of simple and small pH-sensitive NIR fluorescent dyes to interrogate the acidic milieu of solid tumors.

Having demonstrated that LS662 can localize in the acidic environment of a subcutaneously implanted murine mammary tumor model, we extended this imaging approach to the human-origin A431 tumor xenograft model (**Figure 42B**). The tumor cells were grown bilaterally in the mammary fat pads of athymic nude mice. Administration of LS662 in tumor-bearing mice and subsequent fluorescence imaging showed a rapid clearance of the dye from blood and other tissues. At 1 h postinjection, high fluorescence in the bladder was observed, probably due to the low pH of urine. Although the initial fluorescence was low, the accumulation and activation of LS662 in the tumor were evident as early as 1 h postinjection, culminating in maximum tumor-to-normal tissue contrast at 72 h postinjection. This temporal increase suggests that nonfluorescent LS662 remained in circulation or was already trapped in the tumor and became fluorescent with continuous protonation of the molecules. A tumor-to-muscle contrast of 14.30 ± 0.03 was determined *ex vivo* from the excised organs (**Figure 42Biii**).

Subcutaneously implanted tumor models do not fully recapitulate the biologic and

histopathologic features of human cancers. Therefore, we explored the applicability of this

approach in the PyMT spontaneous murine breast cancer model. PyMT mice are

immunocompetent and present aspects of human breast cancer that are not represented by

xenograft models. The similarities include spontaneous tumor development and the complex

interaction of immune cells within the tumor. Intravenous administration of LS662 and

fluorescence imaging showed rapid hepatobiliary clearance within 1 h postinjection of LS662

(**Figure 42C**). This enhanced excretion pathway illustrates the variability in biodistribution that

can be induced in different animal models. In this model, liver uptake was favored compared to

the renal excretion observed in the subcutaneous tumor models (**Figure 42A,B**). Low

fluorescence was observed in the tumors around the mammary fat pads, becoming more evident

at 4 h before plateauing after 24 h postinjection (**Figure 42Cii**). This model also shows lower

tumor-to-muscle contrast (3.46 ± 0.19) than that of the 4T1/luc and A431 tumor models. It is

likely that the multifocal nature of the PyMT tumors prevented secreted protons from being

locally concentrated, as seen in the other tumors, which could minimize the extent of pHe

reduction from normal physiologic pHe. In spite of relatively low tumor-to-background contrast,

histologic analysis of excised tissue showed that LS662 was able to detect multiple small tumors.

6.4.5 Two-photon imaging and fluorescence histology reveal punctate and eiffuse intratumoral distributions of LS662

The planar NIR fluorescence imaging system that we used to acquire the *in vivo* images

is a surface-weighted low-resolution device. To determine the distribution of LS662 in the tumor

microenvironment, we used high-resolution two-photon fluorescence and second harmonic

generation microscopy for the study. 3D reconstruction of a freshly excised 4T1/luc tumor after

LS662 injection revealed a chaotic structure of collagen (blue) and elastin (green) that surround

and form the 4T1/luc tumor matrix (**Figure 43A**). LS662 (red) is distributed in the diffuse

extracellular region just interior to the tumor capsule and is localized with fibrous bundles

surrounding and inside the tumor. A depth of up to 100 μm was imaged, which is a typical

penetration depth for two-photon microscopy.[39] After two-photon imaging, the tumor was frozen

in OCT and sectioned for histology. Imaging of the same region shows LS662 fluorescence

originating from cellular regions of the tissue (**Figure 43A**, right). The two-photon images

demonstrated that LS662 is able to interrogate the extracellular matrix (ECM) of tumors, with a

significant fraction specifically internalizing into tumor cells.

Further analysis of the PyMT tumors via fluorescence histology shows that LS662

localized in specific cells and throughout the tumor stroma, supporting the findings from the

4T1/luc two-photon imaging (**Figure 43D**). We also found that a tumor-infiltrated lymph node

displayed high LS662 fluorescence (**Figure 43E**). Muscle samples from the left leg of the mouse

were obtained to evaluate the presence of LS662 in healthy tissue (**Figure 43F**). The absence of

NIR fluorescence indicates that LS662 is not present in normal tissue, except the excretory

organs. Acidification of the muscle tissue with PBS (pH 4.0) did not result in NIR fluorescence,

indicating the absence of residual nonprotonated LS662 in healthy tissue.
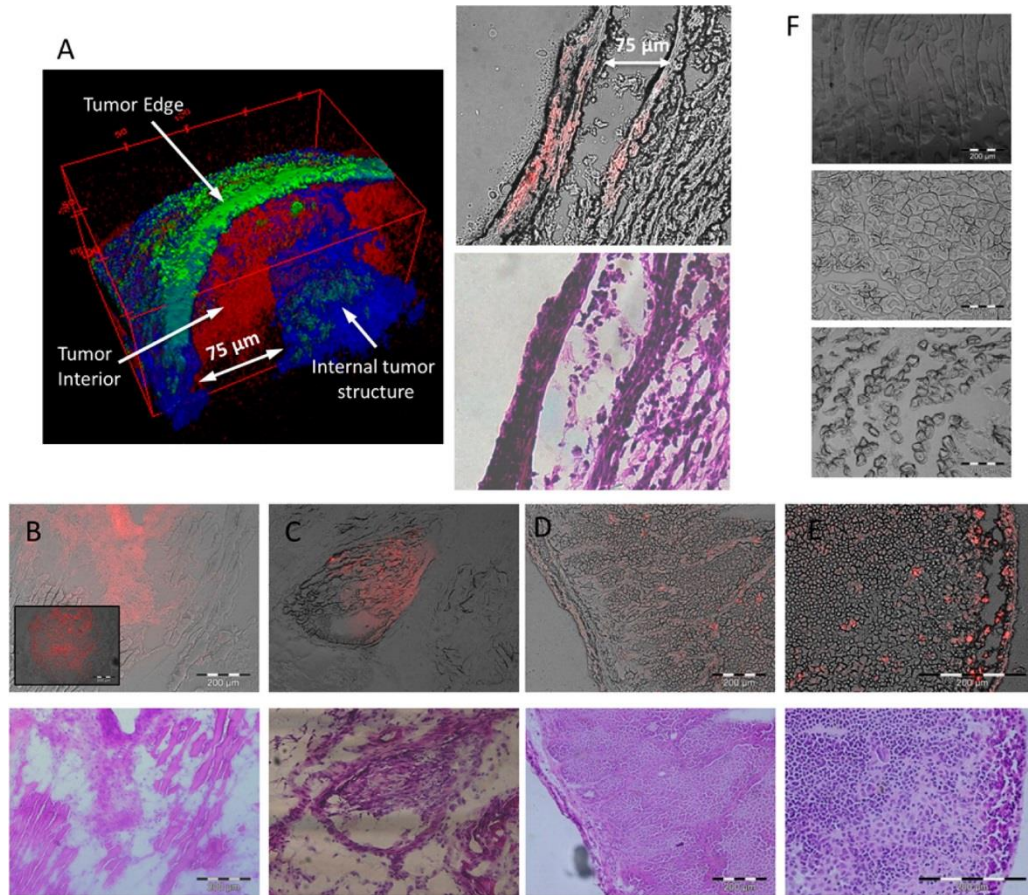
Figure 43. (A) Two-photon tomographic reconstruction of a 4T1/luc tumor, excised immediately after the animal was sacrificed, 24 h post initial injection of LS662 (green, elastin; blue, collagen; red, LS662). (B–D) LS662 fluorescence (red, top) and H&E stained (bottom) images of the same regions from serial sections of 4T1/luc (B), A431 (C), and PyMT (D) tumors. (E) Lymph node infiltrated with tumor cells showing LS662 fluorescence. (F) Muscle samples from 4T1/luc (top), A431 (middle), and PyMT (bottom) bearing mice show no LS662 fluorescence.

6.5 Discussion

Although it was previously considered to be a side product of enhanced glycolysis, acidification of the tumor environment appears to support tumor proliferation and metastasis of aggressive solid tumors. Earlier studies have demonstrated the potential of targeting this

physiologic condition for cancer detection and treatment.[3, 4, 9, 40] For optical imaging, pH-

responsive molecular designs include the conjugation of pH sensors to tumor-targeting groups

such as peptides or antibodies.[11] Other pH sensor design strategies include the incorporation of

pH-cleavable linkers into nanoparticle constructs, followed by the release of a high concentration

of chemotherapeutics or imaging agents in solid tumors *in vivo*.[41, 42] Similarly, conjugation of

multiple dyes to macromolecules via acid-cleavable linkers or loading of dyes into pH-

degradable nanoparticles can quench dye fluorescence, which is activated upon degradation of

the product under acidic conditions.[11, 16, 41] Previously, we demonstrated that conjugation of a pH

sensor to an RGD peptide allowed tumors to be detected with high tumor-to-background

fluorescence contrast. Fluorescence enhancement was generated only in intracellular

compartments, similar to that reported using other receptor-targeted approaches.[11] In this study,

we explored the feasibility of using a simple and small pH-sensitive molecule to image the acidic

pHe *in vivo*. By avoiding the complexity of nanoparticle formulations and conjugation of the pH-

sensitive molecules with tumor-targeting agents, LS662 represents a viable alternative to current

pH-sensing molecular probes. Because LS662 possesses intrinsic tumor-targeting and retention

properties, we can conjugate drugs instead of tumor-avid ligands to the free carboxylic acid

moiety for targeted therapy.

The pH in the extracellular environment of tumors is generally about 6.5, whereas the pH

of blood and most nontumor tissues is approximately 7.4. Because LS662 is a weak acid with a

pK_a of 5.2, the Henderson–Hasselbalch equation can be used to estimate the percentage of

protonated LS662 at pH 6.5 versus that at pH 7.4

$$pH = pK_a + log_{10}\frac{[A^-]}{[HA]}$$

where [A–] and [HA] are the nonprotonated and protonated forms of LS662, respectively. Using the above equation, we expect 0.6 and 5% of protonated LS662 to be in the nontumor and tumor environments, respectively, representing an 8-fold increase of the protonated form in the acidic tumor environment.

We studied the relative fluorescence enhancement of LS662 in tumor versus nontumor tissues, including the *in vivo* kinetic analysis and *ex vivo* fluorescence biodistribution for all cancer models used (**Figure 42**). Because pH-sensitive LS662 and less pH-sensitive cypate (in a physiologically relevant pH range) are not specifically targeted to tumor cells, we expect similar *in vivo* biodistribution profiles for both compounds. Therefore, the higher fluorescence intensity in the tumor tissues observed with LS662 is attributed to pH-dependent protonation of the dye. LS662 has a pK_a of 5.2 and exhibits low fluorescence above pH 7, which provides low background signal. Although these characteristics improved the tumor-to-surrounding tissue contrast, only a small fraction of LS662 is protonated between pH 6 and 7. Increasing the proportion of the protonated form of the dye in the acidic environment of tumors will improve both the tumor-to-nontumor contrast and net signal (fluorescence intensity). One approach to accomplish this goal is to develop or use a NIR fluorescent pH-sensitive dye possessing a pK_a of about 6.5 and negligible fluorescence above pH 7.2.

LS662 appears to accumulate and internalize in tumor cells by a bimodal pathway. In the nonprotonated form, the highly negatively charged molecules undergo ATP-dependent endocytosis. Although the exact mechanism of internalization is not known at this time, intracellular punctate fluorescence suggests an endosomal pathway that acidifies the molecules as they transit from early (higher pH) to late (lower pH) endosomes/lysosomes. In contrast, protonation of LS662 appears to facilitate internalization by a process that is less dependent on

active transport. We postulate that the positively charged LS662 interacts electrostatically with the phosphate groups on the cell membrane to induce internalization by energy-dependent and -independent mechanisms, similar to that of HIV tat-peptides or amphiphilic polymers.[43, 44]

Internalization of both protonated and nonprotonated forms of LS662 in cells by different mechanisms could lead to sporadic uptake of this molecular probe in many cells *in vivo*. However, our small animal imaging results indicate that it has high tumor selectivity, as demonstrated in three different cancer models. Accumulation in both the extracellular acidic space and in tumor cells provides a two-prong reporting strategy in which relatively weak fluorescence in tumors from molecules protonated in the extracellular space is visible within 1 h, followed by highly intense fluorescence induced by both intra- and extracellular protonation of LS662. Two-photon and SHG imaging also show that LS662 does not stain elastin and collagen fibers in the tumor matrix, a further indication of pH-associated selective uptake in tumor tissue.

Accurate sensing of pHe *in vivo* could be advantageous in monitoring tumor growth and cell death during therapy. Our results show that LS662 accumulates in a variety of cancer models, regardless of the tumor's origin. Comparison of LS662's uptake in these tumor models suggests that LS662 fluorescence may correlate with the differences in pHe and the distribution of the excreted protons (**Figure 42**). Diffuse and invasive tumors such as PyMT[45] release protons into a large tissue volume, which could result in a more neutral physiologic pHe than that of implanted tumors, such as 4T1/luc and A431, which could exhibit a lower pHe because protons are released in a small, encapsulated tissue volume. If it is validated with reference standards, the relative fluorescence of LS662 could be used to correlate tumor invasiveness and metastatic potential with the size, proton distribution, type, and origin.[46, 47] Unlike SNARF-1,[47, 48] which requires its use in high concentrations for pH sensing in the visible-light region, the NIR

emission of LS662 allows tumor tissues to be interrogated noninvasively in small animals with a higher detection sensitivity using a relatively lower dose of the molecular probe.

In summary, LS662 is a promising small molecule for reporting the cellular and extracellular pH of tumors. Its capacity to illuminate the tumors within 1 h, prolonged retention in tumors, and NIR fluorescence make it useful for diverse biomedical applications, including the targeted delivery of drugs. Low background NIR fluorescence before protonation improves tumor contrast *in vivo*. This molecular probe is also capable of sensing different stages of cell death, with over a 5000-fold fluorescence increase in dying and dead tumor cells because of the elevated acidity of necrotic or apoptotic tumor bodies.[34, 35] This work has unveiled a novel class of small molecules that can target diseased tissue simply through electrostatic changes produced by environmental factors.

6.6 Supporting information

6.6.1 Synthesis and characterization of LS798

The synthetic scheme is shown in **Figure 44** below. A mixture of sulpho-indole 3 (0.7 g 2.2 mmol) and methyl iodide (1 g, 6 mmol) was heated under reflux in ethanol overnight. The product 4 was precipitated with diethyl ether and used directly for dye synthesis after drying. A mixture of indole intermediate 4 (114 mg, 0.45 mmol) and Suzuki-product 2 (82 mg, 0.2 mmol) was heated under reflux in the presence of sodium acetate (55 mg, 0.67 mmol) in 10 mL mixed solution of 2 ethanol/acetic anhydride (50%/50%, v/v) for 20 h. After cooling, 3% of HCl in water was added to the resultant mixture. The crude material was purified by reverse-phase C-18 column chromatography, eluting with CH_3CN/H_2O gradient to afford 112 mg of desired dye 5 (yield 77%). NIR/vis: λ abs = 751 nm, λ em = 766 nm, ε = 195,000 $M^{-1}cm^{-1}$, φF (PBS) = 0.12, ESI-MS: m/z 728 (M+H, 100%). Unlike LS662, the absorption and emission spectra of LS798 in

different pH buffers from pH 2.1-10 remained nearly constant, indicating a lack of pH response (**Figure 44B**).
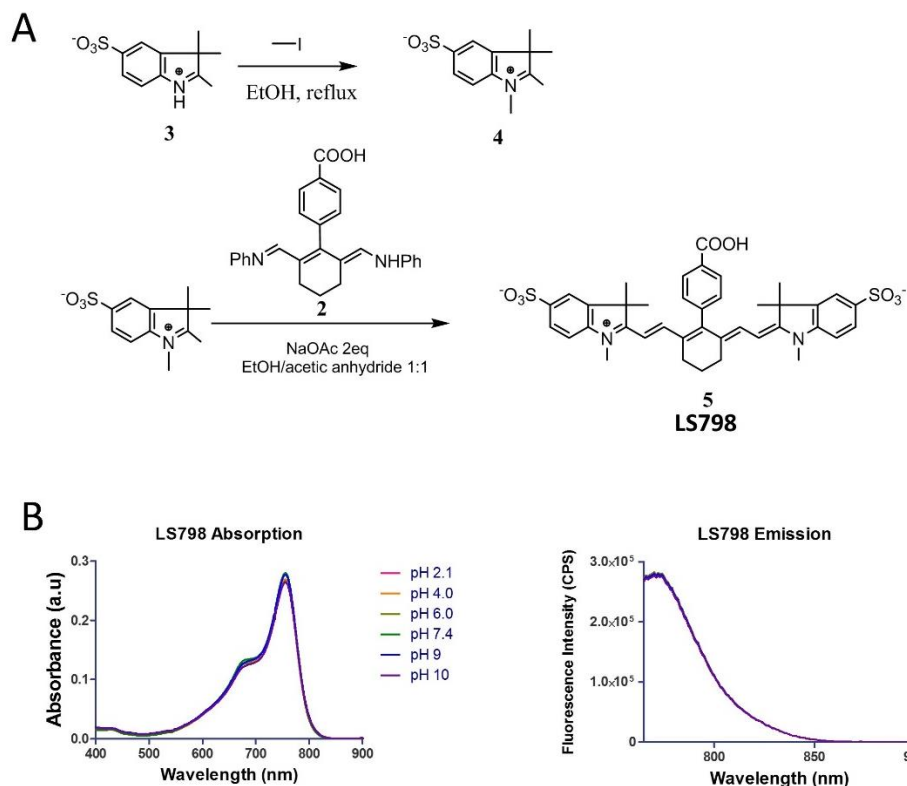
Figure 44. Synthetic scheme and spectral properties of LS798. A. Synthetic route of pH insensitive dye LS798.[5] B. Absorption and emission spectra of LS798 in different pH buffers from pH 2.1-10.

6.6.2 In vivo characterization of LS798

The in vivo biodistribution profiles of LS798 in mice bearing tumors are shown **Figure 45**. The relative intensity of LS798 normalized to post injection values has a maximum intensity at 24 h post injection. Fluorescence intensity of LS798 in tumors is an order of magnitude less than the intensity using LS662. After 24 h, fluorescence of LS798 in tumor decreased rapidly

compared to LS662 (**Figure 45**). In the A431 model, LS798 does not have any substantial uptake

in the tumors compared to LS662 (**Figure 45**). Similarly, the fluorescence of LS798 in the PyMT

tumor model was substantially lower than the same parameter using LS662. In all cases, the

tumor-to-nontumor contrast was much lower with LS798 relative to LS662.

Figure 45. In vivo distribution of LS798 in mouse models of cancer. LS798 in: A. 4T1/luc

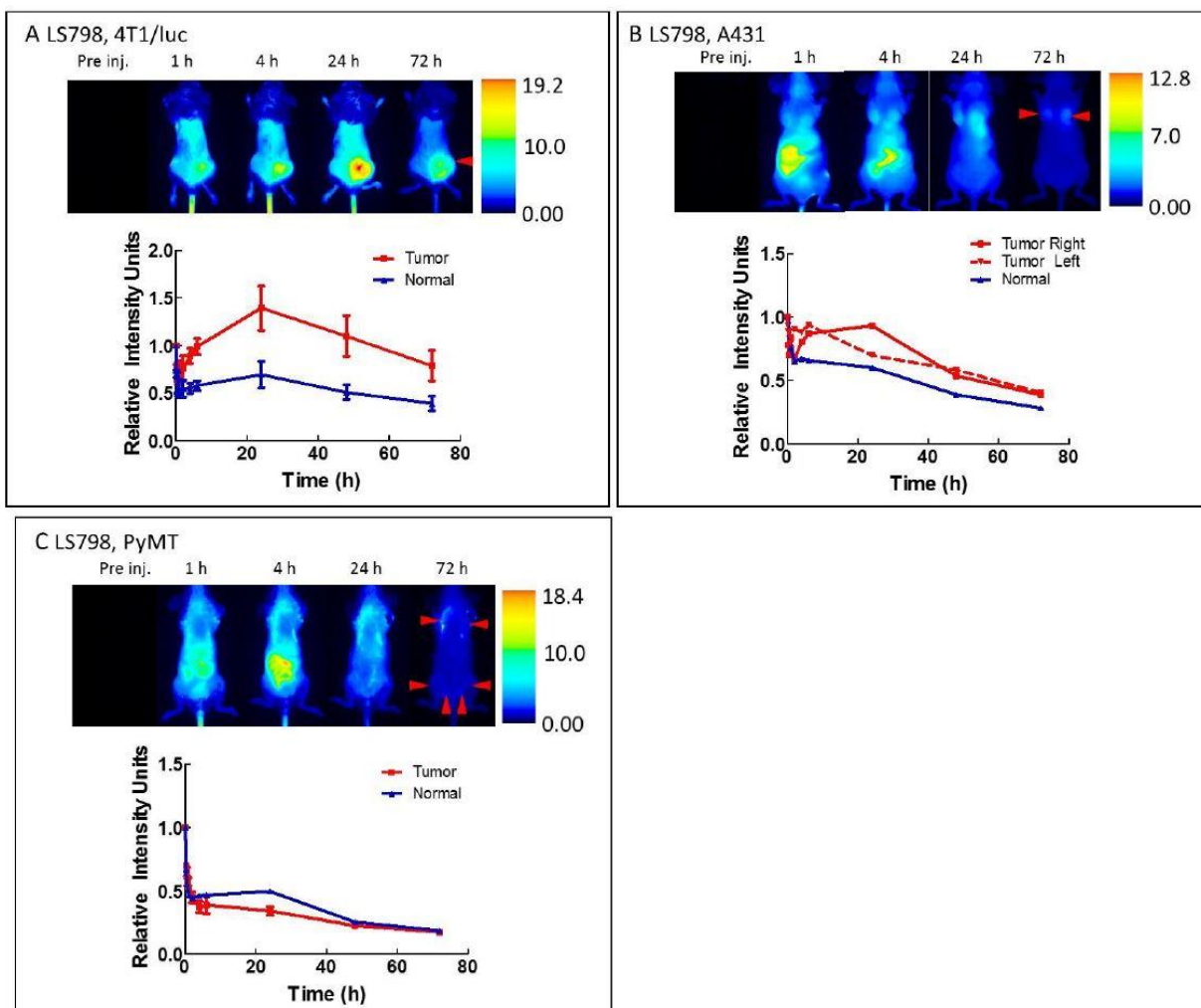murine breast cancer; B. A431, human epidermal cancer; and C. PyMT spontaneous breast

cancer. 4 Fluorescence images were obtained at the specified time points post-injection. Red

arrows indicate the location of the tumor. Plot of the average fluorescence values of the tumor

region compared to non-tumor tissue control regions are shown below each set of fluorescence images. The values are normalized to the post injection fluorescence intensity of each region. Error bars are obtained from n ≥ 3 experiments.

6.7 Acknowledgments

6.8 References

(1)   Cardone, R. A.; Casavola, V.; Reshkin, S. J. *Nat. Rev. Cancer* **2005**, *5*, 786.

(2)   Gillies, R. J.; Raghunand, N.; Karczmar, G. S.; Bhujwalla, Z. M. *J. Magn. Reson. Imaging* **2002**, *16*, 430.

(3)   Robey, I. F.; Baggett, B. K.; Kirkpatrick, N. D.; Roe, D. J.; Dosescu, J.; Sloane, B. F.; Hashim, A. I.; Morse, D. L.; Raghunand, N.; Gatenby, R. A.; Gillies, R. J. *Cancer Res.* **2009**, *69*, 2260.

(4)   Robey, I. F.; Nesbit, L. A. *Biomed Res Int* **2013**, *2013*, 485196.

(5)   Wu, F.; Guo, N. J.; Tian, H.; Marohn, M.; Gearhart, S.; Bayless, T. M.; Brant, S. R.; Kwon, J. H. *Inflamm Bowel Dis* **2011**, *17*, 241.

(6)   Raghunand, N.; He, X.; Sluis, R.; Mahoney, B.; Baggett, B.; Taylor, C.; Paine-Murrieta, G.; Roe, D.; Bhujwalla, Z.; Gillies, R. *Brit. J. Cancer* **1999**, *80*, 6.

(7)   Muller, V.; Riethdorf, S.; Rack, B.; Janni, W.; Fasching, P. A.; Solomayer, E.; Aktas, B.; Kasimir-Bauer, S.; Zeitz, J.; Pantel, K.; Fehm, T.; group, D. s. *Breast Cancer Res* **2011**, *13*, R71.

(8)   Neri, D.; Supuran, C. T. *Nat Rev Drug Discov* **2011**, *10*, 767.

(9)   Robey, I. F.; Martin, N. K. *BMC cancer* **2011**, *11*, 235.

(10)   Webb, B. A.; Chimenti, M.; Jacobson, M. P.; Barber, D. L. *Nat. Rev. Cancer* **2011**, *11*, 671.

(11)   Lee, H.; Akers, W.; Bhushan, K.; Bloch, S.; Sudlow, G.; Tang, R.; Achilefu, S. *Bioconjug. Chem.* **2011**, *22*, 777.

(12)   Urano, Y.; Asanuma, D.; Hama, Y.; Koyama, Y.; Barrett, T.; Kamiya, M.; Nagano, T.; Watanabe, T.; Hasegawa, A.; Choyke, P. L.; Kobayashi, H. *Nat. Med.* **2009**, *15*, 104.

(13)   Ogawa, M.; Kosaka, N.; Regino, C. A.; Mitsunaga, M.; Choyke, P. L.; Kobayashi, H. *Mol Biosyst* **2010**, *6*, 888.

(14)   Chan, K. W. Y.; Liu, G.; Song, X.; Kim, H.; Yu, T.; Arifin, D. R.; Gilad, A. A.; Hanes, J.; Walczak, P.; van Zijl, P. C. M.; Bulte, J. W. M.; McMahon, M. T. *Nat. Materials* **2013**, *12*, 7.

(15)   Kogan, F.; Haris, M.; Singh, A.; Cai, K.; Debrosse, C.; Nanga, R. P.; Hariharan, H.; Reddy, R. *Magn. Reson. Med.* **2014**, *71*, 164.

(16)   Rivlin, M.; Horev, J.; Tsarfaty, I.; Navon, G. *Sci. Rep.* **2013**, *3*, 3045.

(17)   Liu, Y.; Bauer, A. Q.; Akers, W. J.; Sudlow, G.; Liang, K.; Shen, D.; Berezin, M. Y.; Culver, J. P.; Achilefu, S. *Surgery* **2011**, *149*, 689.

(18)   Kaijzel, E. L.; van Heijningen, P. M.; Wielopolski, P. A.; Vermeij, M.; Koning, G. A.; van Cappellen, W. A.; Que, I.; Chan, A.; Dijkstra, J.; Ramnath, N. W.; Hawinkels, L. J.; Bernsen, M. R.; Lowik, C. W.; Essers, J. *Circ. Cardiovasc. Imag.* **2010**, *3*, 567.

(19)   Sheth, R. A.; Upadhyay, R.; Stangenberg, L.; Sheth, R.; Weissleder, R.; Mahmood, U. *Gynecol. Oncol.* **2009**, *112*, 616.

(20)   Jaffer, F. A.; Kim, D. E.; Quinti, L.; Tung, C. H.; Aikawa, E.; Pande, A. N.; Kohler, R. H.; Shi, G. P.; Libby, P.; Weissleder, R. *Circulation* **2007**, *115*, 2292.

(21)   Jaffer, F. A.; Vinegoni, C.; John, M. C.; Aikawa, E.; Gold, H. K.; Finn, A. V.; Ntziachristos, V.; Libby, P.; Weissleder, R. *Circulation* **2008**, *118*, 1802.

(22)   Barnett, E. M.; Zhang, X.; Maxwell, D.; Chang, Q.; Piwnica-Worms, D. *Proc. Natl. Acad. Sci. U.S.A.* **2009**, *106*, 9391.

(23)   Klohs, J.; Baeva, N.; Steinbrink, J.; Bourayou, R.; Boettcher, C.; Royl, G.; Megow, D.; Dirnagl, U.; Priller, J.; Wunder, A. *J. Cereb. Blood Flow Metab.* **2009**, *29*, 1284.

(24)   Maxwell, D.; Chang, Q.; Zhang, X.; Barnett, E. M.; Piwnica-Worms, D. *Bioconjug. Chem.* **2009**, *20*, 702.

(25)   Hilderbrand, S. A.; Kelly, K. A.; Niedre, M.; Weissleder, R. *Bioconjug. Chem.* **2008**, *19*, 1635.

(26)   Panizzi, P.; Nahrendorf, M.; Wildgruber, M.; Waterman, P.; Figueiredo, J. L.; Aikawa, E.; McCarthy, J.; Weissleder, R.; Hilderbrand, S. A. *Journal of the American Chemical Society* **2009**, *131*, 15739.

(27)   Smith, M. C. P.; Luker, K. E.; Garbow, J. R.; Prior, J. L.; Jackson, E.; Piwnica-Worms, D.; Luker, G. D. *Cancer Res.* **2004**, *64*, 8604.

(28)   Chen, X.; Nadiarynkh, O.; Plotnikov, S.; Campagnola, P. J. *Nat. Protoc.* **2012**, *7*, 654.

126

(29)   Mansfield, J.; Yu, J.; Attenburrow, D.; Moger, J.; Tirlapur, U.; Urban, J.; Cui, Z.; Winlove, P. *J. Anat.* **2009**, *215*, 682.

(30)   Angiari, S.; Rossi, B.; Piccio, L.; Zinselmeyer, B. H.; Budui, S.; Zenaro, E.; Della Bianca, V.; Bach, S. D.; Scarpini, E.; Bolomini-Vittori, M.; Piacentino, G.; Dusi, S.; Laudanna, C.; Cross, A. H.; Miller, M. J.; Constantin, G. *J. Immunol.* **2013**, *191*, 5489.

(31)   Zhang, Z.; Achilefu, S. *Chem. Commun. (Camb)* **2005**, 5887.

(32)   Keilin D., H. E. F. *Proc. R. Soc. London, Ser. B* **1939**, *127*, 167.

(33)   Cao, W.; Zheng, W.; Chen, T. *Sci. Rep.* **2015**, *5*, 9157.

(34)   Shrode, L. M.; Tapper, H.; Grinstein, S. *J. Bioenerg. Biomembr.* **1997**, *29*, 7.

(35)   Casey, J. R.; Grinstein, S.; Orlowski, J. *Nat. Rev. Mol. Cell. Biol.* **2010**, *11*, 50.

(36)   Patwardhan, S.; Bloch, S.; Achilefu, S.; Culver, J. *Opt. Express* **2005**, *13*, 14.

(37)   Guo, J.; Du, C.; Shan, L.; Zhu, H.; Xue, B.; Qian, Z.; Achilefu, S.; Gu, Y. *Contrast Media Mol. Imaging* **2012**, *7*, 289.

(38)   Achilefu, S.; Dorshow, R.; Bugai, J.; R., R. *Invest. Radiol.* **2000**, *35*, 6.

(39)   Helmchen, F.; Denk, W. *Nat. Methods* **2005**, *2*, 932.

(40)   Zoonens, M.; Reshetnyak, Y. K.; Engelman, D. M. *Biophys. J.* **2008**, *95*, 225.

(41)   Wang, Y.; Zhou, K.; Huang, G.; Hensley, C.; Uange, X.; Ma, X.; Zhao, T.; Sumer, B. D.; DeBerardinis, R. J.; Gao, J. *Nat. Mater.* **2013**.

(42)   Yang, J. *Adv. Drug Deliv. Rev.* **2012**, *64*, 965.

(43)   Madani, F.; Lindberg, S.; Langel, U.; Futaki, S.; Graslund, A. *J. Biophys.* **2011**, *2011*, 414729.

(44)   Palermo, E. F.; Kuroda, K. *Appl. Microbiol. Biotechnol.* **2010**, *87*, 1605.

(45)   Lin, E. Y.; Jones, J. G.; Li, P.; Zhu, L.; Whitney, K. D.; Muller, W. J.; Pollard, J. W. *Amer. J. Path.* **2003**, *163*, 2113.

(46)   Gatenby, R. A.; Gawlinski, E. T.; Gmitro, A. F.; Kaylor, B.; Gillies, R. J. *Cancer Res.* **2006**, *66*, 5216.

(47)   Estrella, V.; Chen, T.; Lloyd, M.; Wojtkowiak, J.; Cornnell, H. H.; Ibrahim-Hashim, A.; Bailey, K.; Balagurunathan, Y.; Rothberg, J. M.; Sloane, B. F.; Johnson, J.; Gatenby, R. A.; Gillies, R. J. *Cancer Res.* **2013**, *73*, 1524.

(48)   Tseng, J. C.; Benink, H. A.; McDougall, M. G.; Chico-Calero, I.; Kung, A. L. *Curr. Chem. Genomics* **2012**, *6*, 48.

Chapter 7 : Conclusions

In this dissertation, we applied optical imaging and therapy techniques to develop a new strategy for PDT. We have addressed several challenges of current cancer therapies: lack of adequate tumor targeting (Chapter 5 : and Chapter 6 :), failure to treat hypoxic tumor cells (Chapter 2 :), and induction of chemotherapy and radiation therapy resistant phenotypes (Chapter 3 : , Chapter 4 : , and Chapter 5 :).

To address lack of adequate tumor targeting we developed a NIR theranostic PS (Chapter 5 :) and a pH sensitive NIR fluorophore (Chapter 6 :) that both obtained high uptake in the tumor compared to normal tissue. In Chapter 5 : , we showed that LS797 accumulates in squamous cell carcinomas and that by monitoring the NIR fluorescence of cypate, we could localize the tumor before treatment, enabling us to choose the optimal DLI. The subsequent light activation of Ce6 produced ROS and resulted in significant tumor regression and slowing of tumor growth. In Chapter 6 : , the development of a pH sensitive NIR fluorophore LS662, provided insight into the acidity of the tumor microenvironment. Interestingly, the protonation of one indolenium ring nitrogen by the acidic tumor microenvironment resulted in retention of LS662 in tumor cells and the extracellular spaces, even without a direct method of targeting. This has implications for delivery drugs to all parts of the tumor, not just the tumor cells. In particular, for PDT, this could enable activation of all three mechanisms of therapeutic action: direct cell death, shut-down of microvessels, and activation of the immune system.

To address the limitation of chemotherapy, radiation therapy and PDT to treat hypoxic tumors, we constructed and characterized a dual type I/II nano-photosensitizer, TiO_2-N3 (Chapter 2 :). In normoxic conditions, TiO_2-N3, produced 3- or 4-fold greater hydroxyl radicals

and hydrogen peroxide than bare TiO_2, respectively. In addition, under hypoxic conditions TiO_2-N3 maintained high hydroxyl production, unlike TiO_2 and N3. TiO_2-N3 is a dual type I/II PS under normoxic conditions and a type I PS under hypoxic conditions, making it an ideal candidate for treating heterogeneously hypoxic tumors.

In order to determine the ideal intracellular localization for TiO_2-N3, we first developed a method for monitoring PDT induced cell damage (Chapter 3 :) and second determined in which organelle ROS production resulted in the greatest cell death (Chapter 4 :).

To monitor and characterize ROS induced cell damage, we developed a fluorescence lifetime method. Since many PSs are internalized into cells through the endosomal pathway, it is important to understand how ROS generated in endosomes and lysosomes induce damage. As a model for lysosomal damage, we used bafilomycin A1, a V-ATPase inhibitor which neutralizes the pH of lysosomes. PS1 FLIM was able to detect and quantify the increase in lysosome pH after addition of bafilomycin. This informed the use of PS1 FLIM to monitor damage due to PDT. Immediately after light activation of PS1, the pH of lysosomes increased, indicating that the PDT generated ROS induced lysosome damage. We also found that lysosomal PDT resulted in greater cell killing than endosomal PDT, even after normalization of intracellular PS concentration. Therefore, the subcellular localization of the PS is extremely important to therapeutic efficacy.

After determining the importance of the PS's localization along the endosomal pathway, we wanted to determine if other organelles had different susceptibilities to ROS damage. In Chapter 4 : , we compared four Ce6 based PSs with different organelle localizations: lysosome (PS1 or PS2), ER (Ce6), and dual mitochondria and lysosome (PS3). By using Ce6 for all

targeted PS, we were able to eliminate differences in the photophysical properties that often complicate such studies. Overall, ER PDT resulted in the greatest cell killing, followed by lysosome PDT with PS2, dual mitochondria and lysosome PDT with PS3, and finally lysosome PDT with PS1. The ER is implicated in activation of the immune system. In fact, previous studies have shown that ROS produced in the ER can induce the UPR, aiding in release of tumor antigens and immune system activation. In this study we have established that ROS production in the ER results in the greatest cell death. Next we would like to determine in which organelle oxidative damages induces the greatest activation of the immune system. Optimizing cell death in conjunction with immune activation would increase overall tumor regression and reduce the induction of tumor resistance.

In conclusion, we have designed and developed the requisite elements for a new PDT strategy. To ensure all three mechanisms of PDT tumor regression are activated, the PS must be targeted to both tumor cells (for direct cell death) and the tumor microenvironment (to disrupt tumor vasculature and activate the immune system). We have shown the LS662 accumulates in both of these regions. Within the cell, we have shown that activation of the PS in the ER results in the greatest cell death. It is also likely that ER localization will aid in the activation of the immune system. Finally, we showed that TiO_2-N3 synergistically produced potent hydroxyl radicals, even under hypoxic conditions. Therefore, combination of LS662, TiO_2-N3 and an ER targeting ligand will enable activation of all three PDT pathways to enhance tumor regression and limit development of therapy resistance.